The Relation Between Structure and Function in Brain Networks

A network science perspective

Meier, Jil

DOI
10.4233/uuid:31b25b38-45e9-4469-810b-79fe19905a4d

Publication date
2017

Document Version
Final published version

Citation (APA)
Meier, J. (2017). *The Relation Between Structure and Function in Brain Networks: A network science perspective*. [Dissertation (TU Delft), Delft University of Technology]. https://doi.org/10.4233/uuid:31b25b38-45e9-4469-810b-79fe19905a4d

THE RELATION BETWEEN STRUCTURE AND FUNCTION IN BRAIN NETWORKS

- A NETWORK SCIENCE PERSPECTIVE -

Jil Meier

THE RELATION BETWEEN STRUCTURE AND FUNCTION IN BRAIN NETWORKS

- A NETWORK SCIENCE PERSPECTIVE -

THE RELATION BETWEEN STRUCTURE AND FUNCTION IN BRAIN NETWORKS

- A NETWORK SCIENCE PERSPECTIVE -

Proefschrift

ter verkrijging van de graad van doctor
aan de Technische Universiteit Delft,
op gezag van de Rector Magnificus prof. ir. K.C.A.M. Luyben,
voorzitter van het College voor Promoties,
in het openbaar te verdedigen op woensdag 24 mei 2017 om 10:00 uur

door

Jil Mona MEIER

Master of Science in Mathematical Finance and Actuarial Science,
Technische Universität München, Duitsland,
geboren te Bremen, Duitsland.

Dit proefschrift is goedgekeurd door de

promotors: prof. dr. ir. P. Van Mieghem en prof. dr. C. J. Stam

Samenstelling promotiecommissie:

Rector Magnificus,	voorzitter
prof. dr. ir. P. Van Mieghem,	Technische Universiteit Delft
prof. dr. C. J. Stam,	Vrije Universiteit Medisch Centrum Amsterdam
Onafhankelijke leden:	
Prof. dr. ir. M. J. T. Reinders,	Technische Universiteit Delft
Prof. Dr. E. Eisemann,	Technische Universiteit Delft
Prof. Dr. M. Á. Serrano,	Universitat de Barcelona, Spanje
Dr. L. Douw,	Vrije Universiteit Medisch Centrum Amsterdam
Dr. M. P. van den Heuvel,	Universitair Medisch Centrum Utrecht

Keywords: structural brain networks, functional brain networks, effective connectivity, information flow, network motifs, shortest paths, epidemic spreading model

Printed by: Ipskamp Printing

Cover Design: Jasper Hamann, original artwork by Patrickss

ISBN 978-94-028-0638-0

An electronic version of this dissertation is available at
http://repository.tudelft.nl/.

To all the people who ever taught me something,
from my first words to conducting good research.

CONTENTS

Summary **ix**

Samenvatting **xi**

1 Introduction **1**

2 The Union of Shortest Path Trees of Functional Brain Networks **5**
- 2.1 Introduction 5
- 2.2 Materials and Methods 6
  - 2.2.1 Data Acquisition 6
  - 2.2.2 Link weights in functional brain networks as communication probabilities 7
- 2.3 Results 8
- 2.4 Discussion 9
- 2.5 Conclusion 10
- 2.6 Appendix: Link weight distribution of functional brain networks 11

3 Generalized α-Tree Sampling Method Shows Link Importance Beyond Betweenness **13**
- 3.1 Introduction 13
- 3.2 Construction of α-Trees 13
- 3.3 Properties of α-trees 16
  - 3.3.1 Link Density of α-Trees 16
  - 3.3.2 Distribution of α_c and other jump points 16
  - 3.3.3 A New Link Ordering Based on the α-Trees 18
- 3.4 Application to Functional Brain Networks 22
- 3.5 Conclusion 25
- 3.6 Appendix 26
  - 3.6.1 Spacings 26
  - 3.6.2 Additional Properties of the USPT 26

4 Motifs in Functional Brain Networks **31**
- 4.1 Introduction 31
- 4.2 Motif-Based Analysis of Effective Connectivity in Brain Networks 32
  - 4.2.1 Methods 32
  - 4.2.2 Results 34
  - 4.2.3 Discussion and Conclusion 36
  - 4.2.4 Appendix. 37
- 4.3 Brain Network Clustering with Information Flow Motifs (Extended) 38
  - 4.3.1 From measurements to directed networks 38
  - 4.3.2 Information flow motifs 39
  - 4.3.3 Motif-based clustering 41
  - 4.3.4 Discussion 42
  - 4.3.5 Conclusion. 44

5 A mapping between the structural and functional brain networks **45**
- 5.1 Introduction 45
- 5.2 Materials and Methods 47
  - 5.2.1 Participants and Data Acquisition 47
  - 5.2.2 Mathematical Background 48
  - 5.2.3 Mathematical Methodology 48

5.3 Results . . . 49
5.4 Discussion . . . 50
  5.4.1 Neurobiological interpretation . . . 55
  5.4.2 Technical implications . . . 57
  5.4.3 Methodological considerations . . . 57
5.5 Conclusion . . . 57
5.6 Supplementary Information . . . 59
  5.6.1 Theory . . . 59
  5.6.2 Data Analysis . . . 60
  5.6.3 Comparison of fitted coefficient values for different modalities . . . 66
  5.6.4 Interpretation with walks . . . 66
  5.6.5 Comparison with a previous study . . . 66
  5.6.6 Error analysis . . . 68
  5.6.7 Reshuffled matrices . . . 70
  5.6.8 Details of the fitting procedure . . . 71
  5.6.9 Dimension differences . . . 81

6 The Epidemic Spreading Model and the Direction of Information Flow in Brain Networks 83
6.1 Introduction . . . 83
6.2 Methods . . . 85
6.3 Results . . . 87
6.4 Discussion . . . 88
6.5 Conclusion . . . 91
6.6 Appendix . . . 92
  6.6.1 Additional Figures . . . 92
  6.6.2 Randomly Reshuffled Matrices . . . 92
  6.6.3 Directed Structural Network of the Macaque Brain . . . 92
  6.6.4 Correlation versus Transfer Entropy . . . 98
  6.6.5 The Covariance $\widetilde{\rho}\left(X_i\left(t\right), X_j\left(t+h\right)\right)$ for a Small Time Lag h. . . . 99

7 Conclusion 101

Acknowledgements 103

References 105

Curriculum Vitæ 113

List of Publications 115

SUMMARY

Over the last two decades the field of network science has been evolving fast. Many useful applications in a wide variety of disciplines have been found. The application of network science to the brain initiated the interdisciplinary field of complex brain networks. On a macroscopic level, brain regions are taken as nodes in a network. The analysis of pairwise connections between the brain regions as links has provided a new perspective on many problems. The application of network science to neuroscience data helped, for example, to identify the disruptions due to different neurological disorders when comparing healthy and abnormal brain networks.

In this dissertation, we focus on the macroscopic level of brain regions and analyze their pairwise connections from a network science perspective. We address different general research questions from network science and exploit their application possibilities towards brain networks. Due to different measurement techniques, one can construct many different representations of brain networks. We thereby distinguish between the structural and functional brain network. Structural brain networks map the anatomical connections between the regions, which we could interpret as the 'streets' of the brain. On top of these streets, we can measure the traffic with techniques like e.g. magnetoencephalography (MEG) or functional Magnetic Resonance Imaging (fMRI) resulting in so-called functional brain networks. However, the relation between the structural and the functional brain networks is still insufficiently understood.

The first main research question of this dissertation focuses on the functional network layer and tries to identify the most important links and motifs of these networks. For this purpose, we propose the union of shortest path trees (USPT) as a new sampling method extracting all the shortest paths of a network (Chapter 2 and 3). After constructing the USPT, we compare the individual functional brain networks of multiple sclerosis patients and healthy controls (Chapter 2). Furthermore, we generalize this sampling method and present a new ranking of all the links based on the USPT (Chapter 3). Regarding the higher-order building blocks of the functional brain networks, we analyze the so-called information flow motifs based on MEG data from different frequency bands (Chapter 4).

After researching the local properties of the functional brain networks, we analyze the influence of the underlying structural connections on the emerging information flow. Thus, the second main research question concerns the relationship between the functional and the underlying structural connectivity. Specifically, we analyze which topological properties of the structural networks drive the functional interactions. First, this question is approached in a mathematical and straightforward manner by assuming that an analytic function between the two networks exists (Chapter 5). We investigate this mapping function and its reverse by evaluating empirical individual and group-averaged multimodal data sets. A second approach towards the structure-function relationship employs a simple model of activity spread. The epidemic spreading model is applied on the human connectome to investigate the global patterns of directional information flow in brain networks (Chapter 6). The main focus here lies on the pairwise measure of transfer entropy to investigate the influence of one brain region on another. We present the results for the local and global outcomes of the dynamic spreading process aiming to identify the driving structural properties behind the observed global patterns.

SAMENVATTING

Tijdens de afgelopen twee decennia is het domein van de netwerkwetenschap snel geëvolueerd. Veel nuttige toepassingen zijn gevonden in een groot scala van disciplines. De toepassing van netwerkwetenschap op het brein initieerde de interdisciplinaire tak van de complexe breinnetwerken. Op een macroscopisch niveau worden hersengebieden gezien als knopen in een netwerk. De analyse van paarsgewijze connecties tussen hersengebieden als verbindingen heeft een nieuw perspectief op tal van vraagstukken opgeleverd.

In deze dissertatie concentreren we ons op het macroscopische niveau van breingebieden en analyseren de connecties tussen paren vanuit het perspectief van de netwerkwetenschap. We behandelen verschillende algemene onderzoeksvragen uit de netwerkwetenschap en bestuderen de toepassingsmogelijkheden van netwerkwetenschap op breinnetwerken. Met verschillende meettechnieken kan men vele verschillende afbeeldingen van breinnetwerken bouwen. Wij maken hierbij onderscheid tussen het structurele en functionele netwerk. Structurele breinnetwerken brengen de anatomische verbindingen tussen de gebieden in kaart, die we kunnen interpreteren als 'straten' van de hersenen. Boven op deze straten kunnen we het verkeer meten met technieken, zoals magnetoencephalography (MEG) of functionele kernspintomografie (fMRI), die resulteren in zogenaamde functionele breinnetwerken. De relatie tussen de structurele en functionele breinnetwerken is echter nog onvoldoende begrepen.

De eerste hoofdonderzoeksvraag van deze dissertatie richt zich op de functionele netwerklaag en probeert de meest belangrijke verbindingen en motieven van deze netwerken te identificeren. Daarvoor stellen we de union of shortest path trees (USPT) methode voor, waarmee we alle kortste paden van een netwerk extraheren (Hoofdstuk 2 en 3). Na het construeren van de USPT vergelijken we de individuele functionele breinnetwerken van multiple sclerose patiënten met een gezonde controlegroep (Hoofdstuk 2). Tevens hebben we deze manier van de bepaling van kortste paden gegeneraliseerd en presenteren een nieuwe rangschikking van alle verbindingen gebaseerd op de USPT (Hoofdstuk 3). Met het oog op de hogere orde bouwstenen van het functionele breinnetwerk analyseren we de zogenaamde informatiestroom motieven met behulp van MEG gegevens van verschillende frequentiebanden (Hoofdstuk 4).

Na het onderzoeken van deze lokale eigenschappen van de functionele breinnetwerken analyseren we de invloed van de onderliggende structurele verbindingen op de zichtbaar wordende informatiestroom. De tweede hoofdonderzoeksvraag richt zich op de relatie tussen de functionele en de onderliggende structurele verbindingen. Meer nauwkeurig analyseren we welke topologische eigenschappen van de structurele netwerken de functionele interacties beïnvloeden. Eerst is deze vraag benaderd op een wiskundige en directe manier door aan te nemen dat er een analytische relatie tussen de twee netwerken bestaat (Hoofdstuk 5). We onderzoeken deze relatie en zijn inversie door het evalueren van empirische multimodale datasets van individuen en groepsgemiddelden. Een tweede benadering van de structuur-functie relatie benut een eenvoudig model van de verspreiding van activiteit. Het epidemische verspreidingsmodel is toegepast op het menselijk connectoom om het globale patroon van gerichte informatiestromen in breinnetwerken te onderzoeken (Hoofdstuk 6). De nadruk ligt hier op de meting van paarsgewijze overdrachtsentropie om de invloed te onderzoeken die gebieden in het brein op elkaar hebben. We presenteren de resultaten van de lokale en globale uitkomsten van het dynamische verspreidingsproces met als doel de onderliggende sturende structurele eigenschappen van de geobserveerde globale patronen te identificeren.

1

INTRODUCTION

The human brain is one of the most complex systems of human knowledge. Understanding brain dynamics in healthy subjects and their disruptions in patients has become a central interdisciplinary research question [14, 93]. With big projects, like e.g. the Human Brain Project[1], different governments are trying to advance this research field in a fast-forward manner. Measurement techniques in neuroscience have simultaneously been largely improved over the past decades. Together, more and more data is becoming, often freely[2], available attracting researchers from many different fields with various backgrounds. However, we are far from understanding all those measurements of the complex processes continuously ongoing and dynamically changing in the human brain. Consequently, an even worse reality is that we do not sufficiently understand many of the currently known neurological disorders.

The field of network science has the advantage to be applicable in many different research areas. Generally speaking, network science is a bit like mathematics: it can be regarded as a common language that initiates and facilitates communication between scientists of the most distant research fields. When building a network out of a complex system, one has to focus on common properties of the single entities and on their connections. A network is formally defined by nodes, which can represent any kind of individual objects, and links symbolizing their connections among each other in a pairwise manner. The most intuitive example is often a social network, where humans are the nodes and there exists a link between them if they are friends. But besides social science, the concepts of network science have already been applied e.g. in computer science, economics, electrical engineering and biology [71]. After building the network, the comparison with other networks from completely different fields can begin and the grounds are set for a barrier-free exchange with scientists from many different disciplines. In this manner, neuroscientists have followed the movement and collaborate in many different research groups around the world in the fast-evolving field of 'complex brain networks' [14, 86, 93].

Analyzing the brain as a network has already led to many new insights in neuroscience with regard to healthy and abnormal brain function [10]. In this dissertation, we focus on a macroscopic whole-brain analysis where nodes represent brain regions and links the connections between them. The connections between brain regions can be measured by different non-invasive techniques. Diffusion Tensor Imaging (DTI) can provide us with information about the anatomical connections in the brain by measuring white-matter tracts. The brain regions together with the anatomical links between them build the so-called structural brain network. In contrast to these structural connections, other techniques like e.g. magnetoencephalography (MEG) and functional Magnetic Resonance Imaging (fMRI) capture time series of activation for each brain region. Based on these time series, one can calculate their pairwise interactions and build the functional brain network. The simplest statistical dependency between two time series is probably their correlation, which is referred to as the functional connectivity between regions. For the functional brain network, the arising network is not binary but the differences in interaction patterns are often characterized by a link weight normalized to the $(0,1)$ interval. The constructed structural and functional brain networks can be placed into a two-layer framework (see Figure 1.1).

---

[1] https://www.humanbrainproject.eu/

[2] see e.g. http://www.humanconnectome.org/

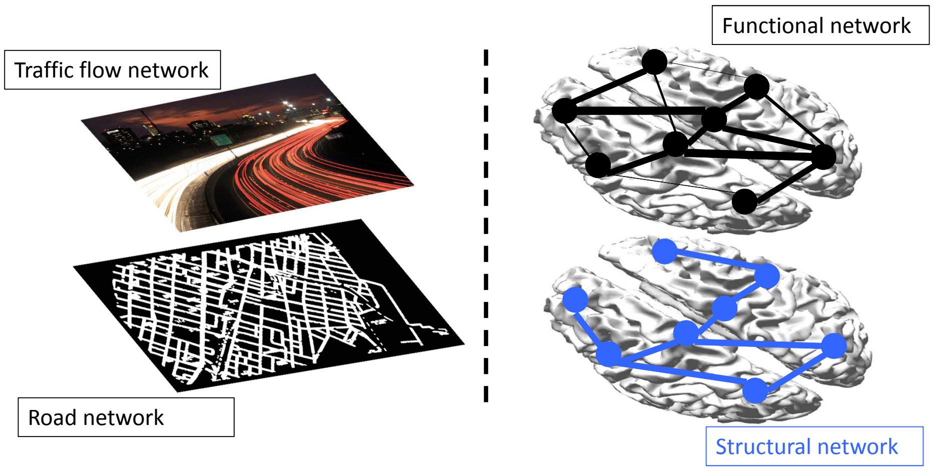

Figure 1.1: The brain can be analyzed as a multilayer network consisting of the anatomical connections in form of the structural brain networks (which could be associated with the underlying streets) and on top of it we can measure correlations and information flow to construct the functional brain network (which could be interpreted as measuring the traffic flow).

Next to the simple statistical dependency of correlation, the transfer entropy, a measure of information flow between time series, is lately often computed in neuroscience [50, 61]. The transfer entropy between two brain regions quantifies the causal effect of one brain region on another one [2, 35, 82]. Time-delayed measures like transfer entropy can equally be used as link weights for the functional brain network and are summarized as effective connectivity measures. Effective connectivity aims to detect the influence from one brain region on another region. This time-delayed view introduces directionality in the interaction patterns and can help to construct the functional brain network as a directed network with every link being either bidirectional or being assigned one dominant direction. The directed characterization of the functional brain network offers new insights into the information flow in the human brain on a macroscopic regional level.

Though there has been increasing interest in the relation between the structural and the functional brain networks over the last years, their relationship remains insufficiently understood [90]. Based on these different kinds of brain networks, the following two research questions are the main focus of this dissertation. The first question focuses on the building blocks of the functional brain networks in order to understand the emergence of global communication outcomes. Then, with a better understanding of the important links and higher-order constructions of the functional brain network, the second research question aims at finding the origins of these communication patterns in the underlying structural brain network.

RESEARCH QUESTION 1: WHAT ARE THE MOST IMPORTANT LINKS AND MOTIFS IN FUNCTIONAL BRAIN NETWORKS WITH RESPECT TO GLOBAL INFORMATION FLOW?

After computing the functional or effective connectivity between brain regions, the functional brain network is a fully weighted network whose topology is often masked by measurement noise. Before applying the variety of measures from network science, a network representation of the functional brain network that includes only the most important links for the global information flow while disregarding noise and higher levels of redundancy needs to be found without setting an arbitrary threshold. The choices in this step of the analysis have proven to be crucial to the outcomes of many network measures [118]. One additional challenge here is that a network representation should allow for an unbiased comparison between different kinds of networks. Especially for neuroscience, enabling the comparison between the functional brain networks of patients suffering from neurological disorders and healthy controls is very important. One approach to conquer this influential choice has been to extract the minimum spanning tree of the network [92], which has also been referred to as the super-highways of a network [126]. The minimum spanning tree (MST) has been successful in a lot of recent studies to comprise important features of functional brain networks and distinguish between patients and healthy controls [98, 106, 121]. Enlarging this representation towards a denser network based on the MST but including alternative pathways has been the motivation behind our analysis of the shortest paths in functional brain networks. Proposing the network representation of the so-called union of shortest path trees for functional brain networks and use this method to rank all links with regard to their importance for the global information flow is the focus of Chapters 2 and 3 of this thesis.

In Chapter 4, we then shift to the effective connectivity and the directed functional interactions in brain networks. There, we analyze the most important higher-order building blocks of the functional brain networks in the form of motifs that give rise to the global patterns of information flow.

RESEARCH QUESTION 2: WHICH STRUCTURAL NETWORK PROPERTIES DRIVE THE FUNCTIONAL INTERACTIONS?

As mentioned before, there is not one brain network but instead many representations of the same complex system. The relationships, however, between those different kinds of brain networks are still unclear. The field of neuroscience can only really benefit from its data variety once the relations between the different representations of the human brain can be understood. In this dissertation, we focus on the relation between the structural and the functional brain networks. This relation between structure and function is a rather general question, not necessarily limited to the field of complex brain networks. For many different spreading processes on networks, it remains yet to be investigated how the structural network properties influence the emerging dynamics [72, 73]. The main objective here is to identify the structural network properties that drive the functional interactions in the human brain. In this thesis, we approach this question from different angles. In Chapter 5, we take a rather straightforward approach to investigate the relation between structure and function in brain networks by analyzing a mapping between the connectivity matrices of the different empirical networks. After investigating the relation between empirical matrices, we analyze the properties of the structural network that drive those information flow patterns by applying a simple model of activity spread on the human connectome in Chapter 6.

2

THE UNION OF SHORTEST PATH TREES OF FUNCTIONAL BRAIN NETWORKS

2.1. INTRODUCTION

Recently, the shortest paths between brain regions were found to be crucial to understand functional networks in terms of structural networks [41] and pathological network alterations in brain diseases. Structural or functional brain networks in patients with neuropsychiatric diseases are often characterized by a reduced global efficiency, which is proportional to the inverse of the shortest paths. However, the shortest paths of the functional brain network have merely been analyzed with regard to their average length. Using all shortest paths as an alternative topology for the functional brain network is a new approach.

Several sampling methods on functional brain networks set a threshold or fix the link density to thin the complete weighted graph. However, these methods have disadvantages: the choice of the a priori chosen threshold or link density is often arbitrary and, in addition, different link densities can lead to different results [118]. Constructing the minimum spanning tree (MST) of the functional brain network has provided insight in the differences between patients suffering from brain disorders and healthy controls in a lot of recent studies [28, 92, 99, 106, 121]. An advantage of the MST lies in its independence of the transformation of the weights as long as their ranking is unaltered. There exists only one unique path from a node to another node in the MST, which limits more advanced analysis.

Analyzing shortest paths is a common practice after reducing the complete graph of the functional brain network with any of the existing sampling methods. [15] suggested that the brain is always trying to reduce material and metabolic costs when transporting information. Thus, the concept of shortest paths fits into the current understanding of the brain function. Extracting all shortest paths of the original complete graph can be interpreted as focusing on the backbone or the main functional highways of the brain network. We intend to represent the most important connections of the functional brain network based on global network properties and not only on the ranking of the link weights among each other.

In the present study, we propose the union of shortest path trees (USPT) as a new sampling method for the functional brain network. This sampling method has been successfully applied before on a variety of complex networks [117]. To construct the USPT, we first identify the shortest path tree rooted at each node in the network. The shortest path tree rooted at a node consists of all shortest paths from this node to all the other nodes [114]. The union of all shortest paths from a single node to the rest of the network always results in a tree [111]. Furthermore, we can unite these shortest path trees to obtain the USPT $G_{\cup_{spt}}$ of our network G [117]. The USPT is determined by the topology of the underlying network and its link weight structure (the set of weights on the links in G) [117]. Furthermore, if all link weights equal 1, the USPT is the same as the underlying network because all information then flows over the direct pathways between the nodes.

The properties of the USPT have been analyzed in various studies [114, 117]. The USPT, not the underlying network, determines the network's performance [117]. Another important property of the USPT is that it always includes the MST [117] (Figure 2.1). The regime, where the USPT coincides with the MST is called the

---

This chapter has been published in J. Meier, P. Tewarie and P. Van Mieghem, *The Union of Shortest Path Trees of Functional Brain Networks*, Brain Connectivity, **5**(9), pp. 575-581 (2015).

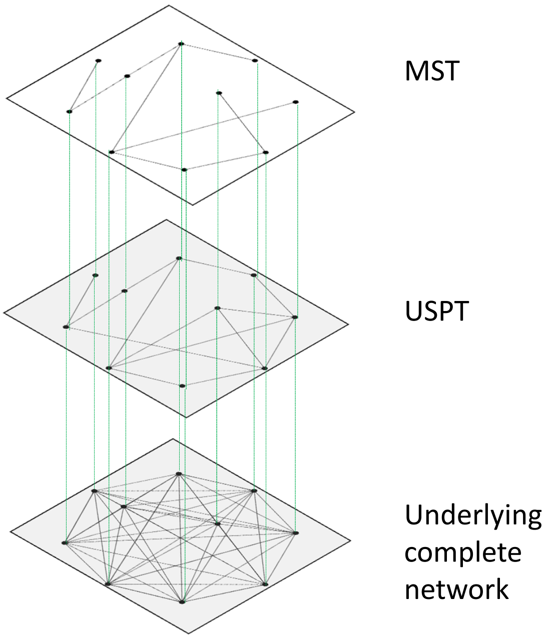

Figure 2.1: Visualization of a complete network with its corresponding USPT (union of shortest path trees) and MST (minimum spanning tree).

strong disorder regime, the counterpart is the weak disorder regime [114, 116]. In the strong disorder regime, all traffic in the network follows only links in the MST, while in the weak disorder regime, a transport may follow other paths. Analogous to the flow of electrical current, we may regard the strong disorder regime as the superconductive phase, whereas the weak disorder corresponds to the resistive phase, where electrons follow many paths between two different voltage points.

In many real-world networks, the information is assumed to flow over the shortest path to optimize transportation costs. The derivation of $G_{\cup_{spt}}$ can be regarded as a filter for the weights that are not important for the overall transportation flow in the brain. By reducing the network to the union of its shortest paths, only those paths are maintained that have a high probability that information is transported along them. The topology of $G_{\cup_{spt}}$ represents the highways of the brain. The goal of this chapter is to evaluate and apply this USPT sampling method to the functional brain network and to find first differences between patients and healthy controls.

In the following, we will interpret the link weights of the functional brain network as communication probabilities and, based on this interpretation, we will construct and analyze the USPT. We will examine the results of this new USPT sampling method by using empirical data from healthy controls and multiple sclerosis (MS) patients and demonstrate that the USPT is sensitive to disease alterations and that our USPT method can be used to discriminate between healthy and pathological conditions.

2.2. MATERIALS AND METHODS

2.2.1. DATA ACQUISITION

In this section, we explain the reconstruction of functional brain networks from our magnetoencephalography (MEG) measurements. Our data set consisted of 68 healthy controls and 111 MS patients, which is a larger but overlapping group as in [98, 99]. Details with regard to data acquisition and postprocessing can be found in our previous article [99]. In short, MEG data were recorded using a 306-channel whole-head MEG system (ElektaNeuromag, Oy, Helsinki, Finland). Fluctuations in magnetic field strength were recorded during a no-task eyes-closed condition for 5 consecutive minutes. A beamformer approach was adopted to project MEG data from sensor space to source space [49]. This beamformer approach can be regarded as a spatial filter that computes the activity within brain regions based on the weighted sum of the activity recorded at the MEG channels. We then used the automated anatomical labeling (AAL) atlas to obtain time series for 78 cortical regions of interest (ROIs) [40, 104]. For each subject, we chose five artifact- free epochs of source space time series [28, 99, 106]. Six frequency bands were analyzed: *delta* (0.5 – 4 Hz), *theta* (4 – 8 Hz), lower *alpha* (8 – 10 Hz), upper *alpha* (10 – 13 Hz), *beta* (13 – 30 Hz), and lower *gamma* bands (30 – 48 Hz).

Subsequently, for each epoch and frequency band separately, we computed the phase lag index (PLI) between all time series of the 78 ROIs to obtain the link weights for our functional brain networks [91, 93]. The PLI can take values between 0 and 1 and is a measure that captures phase synchronization by calculating the asymmetry of the distribution of instantaneous phase differences between time series. Formally, the PLI is defined as

$$PLI = |\langle \text{sign}[\sin(\Delta\Phi(t_k))]\rangle|, \tag{2.1}$$

where $\Delta\Phi(t_k)$, for $k = 1, ..., m$; $m \in \mathbb{N}$, is the time series of phase differences evaluated for time steps $t_1, ..., t_m$, $\langle\cdot\rangle$ denotes the average and $|\cdot|$ the absolute value. High values of the PLI refer to a strong interaction or synchronization between two time series while avoiding bias due to volume conduction.

As a next step, for each epoch we constructed an $N \times N$ weight matrix W with elements w_{ij}, each representing the PLI of the pair of regions, i and j. This symmetric weight matrix W can be interpreted as a complete weighted graph on N nodes ($N = 78$). Last, we averaged over all five weight matrices belonging to each epoch to obtain one weight matrix per person and to ensure independent samples for statistical testing. All further mentioned weight matrices in this chapter refer to matrices with PLI values as entries.

2.2.2. LINK WEIGHTS IN FUNCTIONAL BRAIN NETWORKS AS COMMUNICATION PROBABILITIES

A network can be represented by a graph G consisting of N nodes and L links. Each link $l = i \to j$ from node i to j in G can be specified by a link weight $w_l = w_{ij} = w(i \to j)$. Assume a path from a node A to node B in our network G. We denote this path by $\mathcal{P}_{A\to B} = n_1 n_2 ... n_{k-1} n_k$ with hopcount (sometimes also called the length) $k \in \mathbb{N}$, where $n_1 = A$, $n_k = B$ and $n_2, \ldots, n_{k-1}$ represent the distinct nodes along the path [113]. The weight of a path $\mathcal{P}_{A\to B}$ is usually defined as

$$w(\mathcal{P}_{A\to B}) = \sum_{l \in P_{A\to B}} w_l \tag{2.2}$$

The shortest path $\mathcal{P}^*{}_{A\to B}$ between A and B equals that path that minimizes the weight $w(\mathcal{P}_{A\to B})$ over all possible paths from A to B, hence, $w(\mathcal{P}^*{}_{A\to B}) \le w(\mathcal{P}_{A\to B})$. The efficient Dijkstra algorithm to compute the shortest path requires that link weights are non-negative [110]. If the link weights are real, positive numbers, in most cases – though not always –, the shortest path $\mathcal{P}^*{}_{A\to B}$ is unique. Other definitions of the weight of a path are possible [110, Ch. 12], such as $w(\mathcal{P}_{A\to B}) = \prod_{l\in P_{A\to B}} w_l$ or $w(\mathcal{P}_{A\to B}) = \min_{l\in P_{A\to B}} w_l$. Here, we will deduce a new definition of the weight of a path, particularly geared to functional brain networks.

The PLI, defined in Equation (2.1), is an approximation of the probability of phase synchronization between time series. Therefore, we can interpret the PLI as the communication probability between two nodes in the functional brain network. The PLI also implies symmetry in the communication direction so that $w_{ij} = w_{ji}$ and we further confine ourselves to undirected links. With this interpretation, the link weight $w_{ij} = w(i \leftrightarrow j)$ between node i and j represents the probability that the end nodes i and j are communicating or that information is transmitted over this functional link. The PLI assigns a high link weight to strongly communicating nodes. Likewise, low values of the PLI represent low probabilities that the end nodes are communicating. The weight of a path between brain regions, A and B, can then be interpreted as

$$\begin{aligned} w(\mathcal{P}_{A\to B}) &= \Pr[\text{information is transported along the path } \mathcal{P}_{A\to B}] \\ &= \Pr[\text{every link in } \mathcal{P}_{A\to B} \text{ transports the information}] \\ &= \Pr[\bigcap_{l\in\mathcal{P}_{A\to B}} \text{link } l \text{ transports information}]. \end{aligned}$$

To proceed, we assume independence between different link weights so that

$$\Pr[\bigcap_{l\in\mathcal{P}_{A\to B}} \text{link } l \text{ transports information}] = \prod_{l\in\mathcal{P}_{A\to B}} \Pr[\text{ link } l \text{ transports information}].$$

Introducing our interpretation of the link weights in the functional brain network as communication probabilities,

$$w_l = w_{ij} = \Pr[\text{link } i \leftrightarrow j \text{ transports the information}],$$

we find the weight of the path between A and B

$$w(\mathcal{P}_{A\to B}) = \prod_{1\le i\le k-1} w_{n_i n_{i+1}}. \tag{2.3}$$

Table 2.1: p-Values for the two-sample t-test for differences in mean link density of the USPT (under the link weight transformation $v_{ij} = -\ln(w_{ij})$) between MS patients and controls for all frequency bands. The annotation * means that the p-value is under the 5% significance level.

Frequency band	p-Value
delta	0.0245^*
theta	$< 0.001^*$
alpha1	0.3297
alpha2	0.0902
beta	0.0588
gamma	0.2907

The assumption of independence between the link weights is debatable. Identifying the dependency structure, thus the correlations between the different links in the functional brain network, is a complex task. In this study, we approximate all link weights as being independent of each other and we thus ignore correlations.

Between any pair of nodes, A and B, in our network, we identify the path with the highest probability of successful communication between these two nodes, which is the path that maximizes $w(\mathscr{P}_{A\to B})$ in Equation (2.3). The path between nodes, A and B, which maximizes $w(\mathscr{P}_{A\to B})$, is defined as the shortest path $\mathscr{P}^*_{A\to B}$ between two nodes. Since $0 \le w_{ij} \le 1$ by the definition [Eq. (2.1)] of the PLI, we rewrite Equation (2.3) as

$$w(\mathscr{P}_{A\to B}) = \exp\left(\sum_{1\le i\le k-1} \ln w_{n_i n_{i+1}}\right) = \exp\left(-\sum_{1\le i\le k-1} |\ln w_{n_i n_{i+1}}|\right). \tag{2.4}$$

and observe that maximizing $w(\mathscr{P}_{A\to B})$ is equal to minimizing the sum of the transformed link weights $-\sum_{1\le i\le k-1} \ln w_{n_i n_{i+1}}$. Consequently, Dijkstra's shortest path algorithm can be used after transforming the weights $v_{ij} = -\ln(w_{ij})$ for all $1 \le i, j \le N$. This transformation approach is often used in computer networks (see e.g. p. 313 in [110]).

As mentioned earlier, there are different link weight transformations apart from the interpretation of the link weights as communication probabilities. A basic transform is a polynomial link weight transformation $v_{ij} = (w_{ij})^{\alpha}$, for example, in [114] and [11]. Interestingly, we can rephrase our probabilistic approach in terms of the polynomial link weight transformation as

$$v_{ij} = -\ln w_{ij} = \frac{d}{d\alpha}\left(\exp\left(-\alpha \ln w_{ij}\right)\right)\Big|_{\alpha=0} = \frac{d}{d\alpha}\left(w_{ij}^{-\alpha}\right)\Big|_{\alpha=0}.$$

where α can be regarded as an extreme value index of the link weight distribution [113, Chapter 16]. When $\alpha < \alpha_c$, the USPT operates in the strong disorder regime and all information flows over the MST, whereas, for $\alpha > \alpha_c$, information traverses more links in the USPT. The critical value α_c can be associated with a phase transition in the graph's link weight structure, for which we refer to [114, 116, 117].

2.3. RESULTS

After constructing the USPT of the functional brain network under the link weight transformation $v_{ij} = -\ln(w_{ij})$, we can analyze the resulting link densities of the different USPTs. The mean and the standard deviation of the number of links in the USPT are plotted for the different frequency bands in Figure 2.2. We can infer from Figure 2.2 that on average the number of links needed for the USPT does not differ much over all frequency bands, except that the *alpha1* and *alpha2* band seem to have a lower mean link density of their USPT than all the other frequency bands. Overall, the mean link density of the USPT varies between 98.27% and 99.98%, which is too dense to obtain a meaningful visualization of the resulting network.

Furthermore, we tested the differences in mean link density between MS patients and controls with a two-sample t-test. We found that MS patients have on average a significantly lower link density than healthy controls in the *theta* and*delta* frequency band under the 5% significance level (Table 2.1).

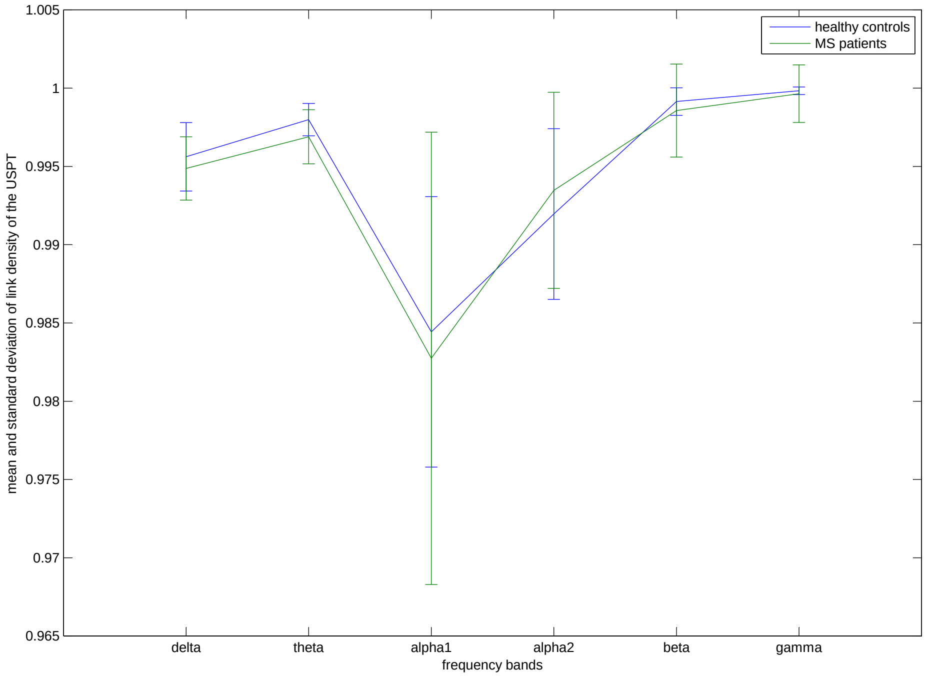

Figure 2.2: Plot of the mean value of the link density in the USPT and an error bar of length twice the standard deviation for healthy controls and MS patients over different frequency bands under the link weight transformation $v_{ij} = -\ln(w_{ij})$.

2.4. DISCUSSION

Unlike the MST method where the number of links $L = N - 1$, we found that the USPT of the functional brain network has a specific link density so that the number of links L in the USPT is different for different brain networks. The difference in the number of links influences graph metrics, but the number of links itself informs us about the spread of transport in the brain. The links in the USPT are those links over which the information is flowing. Thus, the link density in our method is not fixed arbitrarily, but emerges as a property of the underlying transport or communication structure. Hence, the differences in link densities contain meaningful information about the brain network topology and performance. A nearly complete graph, as the USPT here with relatively low standard deviation, shows that this path weight interpretation belongs to the weak disorder regime [114, 116]. Thus, the information in the functional brain network seems to flow over more links than just the MST topology. Moreover, the high link density shows that the communication flow in the functional brain network is probably spread across nearly all possible connections. A high link density in the USPT means that in most cases the direct communication between two brain regions is preferred. Thus, the length (or hopcount) of the shortest path is overall short, which confirms the assumption that the functional brain network operates as a small world [14].

In the probabilistic approach to generate the USPT, no *a priori* parameter or link weight threshold needs to be fixed arbitrarily. Besides the interpretation of the shortest path as a communication channel, the only assumption in this approach is that all links (and link weights) are independent. Disadvantages of the USPT sampling method lie in the dependence on the chosen link weight transformation. However, our link weight transformation arises as a consequence of the interpretation of the link weights, measured by the PLI, as communication probabilities and is therefore not arbitrarily chosen.

The observation that the link density in the USPT for patients is nearly always lower on average than the link density for healthy controls shows that MS patients seem to have less links for brain communication. Therefore, the average path length becomes longer and thus the communication within the functional brain network less effective.

On nearly the same data set, a more classic network analysis has been performed in [99]. One of the findings in [99] was that for MS patients, there has been a higher mean PLI value in the *delta* and *theta* frequency band and a lower mean PLI value in the *alpha2* frequency band. The higher mean PLI value in the *delta* and *theta* band seems to align with our results of a lower link density for the USPT for patients. The correlation between the overall mean of the link weight distribution and the USPT is not yet clear and needs to be investigated in future research (see Appendix Figures 2.3 and 2.4). Additionally, for the $theta$ band, the other study [99] found patients to have a significantly higher (normalized) path length in their functional brain network, which implies a more regular topology for patient networks. Since a larger normalized path length also indicates a larger path length in the USPT and, equivalently, a lower link density in the USPT, this finding agrees with our current study in the *theta* band.

To sum up, we found that our USPT method picks up most of the differences found in a previous study between MS patients and controls. Overall, this previous study [99] found significant differences for the functional brain network between MS patients and controls in three frequency bands, *delta*, *theta*, and *alpha2*, with the help of conventional network analysis and testing the overall mean PLI values against each other. The performed MST analysis on the same data set seemed to only find the differences in the *alpha2* band [99] and provides meaningful interpretation for those differences concerning the overall integration of communication that seems to be disrupted in MS patients. Our USPT method enlarges the analysis and incorporates the differences in the remaining frequency bands, the *delta* and *theta* bands. For these frequency bands, the USPT method can enhance our insight concerning the overall communication in the functional brain networks of MS patients. In another study, Goñi and co-authors [41] applied the same link weight transformation, $v_{ij} = -\ln w_{ij}$ to the structural brain network without giving further rationale for this specific transform. Furthermore,Goñi et al. [41] also confirmed that the shortest path weights calculated under the link weight transformation $v_{ij} = -\ln w_{ij}$ play a major role in brain network communication. This chapter provided a detailed argument on why the $v_{ij} = -\ln w_{ij}$ transform is a reasonable choice for the link weights of the functional brain network and showed that the topology of the resulting shortest paths can be used to differentiate between patients and healthy controls.

2.5. CONCLUSION

We found statistically significant differences between MS patients and controls while analyzing the link density of their USPT under the link weight transformation $v_{ij} = -\ln(w_{ij})$ derived from the interpretation of the link weights as independent communication probabilities. Those differences were found in the same frequency bands as in a previous study on a similar data set [99]. As a conclusion of our findings, we propose the USPT under the link weight transformation $v_{ij} = -\ln(w_{ij})$ as a new sampling method for extracting differences between the functional brain networks of patients and healthy controls. The interpretation of the link weights as communication probabilities leads to a USPT of the functional brain network that includes all important links of the global brain communication.

2.6. APPENDIX: LINK WEIGHT DISTRIBUTION OF FUNCTIONAL BRAIN NETWORKS

In this section, we analyze the link weight distribution of the functional brain network since the USPT does depend directly on the underlying link weight distribution [114]. If we analyze the histogram of the link weights per frequency band, Figure 2.3 and 2.4 illustrate that (after averaging over five epochs) the accumulated link weight histogram for the *delta* frequency band and *alpha1* frequency band seem to follow a Gamma distribution.

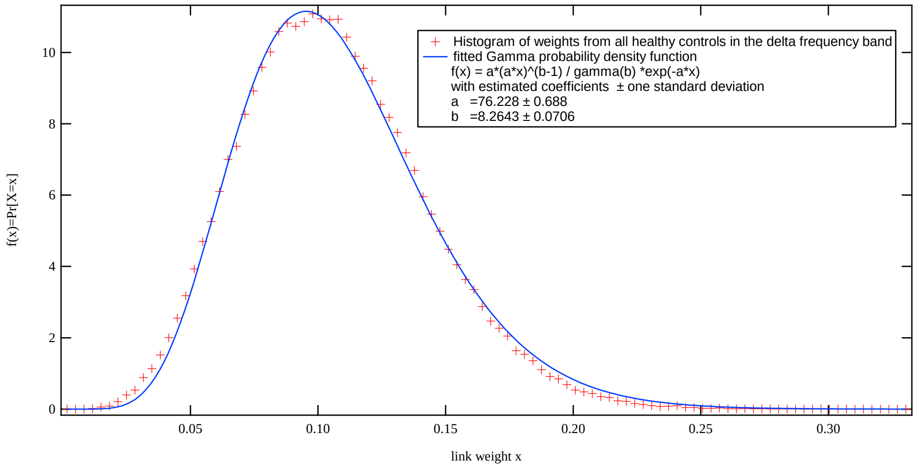

Figure 2.3: Histogram of all the link weights (after averaging over five epochs) from all PLI matrices of the *delta* frequency band of all 68 healthy controls.

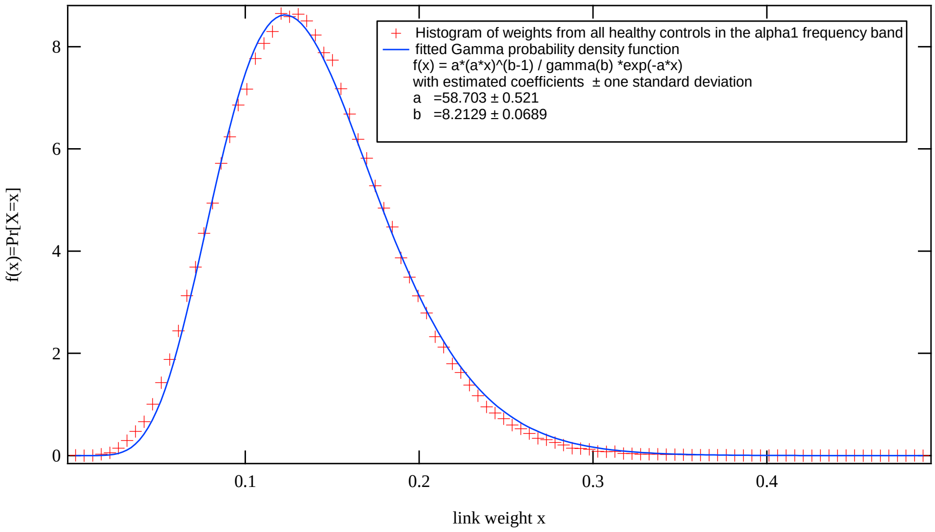

Figure 2.4: Histogram of all the link weights (after averaging over five epochs) from all PLI matrices of the *alpha1* frequency band of all 68 healthy controls.

3

GENERALIZED α-TREE SAMPLING METHOD SHOWS LINK IMPORTANCE BEYOND BETWEENNESS

3.1. INTRODUCTION

Extracting all shortest paths for different networks often leads to different link density causing difficulties for an unbiased comparison of those network topologies since most network metrics are influenced by link density. In this study, we propose a new general sampling method for any complex weighted network based on the shortest path structure, which not only reveals the link ordering with respect to shortest paths but also enables comparisons between the shortest path structures of different networks.

The union of shortest path trees (USPT) as an alternative reduced topology has proved an interesting representation for many different complex networks [117, 123] (Chapter 2). The union of shortest paths of a weighted graph G is the subgraph of G that contains all the links that belong to a shortest path in G. The union of all shortest paths in G equals the union of the shortest path trees $G_{\cup_{SPT}}$ (USPT) rooted at each node in G. The properties of the USPT have been analyzed before in various studies [114, 117], where an important attribute is that the USPT always includes the Minimum Spanning Tree (MST) [117]. The regime where the USPT coincides with the MST is called the strong disorder regime, the counterpart is the weak disorder regime [114, 116]. One may compare the strong disorder regime with the superconductive phase for electrical currents in solids, while the weak disorder corresponds with the dissipative phase, where the resistance of the solid causes the electrical flow between two voltage points to spread over all possible paths between those two points. The USPT is determined by the topology of the underlying network and its link weight structure or distribution [117]. For the length of the shortest path, a critical number of nodes N has been found depending on the link weight distribution that symbolizes the transition from weak to strong disorder [11].

In this study, we present a new general sampling method based on shortest paths which can be applied to any complex weighted network with any underlying link weight distribution. Via a parameter α, the link density of the networks can be tuned, always resulting in the USPT of the network (for examples see Figures 3.1 and 3.2). After describing the construction of those α-trees, the influence of the tuning parameter α on the properties of the resulting network topologies is analyzed. Furthermore, the USPT sampling method reveals a new link ordering based on the importance of a link for the shortest path structure. Finally, we apply this new sampling method of the so-called α-trees to compare functional brain networks of multiple sclerosis (MS) patients and healthy controls.

3.2. CONSTRUCTION OF α-TREES

Let w denote an arbitrary link weight in a graph $G(N,L)$ with value $w \in [0,1]$. We construct a new graph $G_\alpha(N,L)$ in which all link weights are transformed and the new value for the arbitrary link is $V = h(w,\alpha)$, where α is a control parameter. Here, we choose

$$h(y,\alpha) = y^{\frac{1}{\alpha}} \tag{3.1}$$

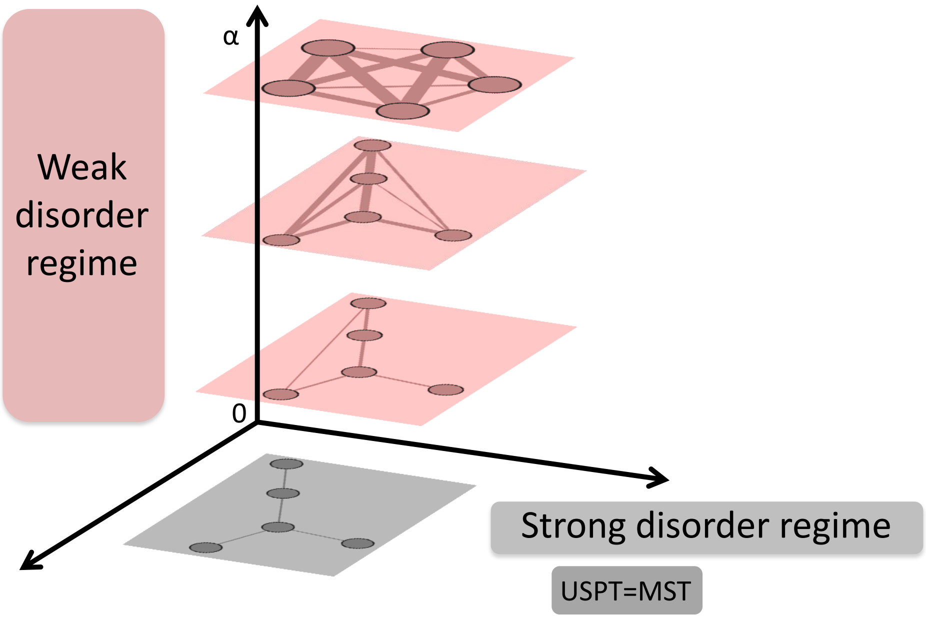

Figure 3.1: Example of the USPT for different values of α.

where $y \in [0,1]$. The motivation for this choice of transform is the following. If w has the distribution function

$$F_w(x) = \Pr[w \le x]$$

then V has the distribution function

$$\Pr[V \le x] = \Pr\left[w^{\frac{1}{\alpha}} \le x\right] = \Pr\left[w \le x^\alpha\right] = F_w\left(x^\alpha\right)$$

Since only links with small link weights appear in the shortest path (and thus in the USPT), mainly small values of x are important. Following the arguments in [113, p. 414], we assume that $F_w(x)$ is a regular distribution that possesses a Taylor series at each point $x \in [0,1]$. Hence, applying the Taylor series around $x = 0$,

$$\begin{aligned} F_w(x) &= F_w(0) + F'_w(0)\,x + O\left(x^2\right) \\ &= f_w(0)\,x + O\left(x^2\right), \end{aligned}$$

where $f_w = F'_w$, shows that, for small x,

$$\begin{aligned} \Pr[V \le x] &= F_w\left(x^\alpha\right) \\ &= f_w(0)\,x^\alpha + O\left(\left(x^\alpha\right)^2\right) \end{aligned}$$

illustrating that V follows a polynomial distribution with extreme value index α for small x. This observation allows us to import the theory and scaling laws of polynomial links weights [114, 117]. In contrast to these previous papers, where several instances of graphs with the same polynomial link weight distributions were studied, here, one single graph with an initial link weight distribution $F_w(x)$ is transformed in different graphs G_α with near to polynomial link weights. After the link weight transformation (3.1), we construct the USPT of the graphs G_α, which we denote by U_α or α-trees (for an example see Figure 3.2b).

The analysis shows that the initial link weight distribution $F_w(x)$, given that it is regular, looses influence after the transformation (3.1). The constant $f_w(0)$ is, for small x, the only reference to the original link weight distribution after the transformation (3.1). Thus, the parameter α, also called extreme value index, plays a more dominant role than $F_w(x)$. As demonstrated in the sequel, the main role of the initial link weight distribution $F_w(x)$ is to assign an ordering of the link weights in the graph. Therefore, we can confine ourselves to two different underlying link weight distributions, uniformly distributed link weights in the interval $(0,1)$ and exponentially distributed link weights with mean 1.

(a) Step function of the number of links of α-trees.

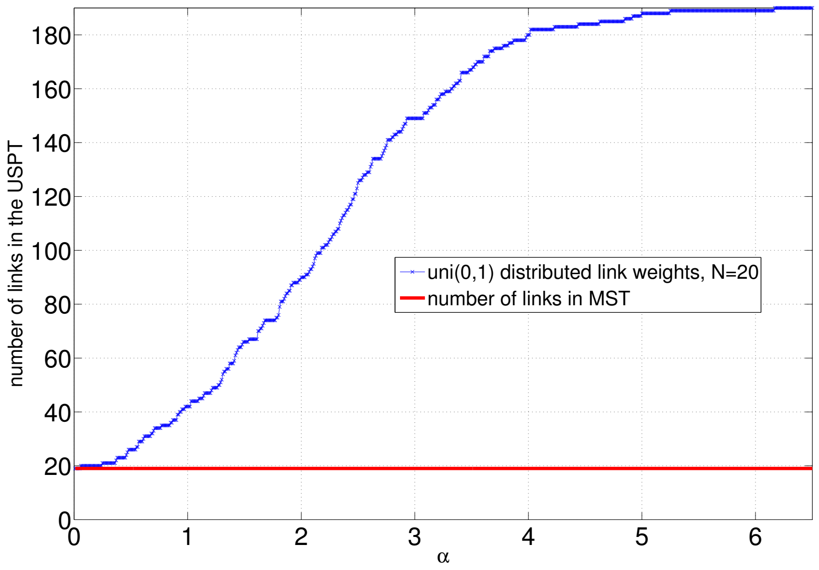

(b) Visualization of the α-trees with different number of links.

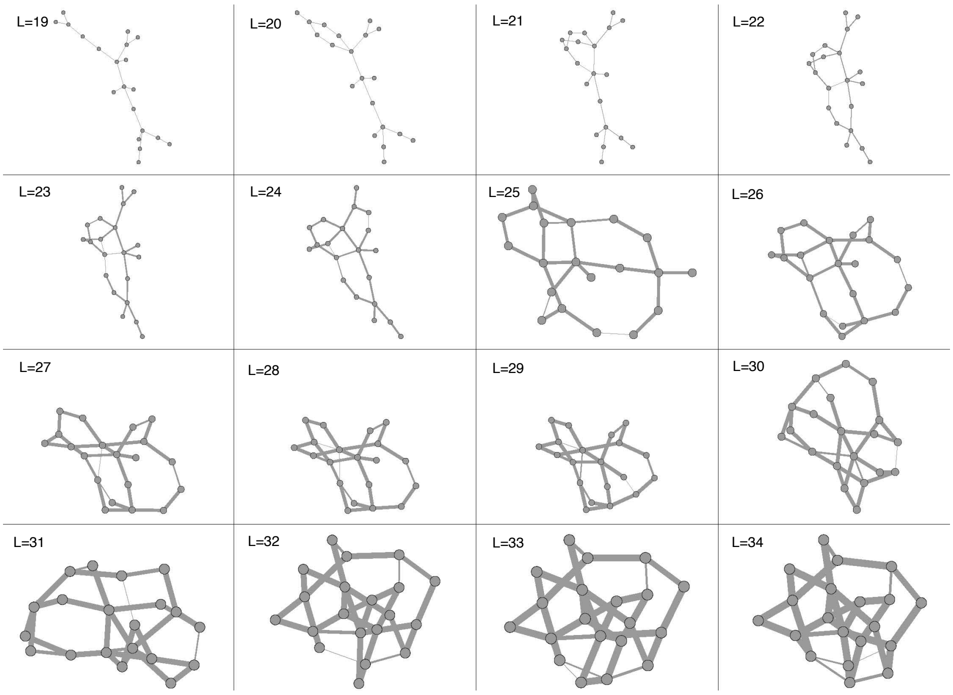

Figure 3.2: (a) Example of the step function of the number of links depending on the tuning parameter α for uniformly distributed link weights in the interval $(0,1)$ and $N = 20$. (b) Visualization of the corresponding α-trees with different number of links starting from the MST with $L = N - 1$.

In Figure 3.2, we plotted α against the number of links of the USPT based on an example network with $N = 20$ nodes and exponentially distributed link weights with rate 1. We observe that the number of links in the USPT can be changed from $L = N-1$ (MST) to $L = \binom{N}{2}$ (the complete graph K_N) by tuning the parameter α. In [114] and [116] Van Mieghem et al. showed that there exists a critical $\alpha_c > O\left(L^{-2}\right)$, where L is the number of links in the original graph, and for all $\alpha \leq \alpha_c$, the USPT U_α is equal to the MST. The estimate of the critical α_c of the phase transition was improved in [114] to $\alpha_c = O(N^{-\beta})$, where the power law exponent β reflects the underlying graph. The best estimates so far are described in [117]. The α-regime $[0, \alpha_c]$ corresponds to the strong disorder regime, where all transport flows over the backbone (MST) of the network, while the α-regime where $\alpha > \alpha_c$, is the weak disorder regime, where many paths are used for transport. In our case, α_c is the first "jump point" from the $N-1$ links in the MST to N links (see Figure 3.2). More general, all the α-values, for which U_α is the same, constitute an α-interval and the beginning of the j-th α-interval is defined by the *jump point* ξ_j, where by definition $\xi_0 = 0$ and $\xi_1 = \alpha_c$. The number of links in U_{ξ_j} equals $L_{\xi_j} = N - 1 + j$ for $0 \leq j \leq \binom{N-1}{2}$. Further, we denote the link density of a USPT by $l_\alpha = L_\alpha / \binom{N}{2}$.

For very small values of α, we faced some numerical problems since the exponent of the weight transformation function (3.1) becomes very big and thus the link weights are all very small. By applying a very high precision, these numerical problems could be solved for most networks (for the exact number of necessary digits see [114]). However, in some cases, a single very small original link weight can be transformed with a small enough α-value and rounded to 0 before α_c was reached. As we observe later in the results, these cases probably cause the discrepancies for small values of α.

3.3. PROPERTIES OF α-TREES

3.3.1. LINK DENSITY OF α-TREES

In Figure 3.3a, we plotted the link density l_α versus α based on uniformly and exponentially distributed link weights. For these plots (Figure 3.4), we calculated the average jump point, denoted by $\tilde{\xi}_{l_\alpha}$, based on 10^4 realizations of a network with $N = 20$ nodes, each with different link weights, though drawn from one of the distributions. The average jump point is representative since the 80% confidence interval offers a quite narrow band around the average value (see Appendix Figures 3.11 and 3.12). Similar to previous studies [114], we observe a phase transition for the link density of the USPT between two extreme link densities (see Figure 3.3a). For $\alpha \to 0$, we can confirm the strong disorder regime where the USPT of the transformed link weights equals the MST. For $\alpha \to \infty$, we find that all link weights approach 1 and, thus, the USPT equals the complete graph.

It appears that (see Figure 3.3a), for both uniformly and exponentially distributed link weights, the average number of links is close to

$$E\left[l_\alpha\right] \simeq \frac{2}{N} + \frac{\left(1 - \frac{2}{N}\right)}{1 + \exp\left(-b\left(\alpha - c\right)\right)}\ , \tag{3.2}$$

which is a modified logistic function with $\lim_{\alpha\to 0} E\left[l_\alpha\right] = (N-1)/\binom{N}{2} = \frac{2}{N}$ and $\lim_{\alpha\to\infty} E\left[l_\alpha\right] = 1$ (fitted with least-square procedure). The parameter b represents the steepness and c the midpoint of the curve. Even though, the initial average jump points do not differ much for the two distributions, the increase in link density for higher jump points was less steep for the exponential than for the uniform distribution (see Figure 3.3a). To investigate the influence of the number of nodes N on the average jump point, we show the same plot for different number of nodes $N = 10, 20$ and 50 and uniformly distributed link weights in Figure 3.3b, where the curve was fitted with the logistic function from Eq. (3.2). For bigger N, the parameter b of the logistic function in Eq. (3.2), which represents the steepness of the function, decreases while the parameter c, the midpoint of the growth, increases. Except for the different starting points in link density, the overall development for different number of nodes appears to be similar (Figure 3.3b). For all curves in Figure 3.3, the logistic function provides a good fit except for very small values of $\alpha < 1$, which can probably be traced back to numerical imprecision (as mentioned in the previous section).

3.3.2. DISTRIBUTION OF α_c AND OTHER JUMP POINTS

We have discovered a precise way to determine α_c: (a) start with $\alpha = \frac{1}{L^2}$, which should, according to [116], result in U_α = MST with $N-1$ links, (b) gradually increase α until[1] the jump point $\xi_1 = \alpha_c$, i.e. when $U_{/xi_1}$ has N links. Previously in [114, 117], the determination of the critical threshold α_c was more complicated,

---

[1] Actually, the bi-section method was applied to find α_c by iteratively halving the interval around the jump point ξ_1.

(a) Link density of α-trees for different link weight distributions.

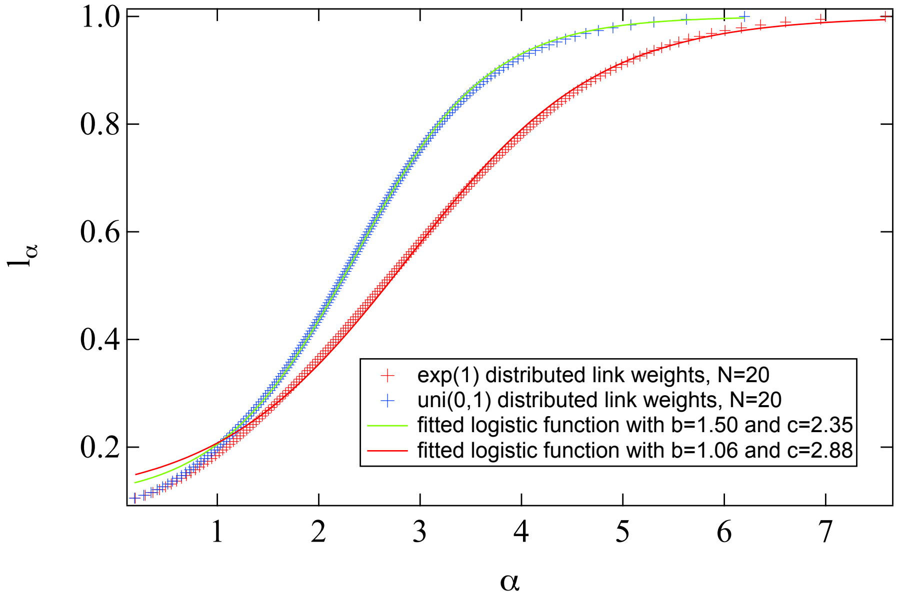

(b) Link density of α-trees for different number of nodes N.

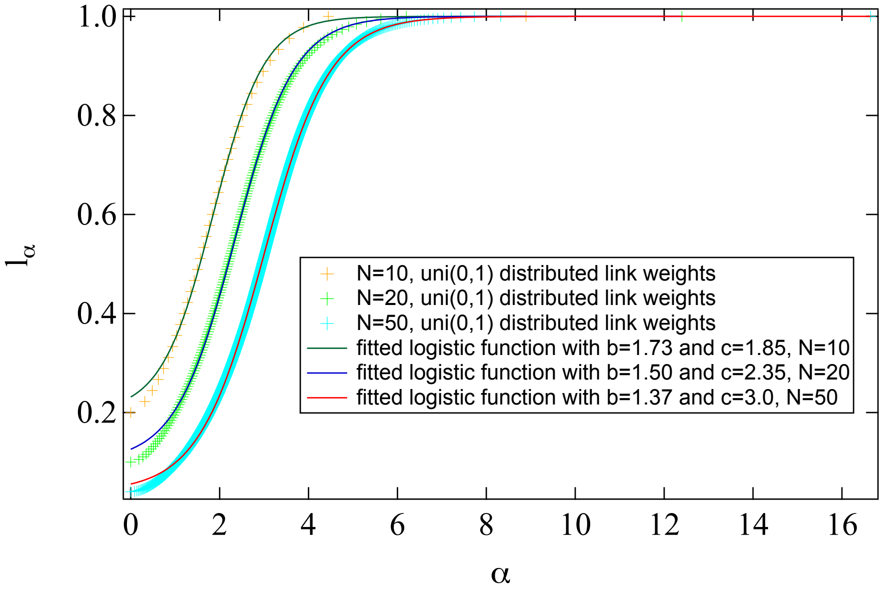

Figure 3.3: (a) The link density l_α of the α-tree versus α for 10^4 realizations of networks with $N = 20$ nodes, both for exponentially distributed link weights with mean 1 and uniformly distributed link weights in the interval $(0,1)$. (b) The link density l_α versus α for 10^4 realizations of networks with $N = 10, 20$ and 50 nodes for uniformly distributed link weights between 0 and 1. All curves were fitted with the function in Eq. (3.2) with a least-squared fitting procedure. For bigger N, the parameter b of the logistic function in Eq. (3.2), which represents the steepness of the function, decreases while the parameter c, the midpoint of the growth, increases. Except for the values of $\alpha < 1$, the fitted function describes the development quite accurately. The discrepancies for small values of α probably originate from numerical imprecision.

because each time the USPT in a graph with polynomial link weights with a certain α had to be generated and checked whether the USPT was equal to the MST. In order to have good statistics, for each α, this procedure had to be repeated at least 10^4 times. The present transform method starts from m graphs, each with link weights drawn from the distribution function $F_w(x)$, and determines in each of those graphs separately the value of the jump point $\xi_1 = \alpha_c$, described above. A similar procedure was applied to determine the second and higher jump points.

Figure 3.4 shows the distribution of $\xi_1 = \alpha_c$ and ξ_2 for uniformly and exponentially distributed link weights. We reached a good fit with a Weibull distribution

$$f(x) = abx^{b-1}\exp(-ax^b) \tag{3.3}$$

for the first and second jump point with, in each case, similar parameter values a and b for both link weight distributions (see Figure 3.4). These results suggest that the distribution of the initial jump points, α_c and ξ_2, does not depend on the specific underlying link weight distribution. The first point in both histograms (Figure 3.4) is high due to a high number of very low jump points (lower than the applied numerical threshold 10^{-4}). These outliers for very small values of α are again probably emerging from numerical imprecision causing small link weights to be rounded to 0.

Applying our computationally less exhaustive method to find the jump points, we could also easily determine all higher jump points for each graph (for histograms see Figure 3.5). From the third jump point onwards, the normal distribution provided a better fit than the Weibull distribution (see Figure 3.5). For the third jump point, the histograms of the two underlying link weight distributions, exponential and uniform, possess a big overlap whereas for increasing jump points this overlap decreases and the mean for the exponentially distributed link weights becomes higher than the average jump point for the uniformly distributed link weights.

Our results for the critical value α_c are also in line with previous studies. In [114] (and later confirmed in [117]), simulations accompanied by heuristic arguments revealed that the probability $F_T(\alpha) = \Pr[U_\alpha = MST]$, is approximately a Weibull distribution $F_T(\alpha) \approx 2^{-\left(\frac{\alpha}{\alpha_c}\right)^2}$, where they defined α_c as the median of this distribution ($\Pr\left[U_{\alpha_c} = MST\right] = 0.5$) and discovered from simulations $\alpha_c = 1.06 \cdot N^{-0.63}$. This distribution corresponds to the upper tail of our histogram for α_c since

$$F_T(\alpha) = \Pr[U_\alpha = MST] = \Pr[\alpha_c > \alpha] = 1 - \Pr[\alpha_c \le \alpha] = \exp(-a \cdot \alpha^b),$$

where the parameters a and b denote the fitted values in Figure 3.4a. Following this reasoning, we reconstructed the Weibull distribution based on polynomially distributed link weights from previous work [114] (see grey-dotted line in Figure 3.4a), which is close to our observations for the transformed exponentially and uniformly distributed link weights.

We also analyzed the spacing $\Delta\alpha_j = \xi_j - \xi_{j-1}$ for $j > 1$ (see Appendix Figures 3.9a and 3.9b) which seems to possess a power-law distribution with exponents between 2 and 3 for both underlying link weight distributions. These spacings depend on the difference between the direct added link weight and the sum of weights along the path in the α-tree before that link is added. When this difference reaches zero for increasing values of α, the link is added to the α-tree, which then also uniquely defines the corresponding jump point for this link.

3.3.3. A NEW LINK ORDERING BASED ON THE α-TREES

The following USPT Inclusion Theorem shows that the USPT with smaller value of α is always included in the USPT with larger value of α.

Theorem 1 (USPT Inclusion Theorem) *If* $\alpha_1 \ge \alpha_2 > 0$, *then* $U_{\alpha_2} \subseteq U_{\alpha_1}$.

The USPT Inclusion Theorem 1 relies on the property that *the ordering of the weights of all the links is independent of* $\alpha > 0$. Indeed, we order the original set of link weights in $G(N,L)$ as $w_{(1)} \ge w_{(2)} \ge \ldots \ge w_{(L)}$, where $w_{(i)}$ denotes the i-th smallest link weight and $1 \le i \le L$. After the link weight transformation (3.1), the ordering of the link weights is unchanged,

$$w_{(1)}^{\frac{1}{\alpha}} \ge w_{(2)}^{\frac{1}{\alpha}} \ge \ldots \ge w_{(L)}^{\frac{1}{\alpha}}$$

because $x^{\frac{1}{\alpha}}$ is increasing in x (for each value of $\alpha > 0$).

(a) Histogram of α_c.

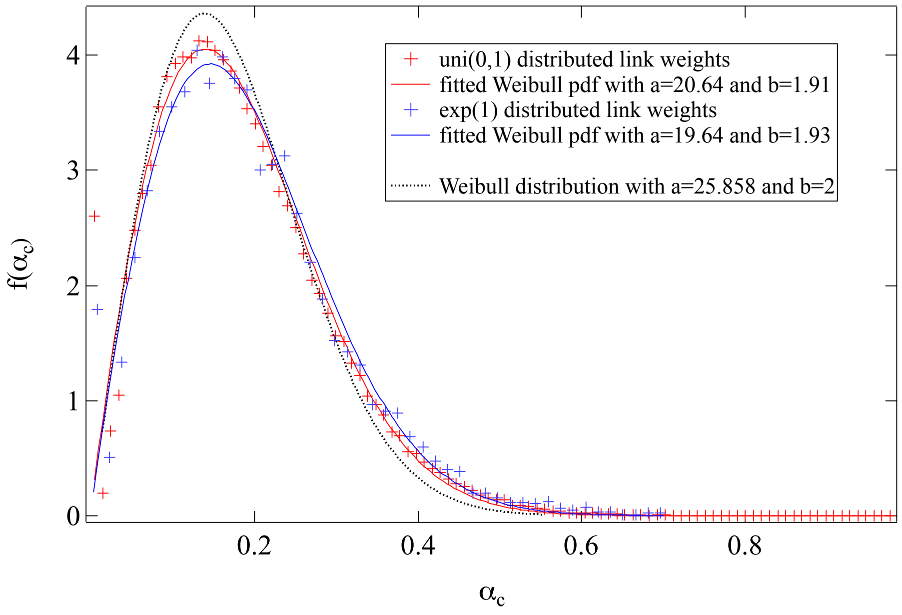

(b) Histogram of the second jump point.

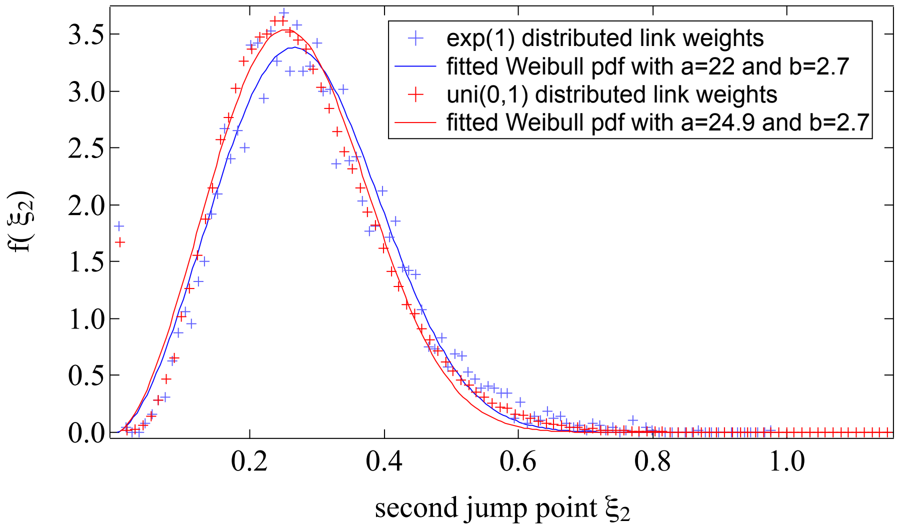

Figure 3.4: (a) Histogram of α_c from 10^4 generated matrices from the uniform $(0,1)$-distribution and exp(1) distribution, respectively, for $N = 20$ with a fitted Weibull distribution $f(x) = abx^{b-1}\exp(-ax^b)$. The grey-dotted line represents the fitted Weibull distribution from previous work (Van Mieghem and Magdalena, 2005). (b) Histogram of the second jump point for the same matrices with a fitted Weibull distribution. The first point in both histograms is high due to a high number of jump points that are very low (lower than the numerical threshold 10^{-4}).

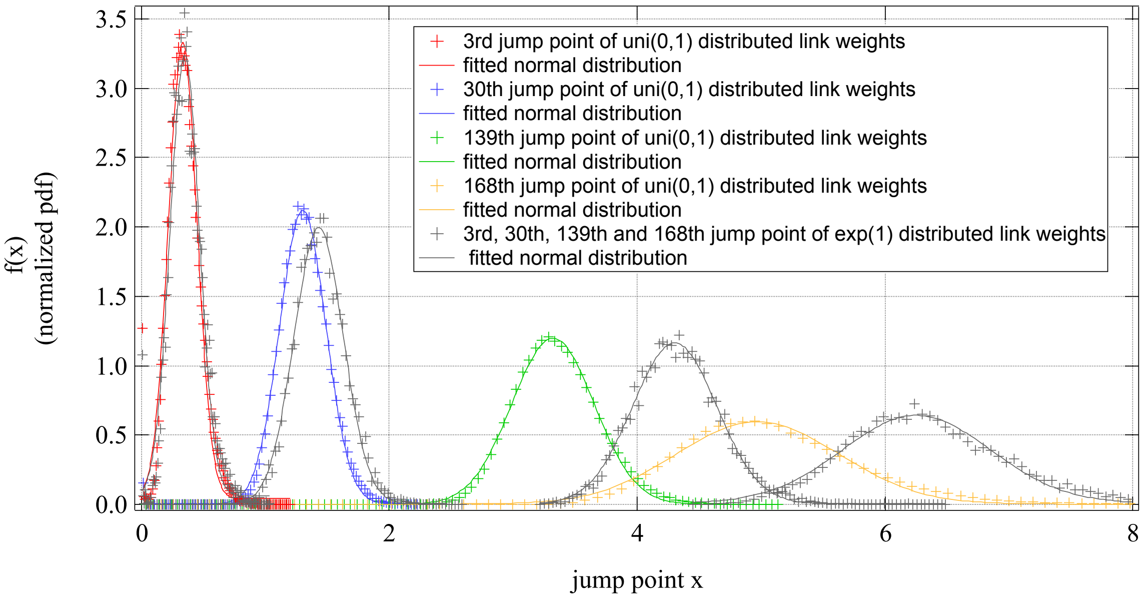

Figure 3.5: Histograms of higher jump points from 10^4 generated matrices from the uniform $(0,1)$-distribution and exp(1) distribution (shown in grey), respectively, for $N = 20$ with fitted normal distributions. For the third jump point, the histograms of the two underlying link weight distributions possess a big overlap whereas for increasing jump points this overlap decreases and the mean for the exponentially distributed link weights becomes higher than the average jump point of the uniformly distributed link weights.

The link with i-th smallest link weight $w_{(i)}$ has weight $w_{(i)}^{\frac{1}{\alpha_2}}$ in G_{α_2}. We call the index i the rank of the link since the ordering of the weights of all the links is independent of $\alpha > 0$. This link in G_{α_1} will have the same rank i, but its weight is $w_{(i)}^{\frac{1}{\alpha_1}}$. Furthermore, the proof assumes that all original weights are different, so that strict inequality signs can be used (that simplify the proof). With overwhelming probability, all link weights generated from a realistic probability distribution function $F_w(x)$ are distinct.

Proof: The proof is by contradiction (reductio ad absurdum). Assume that there exist a link with rank k in G_{α_2} that belongs to U_{α_2}, but this link in G_{α_1} does not belong to U_{α_1}. The link with rank k connects the nodes A and B in both G_{α_1} and G_{α_2}. The fact that $k \notin U_{\alpha_1}$ means that there exists a path $\mathscr{P}_{AB}$ between nodes A and B, such that

$$w_{(k)}^{\frac{1}{\alpha_1}} > \sum_{i \in \mathscr{P}_{AB}; i<k} w_{(i)}^{\frac{1}{\alpha_1}} \tag{3.4}$$

where, importantly, the rank condition $i < k$ for a link implies that each link in $\mathscr{P}_{AB}$ must have a smaller weight than the link with rank k. Using $w_{(i)}^{\frac{1}{\alpha_1}} = w_{(i)}^{\frac{1}{\alpha_2}} w_{(i)}^{\frac{\alpha_2-\alpha_1}{\alpha_1\alpha_2}}$, we rewrite inequality (3.4) as

$$w_{(k)}^{\frac{1}{\alpha_1}} = w_{(k)}^{\frac{1}{\alpha_2}} w_{(k)}^{\frac{\alpha_2-\alpha_1}{\alpha_1\alpha_2}} > \sum_{i \in \mathscr{P}_{AB}; i<k} w_{(i)}^{\frac{1}{\alpha_2}} w_{(i)}^{\frac{\alpha_2-\alpha_1}{\alpha_1\alpha_2}}$$

Since $i < k$ and $\alpha_1 \geq \alpha_2$, it holds that $w_{(i)}^{\frac{\alpha_2-\alpha_1}{\alpha_1\alpha_2}} > w_{(k)}^{\frac{\alpha_2-\alpha_1}{\alpha_1\alpha_2}}$ and

$$\sum_{i \in \mathscr{P}_{AB}; i<k} w_{(i)}^{\frac{1}{\alpha_2}} w_{(i)}^{\frac{\alpha_2-\alpha_1}{\alpha_1\alpha_2}} > w_{(k)}^{\frac{\alpha_2-\alpha_1}{\alpha_1\alpha_2}} \sum_{i \in \mathscr{P}_{AB}; i<k} w_{(i)}^{\frac{1}{\alpha_2}}$$

from which we find the inequality

$$w_{(k)}^{\frac{\alpha_2-\alpha_1}{\alpha_1\alpha_2}} w_{(k)}^{\frac{1}{\alpha_2}} > w_{(k)}^{\frac{\alpha_2-\alpha_1}{\alpha_1\alpha_2}} \sum_{i \in \mathscr{P}_{AB}; i<k} w_{(i)}^{\frac{1}{\alpha_2}}$$

Hence,

$$w_{(k)}^{\frac{1}{\alpha_2}} > \sum_{i \in \mathscr{P}_{AB}; i<k} w_{(i)}^{\frac{1}{\alpha_2}}$$

which contradicts the hypothesis that the link with rank $k \in U_{\alpha_2}$. ☐

In other words, all links in U_{α_2} belong to U_{α_1} if $0 < \alpha_2 \leq \alpha_1$. Thus, the USPT Inclusion Theorem 1 provides another proof besides the one in [117] of the property that *the MST belongs to the USPT U_α for any $\alpha > 0$.*

For all $\alpha \in (0, \alpha_c)$-interval, the USPT U_α equals the MST with $L = N-1$ links. The next interval, $[\alpha_c, \alpha_c + \Delta\alpha)$ with $\xi_1 = \alpha_c$ and $\Delta\alpha = \xi_2 - \xi_1$, creates a USPT equal to the MST plus one link, and so on. By the USPT Inclusion Theorem 1, the set of subgraphs $U_{\xi_1} \subset U_{\xi_2} \subset \cdots \subset U_{\xi_{\binom{N-1}{2}}}$ are all connected and two subsequent subgraphs differ by one link, i.e.

$$U_{\xi_j} \setminus U_{\xi_{j-1}} = l_{(j)} \text{ for } 1 \leq j \leq \binom{N-1}{2}.$$

In other words, each jump ξ_j can be related to a particular link $l_{(j)}$, which is not contained in any USPT U_α with $\alpha < \xi_j$. In this way, links in any weighted graph can be ordered.

We compared the new link ordering based on the α-trees with the ranking of the links that emerges from the original link weights (for an example see Figure 3.6). For the links included in the MST, we assigned the same ordering for the USPT ranking as for the original link weight ordering. In Figure 3.7a, we plotted a histogram of the correlation values between the original link weight ordering and the USPT ranking for 100 networks with uniformly distributed link weights (average correlation of 0.775). This result shows that the USPT ordering is positively correlated with but not trivially connected to the original link weight ordering.

For the construction of the MST, we include the smallest link weights starting with the one corresponding to rank 1 and then adding the higher ranked link weights whenever they do not form a circle (following the Kruskal algorithm). For increasing values of α, we add links to the MST. Every added link cannot be smaller in rank than all the links along the alternative existing shortest path because this link would otherwise have been included in the MST already. This rank relation among the added link weights explains the positive correlation of the original ranking and the USPT ranking.

Since the link betweenness is also based on the shortest path structure of the underlying network, we compared the USPT link ordering to the ranking depending on the link betweenness. However, the link betweenness ranking is not necessarily leading to a unique order. In other words, there may exist different links with the same link betweenness. Figure 3.7b shows a histogram of the correlation values between the USPT ranking and the ranking of the links based on their link betweenness. We found a moderate positive correlation (but again no trivial connection) between the link ordering based on the link betweenness and the link ordering based on the α-tree sampling method (see Figure 3.7b). Here, we could only correlate all the links that had a non-zero betweenness, which equals the number of links in the USPT U_1 (since $\alpha = 1$ returns the original weights and the USPT then consists of all links with non-zero betweenness). Thus, on average only approximately 20% of the links had a non-zero betweenness and could be ranked (see also Appendix Figure 3.10). Our link ordering can rank all links in G, which can be regarded as an advantage over the link betweenness ranking. Concerning the connection between the USPT and the link betweenness, we also proved the following theorem.

Theorem 2 *Among all subgraphs of the weighted K_N with the same number of links, the USPT U_α has the highest overall link betweenness.*

Proof: Let us assume that the link weights have been transformed with $(1-w)^{1/\alpha}$ for a certain fixed value of $\alpha > 0$. We then construct the USPT U_α. The node betweenness in the underlying network or substrate is equal to the node betweenness in the USPT [122]. The link betweenness is defined as the number of shortest paths between all node pairs that traverse that link [122]. If a link is a subpart of a shortest path, it is included in the USPT. Hence, the construction of the USPT filters out all links with zero link betweenness. Therefore, the USPT includes all links with a non-zero betweenness.

The overall betweenness of a graph equals the sum of all link betweenness values. The overall betweenness of the USPT is then (for a certain fixed value of α) equal to the overall betweenness of the substrate, since all links with positive betweenness are included in the USPT. Any other subgraph with the same number of links as the USPT would include a zero-betweenness link and exclude therefore a link with a higher betweenness. Thus, the overall betweenness of any other subgraph with the same number of links as the USPT is lower than the betweenness of the USPT, which proves the theorem. ☐

In addition, the set of $k \geq N-1$ highest links, ordered by the link betweenness, does not necessarily generate a connected subgraph.

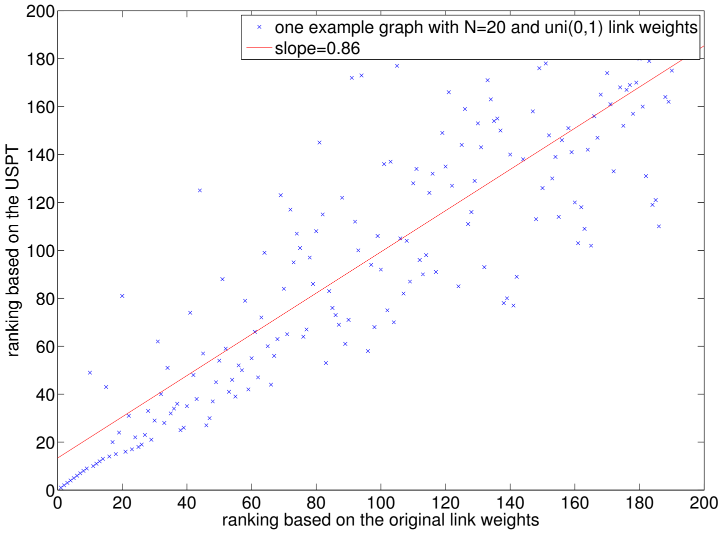

Figure 3.6: Scatterplot of different link orderings of an example network with $N = 20$, based on the original link weights against a link ordering based on our USPT method. Note that there seems to be a positive correlation between the two link orderings. Links included in the MST were given the ranking according to the original link ordering.

To sum up, the new link ordering based on the α-tree sampling method is positively correlated with the original and the link betweenness ranking but exploits the shortest path structure of the underlying network even more by proposing a method to rank all links with regard to their importance for the shortest paths (also the links with zero betweenness). For any value of the tuning parameter α, this sampling method results in a connected subgraph of the network always including all shortest paths with regard to different levels of importance.

3.4. APPLICATION TO FUNCTIONAL BRAIN NETWORKS

We applied the α-tree sampling method to functional brain networks from patients and healthy controls.

DATA ACQUISITION

The used data set included the functional brain networks of 68 healthy controls and 111 MS patients based on magnetoencephalography (MEG) measurements, which overlapped with the group data set analyzed in [98, 99]. For details of the data acquisition and processing, we refer to the previous study [99]. The data was subdivided into six frequency bands: *delta* (0.5 - 4 Hz), *theta* (4 - 8 Hz), *alpha1* (8 - 10 Hz), *alpha2* (10 - 13 Hz), *beta* (13 - 30 Hz), and lower *gamma* bands (30 - 48 Hz). As a link weight, the Phase Lag Index (PLI) was computed between all time series of the $N = 78$ brain regions for each of the frequency bands [91, 93].

CONSTRUCTION OF α-TREES FOR FUNCTIONAL BRAIN NETWORKS

In functional brain networks, the graph G equals the complete graph K_N on N nodes and a high value of w reflects a high correlation between the brain regions that are connected by the link. We transform each link weight w in K_N to be able to use the USPT method and obtain a new value for the link specified by

$$V = (1-w)^{\frac{1}{\alpha}} \tag{3.5}$$

where $\alpha > 0$ is the tuning parameter and the transform $\widetilde{V} = 1 - w$ is needed to map a high link weight onto a low link weight, where $\widetilde{V} \in [0,1]$ since $w \in [0,1]$.

In Figure 3.8, the mean link density of the USPT under the link weight transformation $(1-w)^{1/\alpha}$ is different for different frequency bands. The *gamma*-band shows the highest link density over the whole range of regarded α-values, and, on the other hand, the *alpha1*-frequency band produces the sparsest USPT over the whole range.

(a) Correlation between USPT and original link weight ranking.

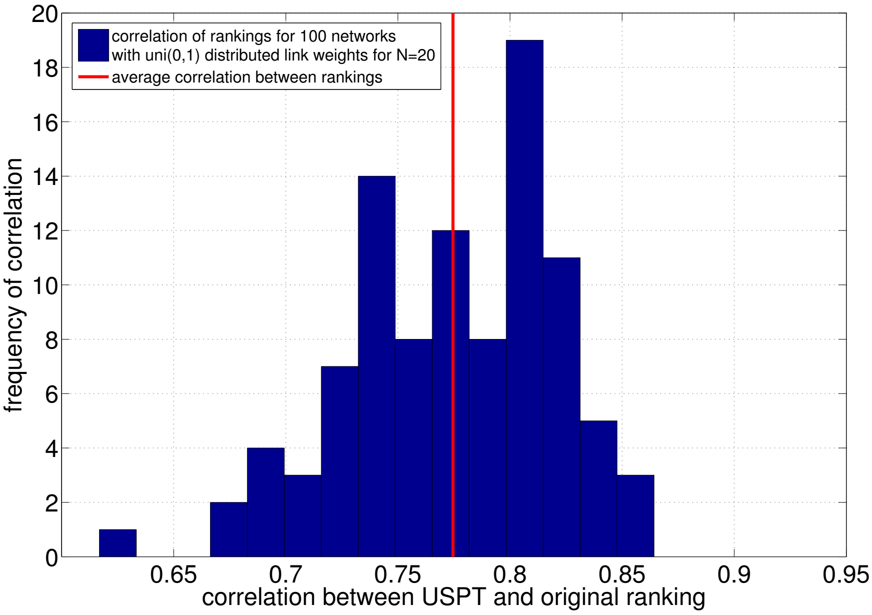

(b) Correlation between USPT and betweenness centrality ranking.

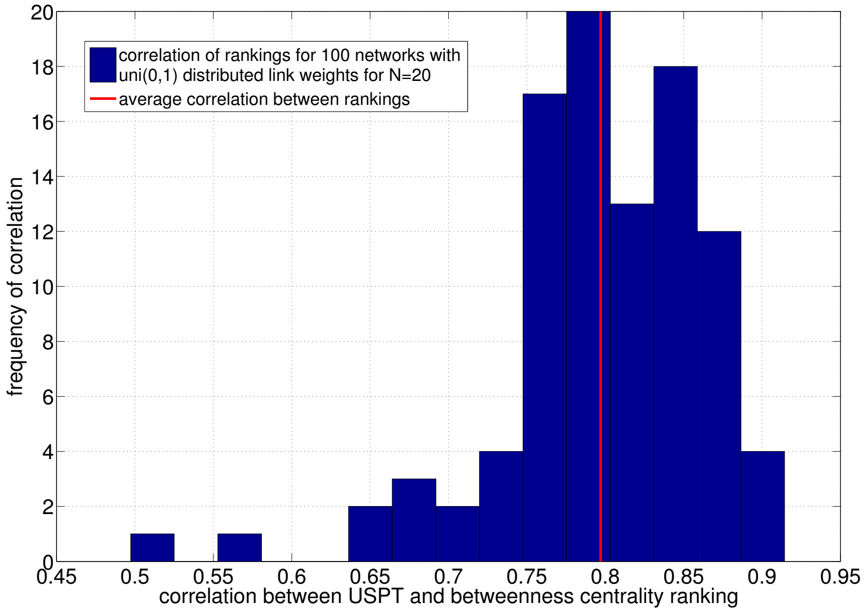

Figure 3.7: Histograms of correlation values between different rankings of the links from 100 uniform $(0,1)$-distributed networks with $N = 20$. (a) Correlation between USPT ranking and original ranking. (b) Correlation between USPT ranking and betweenness centrality ranking. There seems to be a positive correlation in both cases.

Table 3.1: p-values of the MWW-test for the distribution of link densities of MS patients against healthy controls. The p-values marked with * are significant under the 5% significance level.

frequency band	*alpha1*	*alpha2*	*delta*	*theta*	*beta*	*gamma*
p-values	.1957	.0857	.0375*	.0017*	.7772	.7003

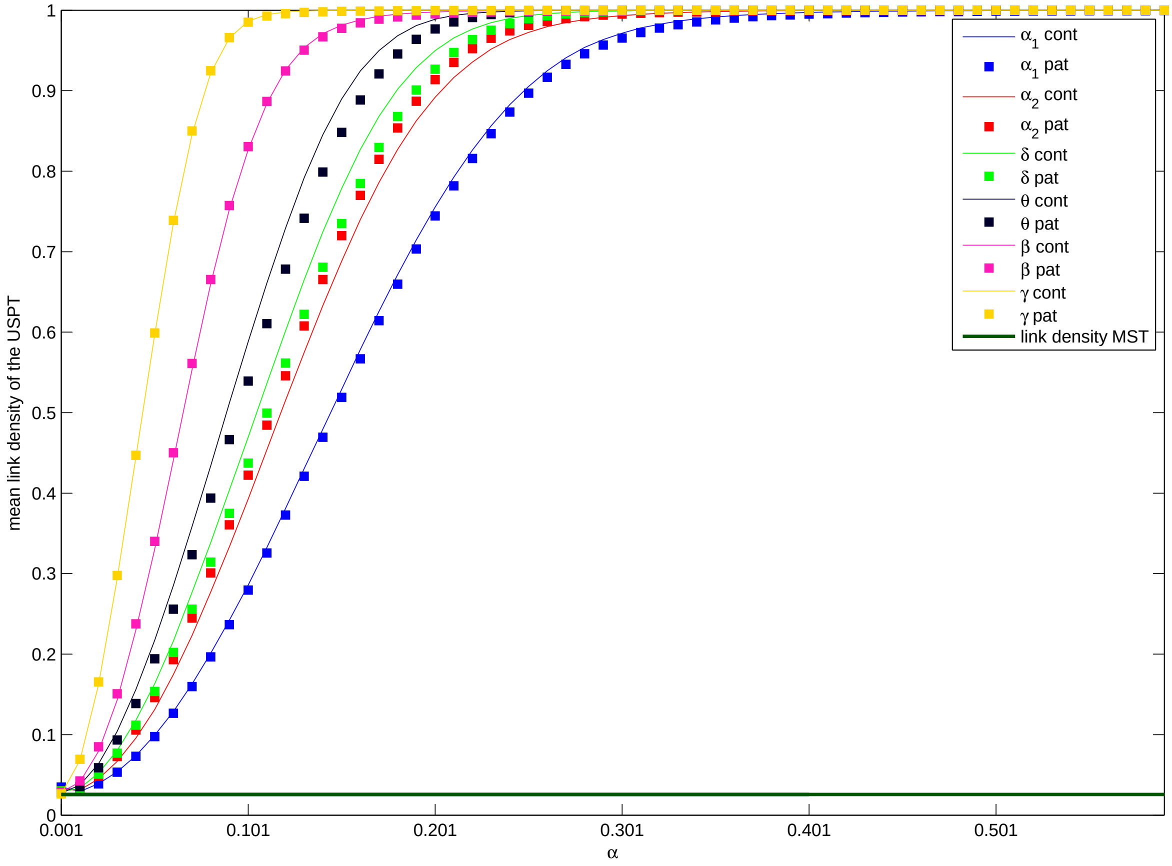

Figure 3.8: Mean link density of the USPT of healthy controls and MS patients over different frequency bands under the link weight transformation $(1-w)^{1/\alpha}$.

Concerning differences between patients and healthy controls in Figure 3.8, we find that the MS patients have a lower link density of their USPT in the delta and theta frequency band over the whole range of α-values and a slightly lower one also in the *alpha1* frequency band. In addition to that, patients show a higher link density of their USPT in the *alpha2* band. We tested those differences for their statistical significance and showed the p-values of the Mann-Whitney-Wilcoxon (MWW) test in Table 3.1. If we choose the significance level of 0.05, we find statistically significant differences between patients and healthy controls in the *delta* and *theta* frequency band.

With the sampling method of the α-trees, we found different numbers of links in the USPT over different frequency bands and also differences between MS patients and healthy controls over the whole range of α-values. Using α as a tuning parameter, we can adjust the link density of our network to a favored level. We can thereby reach any link density between 100% and $N-1$ links, always guaranteeing to include the MST and therefore to obtain a connected subgraph. With this approach, we succeeded in filtering out the low original link weights (corresponding to low PLI values) which is often the objective for functional brain networks. The USPT includes then per construction all high original link weights (high PLI values) up to a certain level as direct shortest paths.

The found significant differences between MS patients and healthy controls are in line with previous studies. A different, more classic analysis on nearly the same data set [99] found that for MS patients, there has been a higher mean PLI value in the *delta* and *theta* frequency band and a lower mean PLI value in the *alpha2* frequency band. The higher mean PLI value in the *delta* and *theta* band seems to align with our findings of a lower link density for the USPT for patients under the transformation $(1-w)^{1/\alpha}$. On the same data set, a probabilistic approach for the USPT was also studied 2. Here, significant differences were also found in the same frequency bands but the link density of the USPTs was above 99%. Therefore, the USPT under the probabilistic link weight transformation had a very dense representation and was not tunable with any parameter. Thus, the α-tree method can be seen as a complementary approach to the classic MST analysis and the probabilistic USPT representation because the tuning parameter α allows us to reach any favorable link density.

3.5. CONCLUSION

In this study, we proposed a new general sampling method of α-trees which reveals the shortest path structure of any underlying network under different levels of importance. We showed the influence of the underlying link weight distribution on the development of the link density for increasing values of the tuning parameter α. The critical α, which represents the phase transition between strong and weak disorder regime, and other initial jump points seem to be independent of the underlying link weight distribution. However, for higher link densities of the α-trees the underlying link weight distribution seems to obtain more influence. We showed that the new sampling method of α-trees gives rise to a new link ordering which facilitates to rank the link importance with regard to the shortest path structure for all links in the network. This new USPT link ordering is related to the link betweenness and can rank all links with respect to their importance for the shortest path structure (also those with zero betweenness). Furthermore, the α-tree sampling method was able to detect significant differences between MS patients and healthy controls. Those differences were found in the same frequency bands as in previous studies on a similar data set [99] (and in Chapter 2). Therefore, we propose the α-trees a new sampling method for extracting differences between the functional brain networks of patients and healthy controls. Future work should explore more data sets of functional brain networks from patients suffering from other brain disorders. Moreover, this new method can be applied in many different areas of complex networks ranging from transportation networks to electrical networks where especially the new link ordering can be useful to find bottlenecks concerning the robustness of these networks.

3.6. APPENDIX

3.6.1. SPACINGS

The spacing $\Delta\alpha_j = \xi_j - \xi_{j-1}$ for $j > 1$ seems to be an interesting feature of U_α (see Figures 3.9a and 3.9b). The distribution of those spacings $\Delta\alpha_j$ seems to be a power-law distribution with exponents between 2 and 3 (see Figures 3.9a and 3.9b). Furthermore, we face only small differences between the exponential and the uniform distribution. Therefore, the initial link weight distribution seems to have only limited influence on those spacings.

3.6.2. ADDITIONAL PROPERTIES OF THE USPT

TRANSFORMATIONS $h(x,\alpha)$ THAT POSSESS THE USPT INCLUSION PROPERTY

Here, we aim to identify a class of link weight transformation functions $h(x,\alpha)$ that possess the generalized USPT inclusion property. Specifically, we construct the USPT U_α on the weighted network $G(\alpha)$ where the weight of each link is a function $h(x,\alpha)$ of the weight in the original network. The objective is to discover the transform functions $h(x,\alpha)$ such that the generalized inclusion property follows, i.e. for any pair $\alpha_1 \geq \alpha_2, U_{\alpha_2} \subseteq U_{\alpha_1}$ always holds or $U_{\alpha_1} \subseteq U_{\alpha_2}$ always holds.

Theorem 3 (Transformation Functions) *If a transform function $h(x,\alpha)$ meets the following conditions: (a) $h(x,\alpha)$ is monotonously increasing or decreasing with x; (b) $h(x,\alpha)$ is monotously increasing or decreasing with α; and (c)*

$$\begin{cases} \dfrac{\partial\left(\frac{\partial \log h(x,\alpha)}{\partial\alpha}\right)}{\partial x} < 0 & \textit{if}\ \dfrac{\partial h(x,\alpha)}{\partial x} > 0 \\ \dfrac{\partial\left(\frac{\partial \log h(x,\alpha)}{\partial\alpha}\right)}{\partial x} > 0 & \textit{if}\ \dfrac{\partial h(x,\alpha)}{\partial x} < 0 \end{cases}$$

then the inclusion property $U_{\alpha_2} \subseteq U_{\alpha_1}$ holds for $\alpha_1 > \alpha_2$.

Proof: The condition (a) insures that the ordering of the link weights in $G(\alpha)$ is the same for any α. Thus, if the link weight $h(x_i,\alpha_1)$ is the i-th smallest weight in $G(\alpha_1)$, the corresponding weight $h(x_i,\alpha_2)$ in $G(\alpha_2)$ is as well the i-th smallest. For simplicity, the index i means that $h(x_i,\alpha)$ is the i-th smallest weight in $G(\alpha)$.

For any link weight x and a positive, small constant $\Delta > 0$, we have

$$h(x,\alpha+\Delta) = h(x,\alpha) + \Delta\frac{\partial h(x,\alpha)}{\partial\alpha} + O\left(\Delta^2\right)$$

Hence,

$$\frac{h(x,\alpha+\Delta)}{h(x,\alpha)} = 1 + \frac{\Delta}{h(x,\alpha)}\frac{\partial h(x,\alpha)}{\partial\alpha} + O\left(\Delta^2\right)$$

and

$$\frac{\partial\left(\frac{h(x,\alpha+\Delta)}{h(x,\alpha)}\right)}{\partial x} = \Delta\frac{\partial\left(\frac{\partial \log h(x,\alpha)}{\partial\alpha}\right)}{\partial x} + O\left(\Delta^2\right) \tag{3.6}$$

Furthermore, for sufficiently small $\Delta > 0$, the sign of the left- and right-hand side partial derivatives are equal.

For any index $i < j$, we have that $h(x_i,\alpha) < h(x_j,\alpha)$, since the index i of the link denotes the rank of the weight $h(x_i,\alpha)$ in $G(\alpha)$. If $\frac{\partial h(x,\alpha)}{\partial x} > 0$, then $x_i < x_j$, i.e. x_i is also the i-th smallest weight in the original network. In this case, equation (3.6) arrives at $\frac{\partial\left(\frac{h(x,\alpha+\Delta)}{h(x,\alpha)}\right)}{\partial x} < 0$, according to condition (c) and it implies that

$$\frac{h(x_j,\alpha_1)}{h(x_j,\alpha_2)} < \frac{h(x_i,\alpha_1)}{h(x_i,\alpha_2)} \tag{3.7}$$

If $\frac{\partial h(x,\alpha)}{\partial x} < 0$, then $x_i > x_j$ in the original network. Equation (3.6) becomes $\frac{\partial\left(\frac{h(x,\alpha+\Delta)}{h(x,\alpha)}\right)}{\partial x} > 0$ according to condition (c) and it implies the inequality (3.7) as well.

Assume that there exists a link with rank k in $G(\alpha_1)$ that does not belong to U_{α_1}. This means that there exists a path $\mathscr{P}_{AB}$ between nodes A and B, such that

$$h(x_k,\alpha_1) > \sum_{i\in\mathscr{P}_{AB};i<k} h(x_i,\alpha_1) = \sum_{i\in\mathscr{P}_{AB};i<k} h(x_i,\alpha_2)\frac{h(x_i,\alpha_1)}{h(x_i,\alpha_2)}$$

(a) Spacings of exponentially distributed link weights.

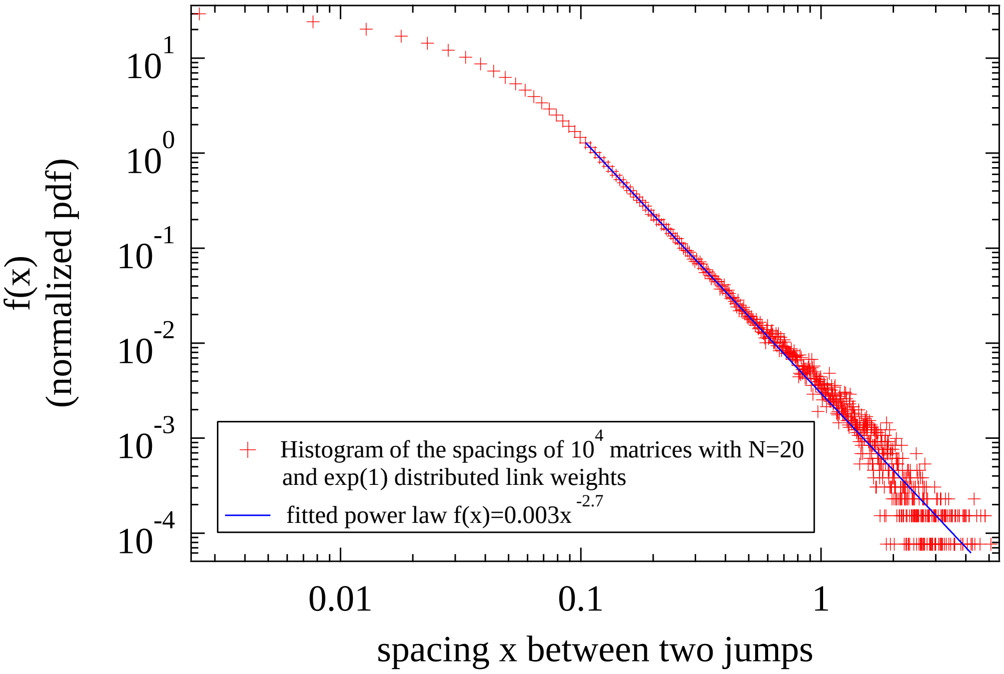

(b) Spacings of uniformly distributed link weights.

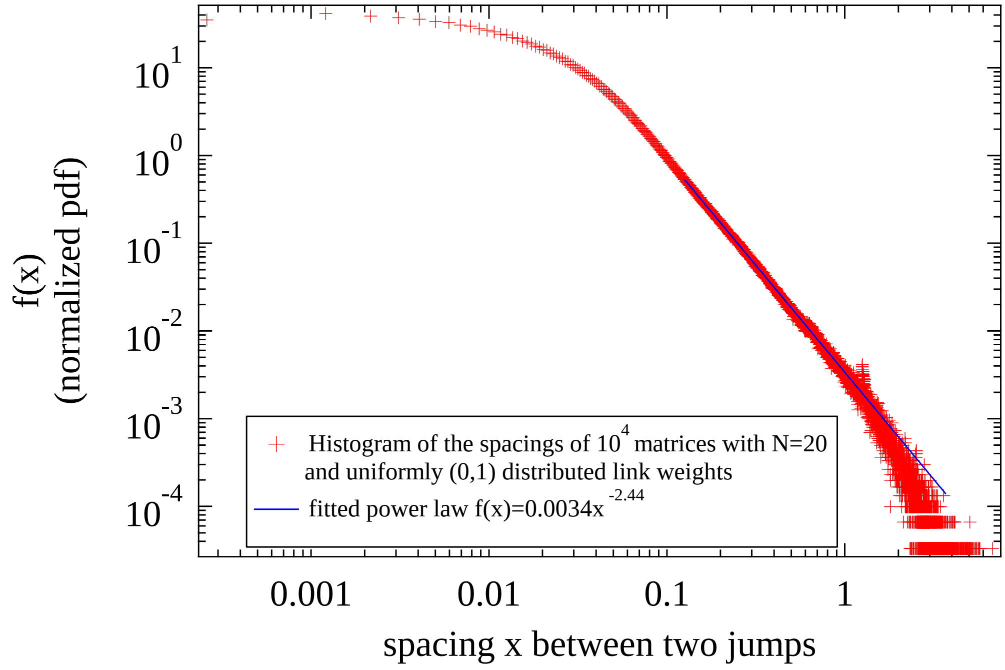

Figure 3.9: Histograms of the spacings (in log-log plots) each based on 10^4 generated matrices under the link weight transformation $w_{ij}^{(1/\alpha)}$ for all i, j for $N = 20$ with a fitted power law in (a) from the exp(1) distribution and in (b) from the uniform $(0,1)$-distribution.

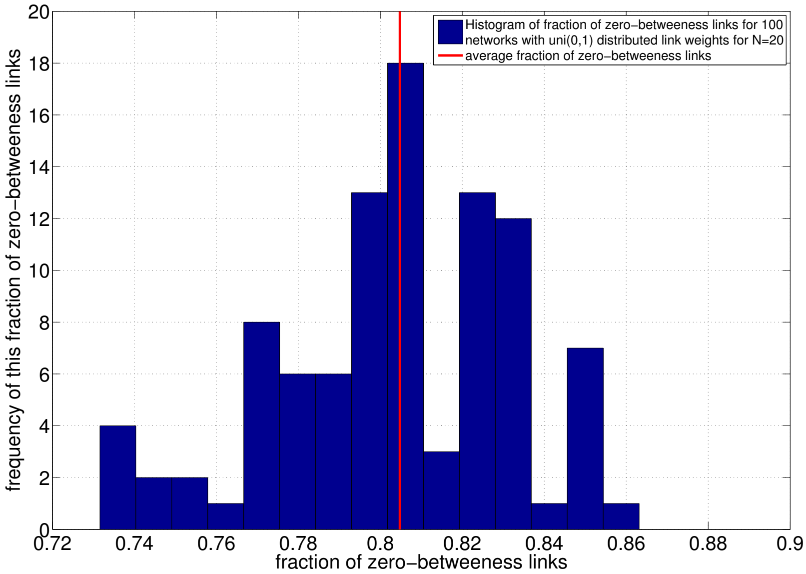

Figure 3.10: Frequency of zero-betweenness links for 100 networks with uniformly distributed link weights from the interval $(0,1)$.

Using the basic inequality (3.7) for h,

$$\sum_{i\in\mathscr{P}_{AB};i<k} h(x_i,\alpha_2)\frac{h(x_i,\alpha_1)}{h(x_i,\alpha_2)} > \frac{h(x_k,\alpha_1)}{h(x_k,\alpha_2)}\sum_{i\in\mathscr{P}_{AB};i<k} h(x_i,\alpha_2)$$

leads to

$$h(x_k,\alpha_2) > \sum_{i\in\mathscr{P}_{AB};i<k} h(x_i,\alpha_2)$$

which means that a link with rank k does not belong to U_{α_2} and, consequently, $U_{\alpha_2}\subseteq U_{\alpha_1}$. ☐

The transformation functions specified in Theorem 3 are possibly not the only functions that possess the inclusion property.

DETERMINATION OF JUMP POINTS

Suppose that the link with rank k between node A and B is just included in U_{α_1}, but not in U_{α_2} for $\alpha_2<\alpha_1<1$. Then, from (3.4), the following equations hold

$$\begin{cases} w_{(k)}^{\frac{1}{\alpha_1}} \le \sum_{i\in\mathscr{P}_{AB}(\alpha_1);i<k} w_{(i)}^{\frac{1}{\alpha_1}} & \text{for any path } \mathscr{P}_{AB}(\alpha_1) \text{ in } G_{\alpha_1} \\ w_{(k)}^{\frac{1}{\alpha_2}} > \sum_{i\in\mathscr{P}^*_{AB}(\alpha_2);i<k} w_{(i)}^{\frac{1}{\alpha_2}} & \mathscr{P}^*_{AB}(\alpha_2) \text{ is the shortest path in } G_{\alpha_2} \end{cases}$$

and the link with rank k between node A and B is $\mathscr{P}^*_{AB}(\alpha_1)$. We apply Hölder's inequality for $p>1$ (see e.g. [113, p. 107])

$$\frac{1}{n}\sum_{j=1}^{n}|x_j| \le \left(\frac{1}{n}\sum_{j=1}^{n}|x_j|^p\right)^{\frac{1}{p}}$$

to the shortest path $\mathscr{P}^*_{AB}$ with hopcount $h\left(\mathscr{P}^*_{AB}\right)$ (i.e. the number of links in the path $\mathscr{P}^*_{AB}$) and obtain, for any $p=\frac{1}{\alpha_2}>1$,

$$\frac{1}{h\left(\mathscr{P}^*_{AB}(\alpha_2)\right)}\sum_{i\in\mathscr{P}^*_{AB}(\alpha_2);i<k} w_{(i)}^{\frac{1}{\alpha_2}} \ge \left(\frac{1}{h\left(\mathscr{P}^*_{AB}(\alpha_2)\right)}\sum_{i\in\mathscr{P}^*_{AB}(\alpha_2);i<k} w_{(i)}\right)^{\frac{1}{\alpha_2}}$$

so that

$$w_{(k)} > \left\{h\left(\mathscr{P}^*_{AB}(\alpha_2)\right)\right\}^{\alpha_2-1}\sum_{i\in\mathscr{P}^*_{AB}(\alpha_2);i<k} w_{(i)}$$

If $h\left(\mathscr{P}^*_{AB}\right) = 1$, then the inequality is always true by the ordering assumption $w_{(k)} > w_{(k-1)}$ for any link with rank k. However, the shortest path between A and B consists of one link and that link must be, by construction, the link with rank k. Hence, we conclude that $h\left(\mathscr{P}^*_{AB}(\alpha_2)\right) \geq 2$. Solving the inequality for α_2 yields

$$\alpha_2 < 1 - \frac{\log \sum_{i \in \mathscr{P}^*_{AB}(\alpha_2); i<k} \frac{w_{(i)}}{w_{(k)}}}{\log h\left(\mathscr{P}^*_{AB}(\alpha_2)\right)}$$

where $\sum_{i \in \mathscr{P}_{AB}; i<k} \frac{w_{(i)}}{w_{(k)}} \leq h\left(\mathscr{P}_{AB}\right)$, with equality only if all order statistics, hence the link weights, are the same. If $\sum_{i \in \mathscr{P}^*_{AB}(\alpha_2); i<k} \frac{w_{(i)}}{w_{(k)}} < 1$, then $\alpha_2 > 1$, in which case the Hölder's inequality cannot be applied. Hence, the inequality $\alpha_2 < 1$ implies that $\sum_{i \in \mathscr{P}^*_{AB}(\alpha_2); i<k} w_{(i)} > w_{(k)}$. In summary, we find that a link with rank k between A and B that does not belong to U_{α_2} for $\alpha_2 < 1$ obeys

$$\sum_{i \in \mathscr{P}^*_{AB}(\alpha_2); i<k} w_{(i)} > w_{(k)} > \left(\sum_{i \in \mathscr{P}^*_{AB}(\alpha_2); i<k} w_{(i)}^{\frac{1}{\alpha_2}} \right)^{\alpha_2} \tag{3.8}$$

where $h\left(\mathscr{P}^*_{AB}(\alpha_2)\right) \geq 2$. When α increases from α_2 towards α_1, the link with rank k becomes the shortest path between A and B. Furthermore, when $U_{\alpha_1} = U_{\alpha_2} \cup \{\text{the link with rank } k\}$, then $\mathscr{P}^*_{AB}(\alpha_2)$ remains the shortest path for $\alpha \in [\alpha_2, \alpha_1)$ and α_1 is a jump point, or the smallest value of α for which inequality (3.8) does not hold anymore.

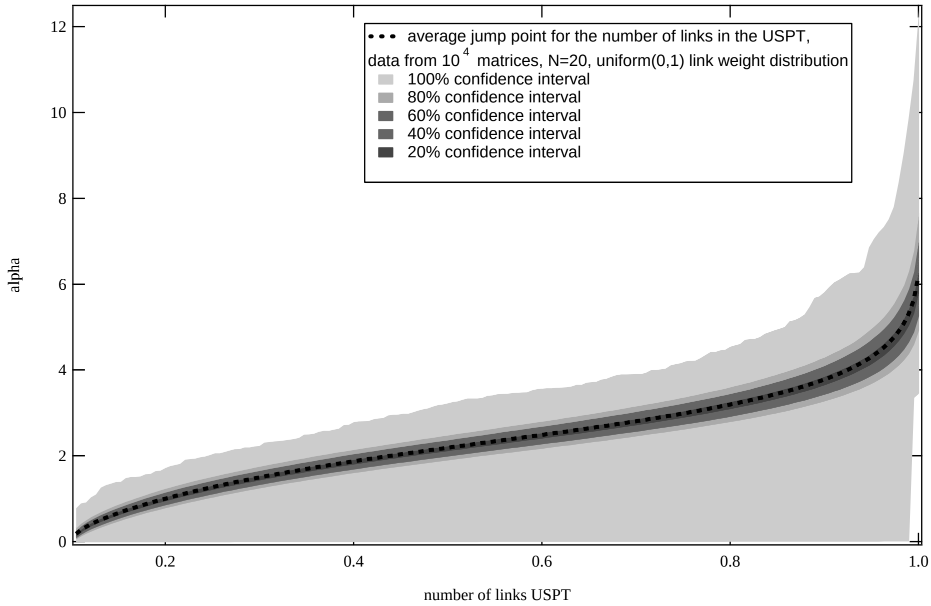

Figure 3.11: The contour plot over 10^4 realizations of network with $N = 20$ nodes and the underlying uniform link weight distribution with values between (0,1) connects α to the number of links in U_α. The average jump point for the link density is visualized as a dotted black line and the different shades of grey symbolize the different confidence intervals for this jump point. 100% confidence intervals means the space between the minimum and maximum jump point, 80% confidence interval then colors the space between the 10th and the 90th percentile, etc..

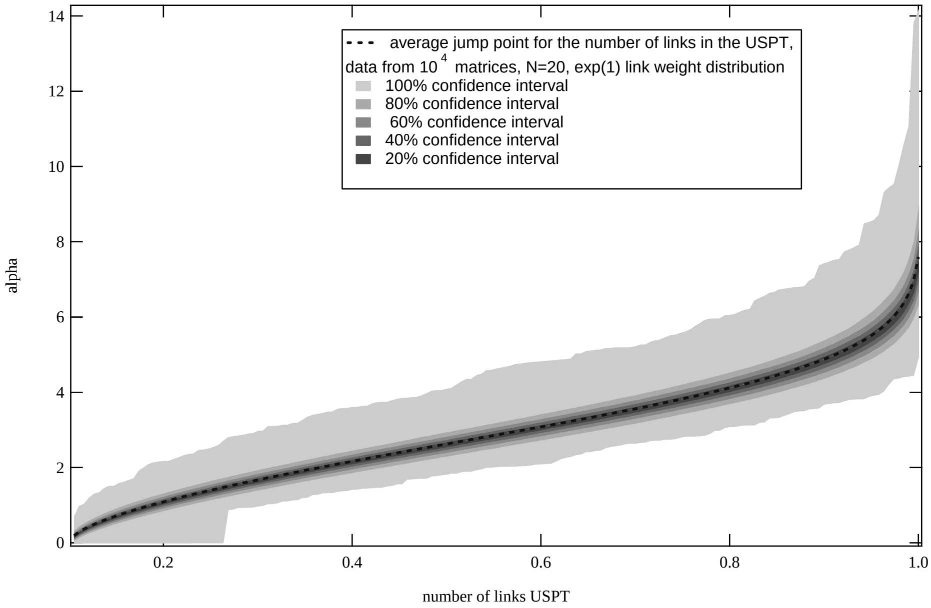

Figure 3.12: The contour plot over 10^4 realizations of network with $N = 20$ nodes and the underlying exponential link weight distribution with mean 1 connects α to the number of links in U_α. The average jump point for the link density is visualized as a dotted black line and the different shades of grey symbolize the different confidence intervals for this jump point. 100% confidence intervals means the space between the minimum and maximum jump point, 80% confidence interval then colors the space between the 10th and the 90th percentile, etc..

4

MOTIFS IN FUNCTIONAL BRAIN NETWORKS

4.1. INTRODUCTION

Recent studies in neuroscience applied the measure of Phase Transfer Entropy (PTE) to construct the effective connectivity network between brain regions and observed a global posterior-anterior pattern in higher frequency bands [50]. However, the effective connectivity at a local level remains yet to be analyzed. In this chapter, we analyze with PTE the directionality at a local level in the form of network motifs.

Effective connectivity describes the causal effect of one brain region on another region [2, 35]. To calculate this pairwise value between brain regions, the measure of Transfer Entropy (TE) is often applied [82]. The TE from a region X to a region Y quantifies the improvement in predicting the future of time series X if the present value of Y is also included. Recent work has extended this measure to the analysis of phase time series (Phase Transfer Entropy (PTE); [61]). The advantage of phase time series instead of the original time series is the lower computational cost for analyzing their pairwise interactions [79]. When representing brain regions as nodes and assigning PTE values as link weights, one can build the effective connectivity network.

Based the pairwise PTE values, Hillebrand et al. [50] observed that for higher frequency bands, *alpha1*, *alpha2* and *beta*, the global information flow was predominantly from posterior to anterior brain regions, whereas the pattern was opposite for the *theta* band. The latter, an anterior-to-posterior pattern, was also discovered in electroencephalography (EEG) data [20]. The emergence of this pattern is still not completely understood. The different patterns of information flow in resting-state networks are likely driven by the strong posterior hubs and their high neuronal activity [21, 50, 70]. Furthermore, activity in the *alpha* and *theta* frequency band has both been related to attention encoding probably its different spatiotemporal contents [33]. Another biological explanation for the reverse patterns could be the two interacting subsystems of the Default Mode Network (network of brain regions active during resting-state): The temporal and the fronto-parietal system, which are responsible for memory and self-relevant mental simulations, respectively [13], seem to exist in parallel on different frequencies representing together an integration mechanism for brain function [29]. This hypothesis is strengthened by results from invasive animal recordings of the visual cortex [4, 109], where the opposite directions of information flow have been connected with the process of memory consolidation [84].

On a local scale, network motifs are the building blocks of all networks [68]. On top of the micro-structure of nodes and links, network motifs are small subgraphs that form a higher-order organization of the network [7]. Most commonly, network motifs of 3 or 4 nodes are analyzed. Friedman et al. [34] were recently able to identify Alzheimer patients with directed motif analysis in a so-called progression network. Previous work reported that the motif with ID 78 was overexpressed with respect to random networks in the structural brain networks of the cat and the macaque [88] (see Fig. 4.2 for motif IDs). The same motif has also been perceived as a good identifier for structural hubs [52]. Recently, Battiston et al. analyzed the interdependency between structure and function in the human brain applying a multilayer motif approach [6]. With computational models of neuronal activity, Battaglia and co-authors [5] linked effective connectivity motifs based on TE to underlying structural motifs and suggested that changes in the effective connectivity lead to different global directions of information flow. With similar motivation of linking frequencies of single motifs to global outcomes, Benson et al. [7] exploited this higher-order organization of the network to define a new motif-based clustering algorithm.

The aim of this chapter is to investigate effective connectivity motifs in empirical data with the measure of PTE. The subchapter 4.2 describes the analysis of information flow motifs based on the measure of directed Phase Transfer Entropy (dPTE) and focuses on data from the *alpha2* frequency band. An extended investigation of both the *alpha2* and the *theta* frequency band data is conducted in the following subchapter 4.3 starting directly from the measure of PTE.

4.2. MOTIF-BASED ANALYSIS OF EFFECTIVE CONNECTIVITY IN BRAIN NETWORKS

We first explain the construction of the effective connectivity network based on the sending and receiving properties of a node. Then, we analyze the significant motifs in this network. Furthermore, we apply the recently developed motif-based clustering algorithm by Benson et al. [7] on the effective connectivity brain network.

4.2.1. METHODS

This section explains the measure of directed Phase Transfer Entropy (dPTE), the construction of the directed networks, the motif search and our application of the motif-based clustering.

DIRECTED PHASE TRANSFER ENTROPY

The effective connectivity network is based on MEG measurements[1] of 67 healthy controls from a preceding study [50]. We focus our analysis on the *alpha2* frequency band (10-13 Hz) because the previous study observed a significant pattern of posterior-anterior information flow for this frequency band. For every region of interest (ROI) X we compute a time series in the form of a phase time series [79]. We denote a possible value of the signal of region X at time t by x_t and abbreviate the probability that the signal of X equals x_t at an arbitrary time point t to $\Pr[X_t = x_t] = \Pr[x_t]$. The information flow between two ROIs or nodes, X and Y, is then quantified by the Phase Transfer Entropy [61]

$$PTE_{XY}(h) = \sum \quad \Pr\left[x_{t+h}, x_t, y_t\right] \quad \times \log\left(\frac{\Pr\left[x_{t+h}|x_t, y_t\right]}{\Pr\left[x_{t+h}|x_t\right]}\right), \tag{4.1}$$

for a certain time delay h, where the sum runs over all possible values x_t, x_{t+h} and y_t of the signals. The (joint) probabilities are determined over histograms of their occurrences in an epoch [61]. Following Hillebrand et al. [50] we fix h at

$$h = \frac{N_s \cdot N_{ROI}}{N_{\pm}}, \tag{4.2}$$

where $N_s = 4096$ and $N_{ROI} = 78$ are the number of samples and the number of ROIs, respectively, and $N_{\pm}$ counts the number of sign changes for the phase across time and ROIs.

Motivated by Hillebrand et al. [50], we define the dPTE for nodes X and Y as

$$dPTE_{XY} = \frac{PTE_{XY}}{PTE_{XY} + PTE_{YX}}, \tag{4.3}$$

which is a measure of the preferred direction of information flow between nodes X and Y. Since the PTE can only take positive values, this definition of dPTE is well-defined and its value ranges from 0 and 1. If the predominant flow of information is from node X to node Y, then $0.5 < dPTE_{XY} < 1$, else $0 < dPTE_{XY} < 0.5$.

CONSTRUCTING THE DIRECTED NETWORK

The pairwise dPTEs over all ROIs can be interpreted as a weight matrix of a fully connected network. Since the data is from 67 subjects each over $k = 20$ epochs, we have 1340 weighted networks to begin our construction. We apply a procedure to thin out links and induce a directionality per link instead of a weight. After this

---

This chapter has been published in J. Meier, M. Märtens, A. Hillebrand, P. Tewarie and P. Van Mieghem, *Motif-Based Analysis of Effective Connectivity in Brain Networks*, in *Fifth International Workshop on Complex Networks and their Applications* (Springer), November 30 - December 2, Milan, Italy. pp. 685 - 696 (2016).

[1] The MEG data were recorded using a 306-channel whole-head MEG system (ElektaNeuromag, Oy, Helsinki, Finland) during a no-task, eyes-closed condition for five consecutive minutes. A beamformer approach was adopted to project MEG data from sensor space to source space [49] and the automated anatomical labelling (AAL) atlas was applied to obtain time series for 78 cortical regions of interest (ROIs) [40, 104]. For each subject, we extracted the first 20 artefact-free epochs of 4096 samples (3.2768 s).

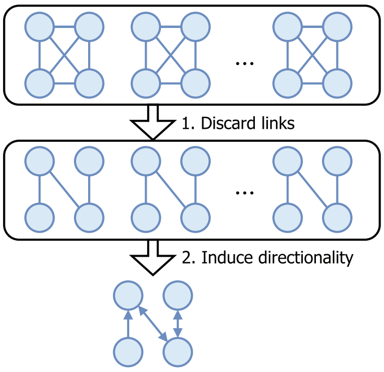

Figure 4.1: Schematic overview of the two steps for constructing the directed network (sparsification): (1) discard links close to 0.5 (2) induce directionality for remaining links.

transformation, which we call "sparsificiation", we obtain a sparse directed (unweighted) network for each subject, which is amenable for motif search and analysis.

The sparsification (see Fig. 4.1) contains two steps. First, we discard all links whose weights are in close proximity to 0.5. More precisely, every link whose average weight (over all epochs) is within the closed interval $[0.5-\alpha\sigma, 0.5+\alpha\sigma]$ will not be considered, where σ is the standard sample deviation taken over all epochs over all pairs of nodes and α is a positive real control parameter. Under the assumption of a normal distribution with mean 0.5, the 3σ-rule states that this procedure will remove approximately 68% for $\alpha = 1.0$ and 95% for $\alpha = 2.0$ of all links.

In a second step, we determine for each remaining link whether it should be bi- or uni-directional, and in case of the latter, in which direction the links should be oriented. Clearly, all remaining link weights are now bounded away from 0.5, though it is possible, that for different epochs a single link weight might be lower or higher than 0.5, which makes it ambiguous which member of the node pair is the dominant sender and which the dominant receiver. Let k^+ (k^-) be the number of epochs that the $dPTE_{XY}$ is above (below) 0.5 where $k = k^+ + k^-$ is the total number of epochs for a subject. If $k^+/k \geq 0.75$, we assume X to be a dominant sender and thus we induce a uni-directional link from X to Y. Contrary, we assume X to be a dominant receiver if $k^+/k \leq 0.25$ and point the link from Y to X. If neither applies ($0.25 < k^+/k < 0.75$), we assume that X and Y frequently change roles between dominant sender and dominant receiver. Thus, we induce a bidirectional link between them.

MOTIF SEARCH

We are using the excellent *mfinder* software [54], provided by the Uri Alon Lab[2], to search for motifs. We also adopted the motif IDs of mfinder for this work, to be consistent. With sparsification, we generate one directed network for each of the 67 subjects as input for mfinder. Additionally, we construct an averaged effective connectivity network (short: averaged network) by considering all epochs of all subjects together. This construction results in a "virtual" subject with $k = 1340$ instead of $k = 20$ epochs. We set α to 1.0 and 2.0 to compare on different levels of sparsity.

Since the complexity of motif search increases dramatically with the size of the motif, we restrict mfinder to search only for subgraphs of 3 and 4 nodes (further called 3-motifs and 4-motifs). The mfinder program executes two tasks: first, it counts the frequency of all motifs in the original input network. Second, it generates a number of random networks (null model) and determines the motif frequencies in each of them as well. In total, mfinder generates 1000 random networks using the switching algorithm described by Milo et al. [67] for each single input network. We use the default parameters for mfinder, which preserve the degree sequence of the original network and the number of bidirectional links.

A motif is called overexpressed if it occurs significantly more often in the original network than in the random networks. It is essential to keep in mind that a motif which is not overexpressed may still occur quite frequently in the original network, though it arises in a similar frequency by a random link rewiring process. Thus, it can be argued that overexpressed motifs must carry some functional importance for the underlying system since they do not arise merely by chance. We report the motifs that mfinder determines to be overexpressed with z-score > 2.

---

[2] `https://www.weizmann.ac.il/mcb/UriAlon/download/network-motif-software`

(a) Histogram of all significantly overexpressed 3-motifs.

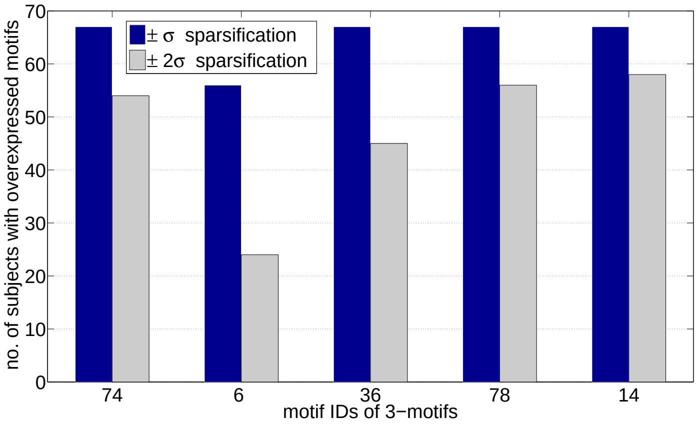

(b) **74** (c) **36** (d) **78** (e) **14** (f) **6**

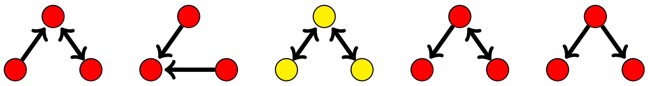

Figure 4.2: **(a)** Frequency of significantly overexpressed 3-motifs over all regarded subjects after the $\pm\sigma$ and $\pm 2\sigma$ sparsification, respectively. **(b)-(f)** All significant 3-motifs over all subjects together with their motif ID. The yellow motif with ID 78 is also overexpressed in the averaged network.

MOTIF-BASED CLUSTERING ALGORITHM

Benson et al. [7] developed a clustering algorithm that partitions a network based on one specific overexpressed motif M. The algorithm constructs clusters by 'cutting' through the minimal possible number of those motifs. Formally, the clustering minimizes the motif conductance defined as

$$\phi_M(S) = \frac{\mathrm{cut}_M(S, S^c)}{\min[\mathrm{vol}_M(S), \mathrm{vol}_M(S^c)]}, \tag{4.4}$$

where S is the set of nodes in the cluster and S^c its complement. Here, $\mathrm{cut}_M(S, S^c)$ is the number of M motifs that is cut through and $\mathrm{vol}_M(S)$ the number of M motifs that is completely in S. The algorithm can be regarded as an extension of the classic spectral clustering algorithm [111]. The obtained clusters reveal a higher-order organization of the network based on the specific motif M. An implementation of the motif-based clustering algorithm was released as part of the open SNAP framework [56], which we applied to the averaged network using default parameters.

4.2.2. RESULTS

We present results for the motif search on 3 and 4 nodes for the individual subjects and for the averaged network, respectively. In addition, we show the results of the motif-based clustering algorithm on the averaged network.

SIGNIFICANT 3-MOTIFS

For both variants of the sparsification method ($\alpha = 1$ and $\alpha = 2$), we find the same significant 3-motifs over all subjects meaning that those motifs are more frequent in our analyzed networks than in the null model (see Fig. 4.2). Those five motifs are not triangular but include all 3-motifs with two links (except for the 2-hop path motif) (Fig. 4.2b- 4.2f). The absolute frequency of those motifs is displayed as a histogram in Fig. 4.2a for the $\pm\sigma$ and the $\pm 2\sigma$ sparsification, respectively. The analysis on the averaged effective connectivity network confirms the over-representation of the motif with ID 78, the bidirectional 2-hop path(Fig. 4.2d), which is the only significant motif that has been found for different sparsification methods (z-scores: 88.25 for $\pm\sigma$ sparsification and 82.7 for $\pm 2\sigma$ sparsification).

(a) Histogram of the 20 most commonly overexpressed 4-motifs.

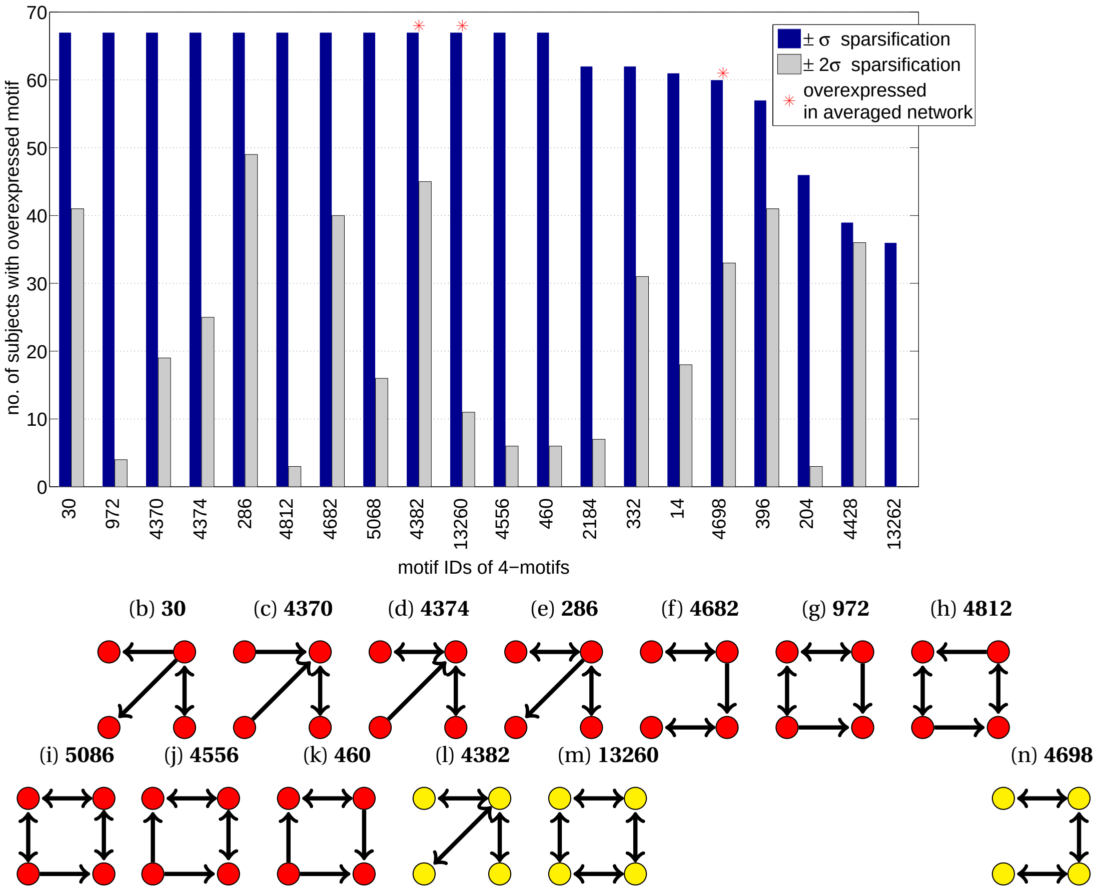

(b) **30** (c) **4370** (d) **4374** (e) **286** (f) **4682** (g) **972** (h) **4812**

(i) **5086** (j) **4556** (k) **460** (l) **4382** (m) **13260** (n) **4698**

Figure 4.3: **(a)** Histogram of the 20 most commonly overexpressed 4-motifs over all subjects after the $\pm\sigma$ and $\pm 2\sigma$ sparsification, respectively. An asterisk marks the motifs that are also overexpressed in the averaged network. **(b)**-**(m)** The twelve 4-motifs that are overexpressed after the $\pm\sigma$ sparsification in every subject with their motif ID. The yellow motifs are also overexpressed in the averaged network. **(n)** Third overexpressed 4-motif in the averaged network, ID 4698.

SIGNIFICANT 4-MOTIFS

In Fig. 4.3a we present a histogram of all significantly overexpressed 4-motifs with the two different sparsification levels. Twelve 4-motifs were found overexpressed in all 67 subject networks (Fig. 4.3a, for a visualization see Figs. 4.3b-4.3m).

Analyzing the averaged network we find 3 significant motifs with the $\pm\sigma$ sparsification method (see Figs. 4.3l - 4.3n, z-scores: 203.74 for ID 13260, 111.89 for ID 4382 and 14.85 for ID 4698) and none with the $\pm 2\sigma$ method. The two 4-motifs with number 13260 and 4382, the bidirectional ring and the bidirectional star, respectively, have the highest z-scores in the averaged effective connectivity network and are a subset of the significant 4-motifs found for every individual subject (Figs. 4.3l and 4.3m). The overexpression of those two motifs cannot be explained by the higher number of bidirectional links in the effective connectivity network since the null model contains the same number of bidirectional links.

MOTIF-BASED CLUSTERS

Following the approach of [7], we apply the motif-based clustering algorithm on the averaged effective connectivity network. Since for both sparsification methods, the 3-motif with ID 78 was significantly overexpressed in the averaged effective connectivity network and in every subject network, we cluster according to this motif. We find two clusters with the sparsified network for $\pm\sigma$ (Fig. 4.4). The frontal brain regions seem to be consistently part of the red cluster and the distribution of the clusters across the two brain hemispheres shows a strong symmetry (Fig. 4.4). The sparser network resulting from the $\pm 2\sigma$ sparsification method was disconnected. Consequently, we could only obtain a motif-based clustering of the largest connected compo-

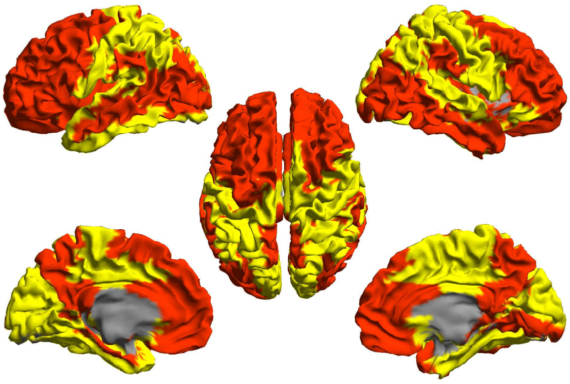

Figure 4.4: The two clusters (in red and yellow) on the template brain obtained via the motif-based clustering algorithm after the $\pm\sigma$ sparsification based on the motif 78.

nent (see Appendix Fig. 4.5).

4.2.3. DISCUSSION AND CONCLUSION

Evaluating the overexpressed motifs for individual human subjects, it is interesting that the 3-motif with ID 78 and its extended 4-node versions have also been overexpressed in other cortical networks of the cat and the macaque brain [88]. In these motifs some nodes seem highly integrated with their neighbors while others are more segregated. Sporns et al. [88] associated these motifs and the absence of triangular shapes with the general principles of integration and segregation in the functional organization of brain networks. This principle originates from studies of neuronal dynamics where signals from many different spatially segregated groups of neurons are integrated with each other forming one coherent signal [86, 103, 129]. In addition, motif 78 can help to identify hubs in structural brain networks by counting the number of times a node participates in that motif [52]. A possible explanation for this identification is that a hub often connects two otherwise disconnected brain regions reciprocally with each other functioning as a 'bridge' for the information flow [52]. Thus, the pre-dominance of motif 78 in the analyzed effective connectivity network suggests that hubs are 'bridges' for the information flow. The impact on the global network could be further investigated by the new metric of 'bridgeness' [53] in future research. Also the other significant 3-motifs are present in brain networks from the literature. For example, motif 6 has been identified in a previous modeling study with Granger causality as the driving structure behind many neuronal dynamics [26].

The fact that the motif-based clustering reveals a strong symmetry between the brain hemispheres is remarkable and supports the idea of a higher-order organization of the effective connectivity brain network. In comparison, the results of a standard spectral clustering algorithm (edge-based conductance) show a much weaker symmetry and a more disconnected spatial distribution of the two clusters (see Appendix Fig. 4.6). However, a rather dense network ($\pm\sigma$) seems to be necessary for the emergence of a higher-order structure since the clustering for the sparser averaged network ($\pm 2\sigma$) appears to be frail (see Appendix Fig. 4.5). Thus, finding an optimal link density for motif-based clustering requires further investigation.

Looking into the obtained clusters, we find that the red cluster in Fig. 4.4 consists of all frontal brain regions and some posterior regions which are known to be the strongest structural hubs [50]. The fact that the motif-based clustering algorithm does not separate posterior hubs and frontal regions suggests that there might be an increased information flow between them. This result strengthens the hypothesis from [50] that the posterior hubs play a crucial role in the global information flow of the effective connectivity. More specifically, posterior hubs in the brain seem to play the role of a 'bridge' for not only the local but also the global information flow. However, this 'bridge' seems to be active in varying pre-dominant directions for different frequency bands [50]. To conclude, our study shows a promising way of integrating local structures to explain the emergence of global patterns in brain networks. This approach might be a first stepping stone towards understanding the information flow in the healthy brain which could, in the future, support the diagnosis of brain disorders.

4.2.4. APPENDIX

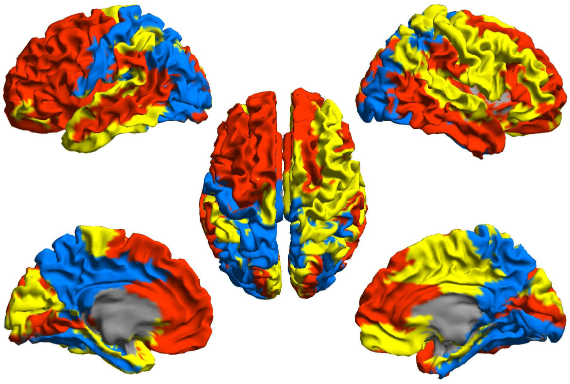

Figure 4.5: The two main clusters (in red and yellow) of the largest connected component on the template brain obtained via the motif-based clustering algorithm after the $\pm 2\sigma$ sparsification based on the motif 78. The blue colored regions were not in the largest connected component.

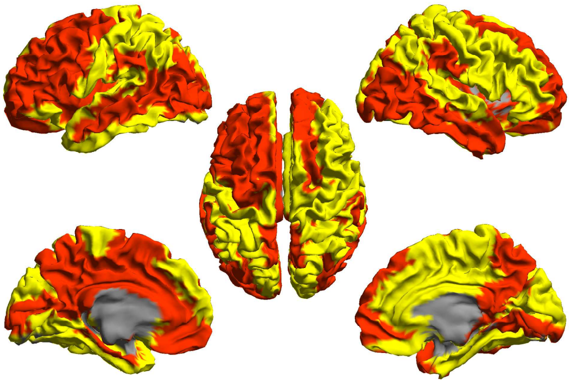

Figure 4.6: The two main clusters (in red and yellow) on the template brain obtained via the spectral clustering algorithm with the $\pm\sigma$ sparsification. In comparison with the motif-based clustering in Fig. 4.4, the red cluster looks more disconnected and does not include all anterior regions anymore.

4.3. BRAIN NETWORK CLUSTERING WITH INFORMATION FLOW MOTIFS (EXTENDED)

Since the building blocks that give rise to the opposite global information patterns are unknown, we investigate in this subchapter the information flow patterns with regard to a smaller scale for different frequency bands. The previous subchapter 4.2 gave evidence that clusterings obtained by Benson et al.'s [7] algorithm are indeed meaningful for effective connectivity networks constructed from a similar measurement, the directed phase transfer entropy (dPTE). We extend this work with results for PTE over a larger number of networks from a specific interval of interest and for two different frequency bands, the *alpha2* and the *theta* band.

4.3.1. FROM MEASUREMENTS TO DIRECTED NETWORKS

MEASURING INFORMATION FLOW IN THE BRAIN

The global directionality of information flow in the brain is shown to be frequency-dependent in a preceding study [50]. To account for this observation, we will study one representative of a higher frequency band (*alpha2* at 10-13 Hz) and one from a lower frequency band (*theta* 4-8 Hz), respectively. Based on the same data as in Chapter 4.2, we calculated the pairwise PTE values (for details we refer to Section 4.2.1). In order to remove individual bias of the measurements, all pairwise PTE values are averaged over all subjects and all epochs. A histogram of those averaged PTEs is shown in Figure 4.7 for the *alpha2* and *theta* frequency band.

NETWORK CONSTRUCTION

The pairwise PTE values between all 78 ROIs imply a fully connected network G_{PTE} where each ROI is a node and the PTE is the weight of each link. In order to filter out noise and focus on the most important connections possessing the highest PTE values, all links with a PTE below or equal a certain threshold τ are discarded (set to zero) and all links above τ remain without a weight (set to one). This procedure eliminates weak connections which might otherwise obscure the inherent topology induced by significantly stronger connections. If (for a fixed h) $PTE_{XY} > \tau$ and $PTE_{YX} > \tau$ for two ROIs X and Y, a bi-directional link between X and Y is set. For $PTE_{XY} \leq \tau < PTE_{YX}$, only a uni-directional link from Y to X is set. Thus, by selecting an appropriate threshold τ, the fully connected weighted network G_{PTE} is transformed into a sparser, directed and unweighted network $G(\tau)$, also known as binary directed network.

Finding an appropriate threshold τ is a challenge in itself [118], which we will not undertake, since one singular value for τ will not be needed for the upcoming analysis. Instead, we consider a class of networks $G(\tau)$ created by sampling some τ from an interval $[\tau_{min}, \tau_{max}]$. Setting $\tau = 0$ results in a fully connected network whereas setting τ to the maximum of all PTE values results in an empty network of 78 isolated nodes. Clearly, these extreme thresholds provide networks that lack of structure and present no insight. To avoid constructing such degenerate networks, we pick a narrower interval as follows.

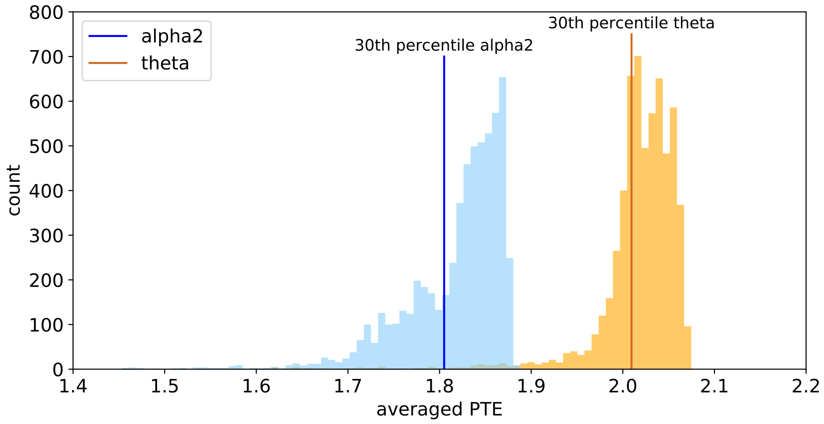

Figure 4.7: PTE between each possible pair of ROIs averaged over all subjects and measurement epochs. In total, 6006 average PTEs are displayed as a histogram with 100 bins for each of the two frequency bands. The *alpha2* frequency band (shown in blue) has on average lower PTEs than the *theta* frequency band (shown in orange). The vertical lines mark the 30th-percentile of each distribution.

Table 4.1: Network properties of $G(\tau)$ for τ at the endpoints of the interval $[\tau_{min}, \tau_{max}]$. For *alpha2* we have $[\tau_{min}, \tau_{max}] = [1.8050, 1.8636]$ and for *theta* $[\tau_{min}, \tau_{max}] = [2.0095, 2.0535]$.

	alpha2		***theta***	
	$G(\tau_{min})$	$G(\tau_{max})$	$G(\tau_{min})$	$G(\tau_{max})$
#uni-directional links	1006	848	648	799
#bi-directional links	1601	81	1776	56
average degree	53.949	12.949	53.846	11.679
assortativity	-0.105	-0.129	-0.351	-0.062
link density	0.700	0.168	0.700	0.152

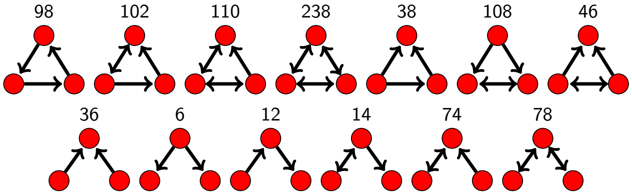

Figure 4.8: All possible 13 connected 3-motifs. The motif ID in binary represents the 3 × 3 adjacency matrix of the motif.

We set τ_{max} to be the smallest threshold at which the obtained network is still weakly connected, i.e. has no isolated nodes. To avoid having too many weak connections, τ_{min} is set to the 30%-percentile of the PTE distributions (see Figure 4.7). This value eliminates a fair amount of weak connections while the majority of the strongest connections persist.

The networks within $[\tau_{min}, \tau_{max}]$ are all connected, but sparse enough to resemble complex structures. At τ_{max} itself, the link density is 0.168 for *alpha2* and 0.152 for *theta*, whereas the 30%-percentile of τ_{min} corresponds to networks with a link density of 0.7. This allows to cover a large variety of different networks in $[\tau_{min}, \tau_{max}]$, each representing a different perspective on the underlying data. For example, we observe that the assortativity for *theta* frequency band data ranges from -0.351 to -0.062 and that the ratio between uni-directional and bi-directional links is changing as well. Table 4.1 contains the exact values of τ_{min} and τ_{max} together with some properties of networks exactly at the interval endpoints.

4.3.2. INFORMATION FLOW MOTIFS

MOTIF SEARCH

Our motif search is performed with the *mfinder* software [54]. For this study, our main focus is on the 13 different 3-motifs as shown in Figure 4.8. Each motif is identified by a number whose binary representation translates to the adjacency matrix of the corresponding motif. This notation is consistent with the one used in *mfinders* documentation.

When given any network G (to which we refer as "original network"), the *mfinder* program performs two tasks: first, it counts the frequency $J_{G,M}$ of all motifs M of G and second, it generates a number of random networks with similar properties as the original network and determines the motif frequencies in each of them as well. For every original network, *mfinder* generates 1000 random networks using the switching algorithm described in [63] with 100 switches. We use the default parameters for *mfinder*, which preserve the degree sequence of the original network and the number of bi-directional links.

The random networks are used as a null model to determine which motifs are *overexpressed* in the original network. More precisely, we are using the criteria given in the supplemental material of Milo et al. [68]. These criteria are:

i) The probability P of having an equal or greater motif frequency in a random network than in the original network is less than 0.01.

ii) The motif appears at least 4 times with disjoint nodes in the original network.

iii) The ratio of the motif frequencies between the original and the random networks is at least 1.1.

Given the mean $\mu(J_{rand,M})$ and the standard deviation $\sigma(J_{rand,M})$ of the motif frequency in the random networks, the magnitude of overexpression of motif M in G is given by its z-score

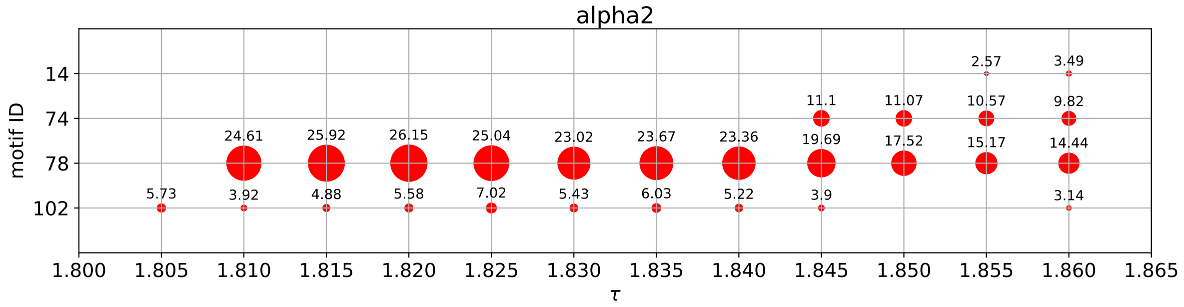

Figure 4.9: Overexpressed 3-motifs for *alpha2* frequency band data in the interval $[\tau_{min}, \tau_{max}]$. The area of the circles scales with the z-scores. The numerical value of the z-scores is plotted on top of each circle for better comparison.

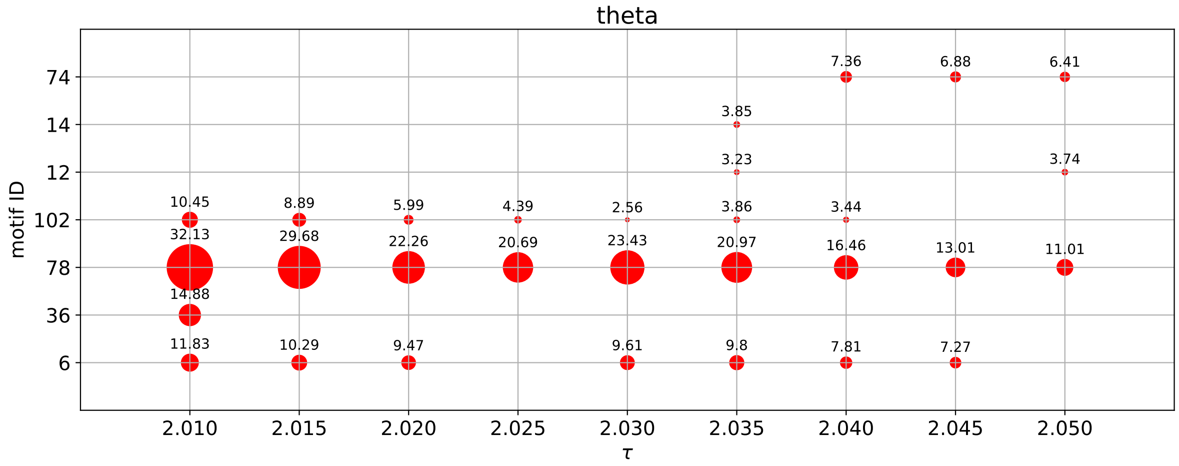

Figure 4.10: Overexpressed 3-motifs for *theta* frequency band data in the interval $[\tau_{min}, \tau_{max}]$. The area of the circles scales with the z-score. The numerical value of the z-score is plotted on top of each circle for better comparison.

$$z_{G,M} = \frac{J_{G,M} - \mu(J_{rand,M})}{\sigma(J_{rand,M})}. \tag{4.5}$$

A motif which is not overexpressed may still occur quite frequently in the original network, though it arises at a similar frequency by a random link rewiring process. Thus, it can be argued that overexpressed motifs carry some functional importance for the underlying system since they do not arise merely by chance.

OVEREXPRESSED MOTIFS IN FUNCTIONAL BRAIN NETWORKS

We sample the interval $[\tau_{min}, \tau_{max}]$ with a step-size of $\Delta = 0.005$, for both *alpha2* and *theta* frequency band data. For each sampled threshold τ, we construct $G(\tau)$ and use it as the original network for mfinder and determine all overexpressed motifs with their z-score. Figure 4.9 shows the overexpressed motifs for *alpha2* and Figure 4.10 for *theta* frequency band data.

We observe that motif overexpression depends on the chosen threshold τ. For example, in the *alpha2* frequency band data motif 74 and motif 14 were only detected in very sparse networks close to the connectivity threshold τ_{max} (Figure 4.9). It is also possible that there are gaps at certain ranges of τ in which a motif does no longer fulfill all overexpression criteria, e.g. motif 102 for *alpha2* or motif 6 for *theta*.

From all overexpressed motifs, motif 78 stands out for the following reasons. First, motif 78 is overexpressed in both, *alpha2* and *theta*, for a large part of the interval $[\tau_{min}, \tau_{max}]$ without any gaps. Second, the z-scores of this motif are always higher than the z-scores of any other overexpressed motif for the corresponding sampled thresholds. Hence, we select motif 78 as our motif M for the upcoming motif-based clustering.

4.3.3. MOTIF-BASED CLUSTERING

Benson et al. [7] developed a clustering algorithm that partitions a network G based on a motif M. The main idea of their algorithm is to construct clusters by “cutting” through the minimum possible number of motif instances, while maintaining a high density of motif instances within each of the clusters. In this section, we summarize only the basic concepts (including the algorithm) necessary to understand how the clustering of the networks was achieved. Details about the performance, complexity and additional applications can be found in the supplemental material of [7] together with a comprehensive analysis of the algorithm.

MOTIF ADJACENCY MATRICES

Let G be a directed network with a set of nodes $\mathscr{N} = \{1, 2, \ldots, N\}$. For each pair of nodes i, j let w_{ij} be the number of node-disjoint motif instances in which i and j participate together. Then, the matrix $(W_M)_{ij} = w_{ij}$ is called *motif adjacency matrix*. The *motif diagonal degree matrix* D_M is given by

$$(D_M)_{ii} = \sum_{j=1}^{N} (W_M)_{ij}$$

and the *motif Laplacian* by

$$L_M = D_M - W_M.$$

The clustering algorithm uses the eigenvector belonging to the second smallest eigenvalue of the *normalized motif Laplacian*, which is defined as

$$\mathscr{L}_M = I - D_M^{-\frac{1}{2}} W_M D_M^{-\frac{1}{2}}$$

where I denotes the identity matrix. For a graph $G(\tau)$ based on a threshold τ the corresponding motif adjacency matrix is denoted by $W_M(\tau)$.

MOTIF CONDUCTANCE

Given the motif adjacency matrix W_M of a network G, and a partition of the nodes $N = |\mathscr{N}|$ into two disjoint subsets $\mathscr{N}_1$ and $\mathscr{N}_2 = \mathscr{N} \setminus \mathscr{N}_1$, we define the motif conductance $\phi_G(\mathscr{N}_1, \mathscr{N}_2)$ of that partition as

$$\phi_G(\mathscr{N}_1, \mathscr{N}_2) = \frac{\mathrm{cut}_G(\mathscr{N}_1, \mathscr{N}_2)}{\min\{\mathrm{vol}_G(\mathscr{N}_1), \mathrm{vol}_G(\mathscr{N}_2)\}}$$

with

$$\mathrm{cut}_G(\mathscr{N}_1, \mathscr{N}_2) = \sum_{i \in \mathscr{N}_1, j \in \mathscr{N}_2} (W_M)_{ij}$$

and for $a = 1, 2$

$$\mathrm{vol}_G(\mathscr{N}_a) = \sum_{i \in \mathscr{N}_a} \sum_{j}^{N} (W_M)_{ij} = \sum_{i \in \mathscr{N}_a} (D_M)_{ii}.$$

Thus, $\phi_G(\mathscr{N}_1, \mathscr{N}_2)$ gives us the ratio between the number of motif-instances cut by the partition $\{\mathscr{N}_1, \mathscr{N}_2\}$ and the lowest number of preserved motif-instances in one of the two partitions.

MOTIF-BASED CLUSTERING ALGORITHM

A low conductance is often a desirable quality for a network clustering [30]. However, finding the minimum conductance of a network is a well-known $\mathscr{NP}$-complete problem [36] which directly translates to the complexity of finding the minimum motif conductance ϕ_G^*. Benson et al. [7] present a polynomial-time algorithm that finds a nearly optimal partition $\{\mathscr{N}_1, \mathscr{N}_2\}$ with motif conductance

$$\phi_G(\mathscr{N}_1, \mathscr{N}_2) \leq 4\sqrt{\phi_G^*}$$

for 3-motifs. In practice, the runtime is largely dominated by the computation of the motif adjacency matrix, which is still efficient for the motifs of size three that we consider for this work.

The algorithm from Benson et al. [7] is a generalization of the classical spectral clustering algorithm [111, 120], which makes use of the Laplacian matrix of a network. The eigenvector corresponding to the second smallest eigenvalue of this matrix is known as Fiedler’s vector [31] and by ordering its elements, a node partition of a low (link-based) conductance can be devised.

The main steps of the algorithm from Benson et al. [7] consist of computing the motif adjacency matrix W_M from which the normalized motif Laplacian $\mathcal{L}_M$ is constructed and the second smallest eigenvalue is computed. Afterwards, the corresponding eigenvector is used to create a partition $\{\mathcal{N}_1, \mathcal{N}_2\}$ according to the smallest motif conductance. Nodes that do not participate in any instance of motif M can yield a motif conductance that is not defined and thus are not considered to be part of neither $\mathcal{N}_1$ nor $\mathcal{N}_2$.

The complete algorithm is listed as Algorithm 1 in pseudocode. An implementation was done by us in Python (using NumPy and NetworkX) and our results were double-checked with the implementation available on the SNAP-platform [56].

Algorithm 1 Motif-based clustering algorithm by Benson et al. [7]

```
Input: Directed, unweighted network $G$ and motif $M$
Output: Motif-based clusters $\mathcal{N}_1$ and $\mathcal{N}_2$ (subsets of nodes)
$(W_M)_{ij} \leftarrow$ number of instances of $M$ that contain nodes $i$ and $j$
$D_M \leftarrow$ diagonal degree matrix of $W_M$
$\mathcal{L}_M \leftarrow I - D_M^{-\frac{1}{2}} W_M D_M^{-\frac{1}{2}}$ normalized motif Laplacian
$z \leftarrow$ eigenvector corresponding to second smallest eigenvalue of $\mathcal{L}_M$
$\sigma_i \leftarrow$ index of vector $D_M^{-\frac{1}{2}} z$ with $i$th smallest value
$\ell \leftarrow \arg\min_{i=1,\dots,\mathcal{N}} \phi_G(\{\sigma_1,\dots,\sigma_i\},\{\sigma_{i+1},\dots,\sigma_N\})$
$\{\mathcal{N}_1,\mathcal{N}_2\} \leftarrow \{\sigma_1,\dots,\sigma_\ell\},\{\sigma_{\ell+1},\dots,\sigma_N\}$
return $\{\mathcal{N}_1,\mathcal{N}_2\}$
```

MOTIF-BASED CLUSTERING OF FUNCTIONAL BRAIN NETWORKS

In order to apply the motif-based clustering to the brain, we have to fix a motif. For reasons already mentioned in Section 4.3.2, we select M to be motif 78. While Algorithm 1 works on a single network G, we want to construct a partition that takes networks created by different thresholds from $[\tau_{min}, \tau_{max}]$ into account. While there exists an infinite amount of different thresholds τ in the interval $[\tau_{min}, \tau_{max}]$, the corresponding network only changes at a finite subset $\mathrm{T} \subseteq [\tau_{min}, \tau_{max}]$ of them. The elements in T are exactly the PTE values of all the links that are present in $G(\tau_{min})$ without the set of links present in $G(\tau_{max})$. Summing the motif adjacency matrices over all elements in T results in an *aggregated motif adjacency matrix*

$$W_{M_{agg}} = \sum_{\tau \in \mathrm{T}} W_M(\tau) \tag{4.6}$$

for each frequency band. Applying the motif-based clustering to this matrix constructs a partition that has on average a low conductance over the interval $[\tau_{min}, \tau_{max}]$ (TO BE SHOWN?). The results of the partition into 2 clusters are shown in Figure 4.11 for the *alpha2* frequency band data and in Figure 4.12 for the *theta* frequency band data.

4.3.4. DISCUSSION

We simplified the construction of directed networks in comparison with our previous study 4.2. In the earlier work, we computed the directed PTE (dPTE) value defined as

$$dPTE_{XY} = \frac{PTE_{XY}}{PTE_{XY} + PTE_{YX}} \tag{4.7}$$

for each direction and extracted the links with significantly high or low dPTE values. Thereby, we focused on the highly asymmetric pairwise relations representing a strong sending and a more receiving node. Thus, between node pairs with low average PTE values in both directions none of the network construction methods assigned a link. In the present study, the strongly assymmetric relations are still represented in the network but we additionally included those symmetric relation where both directions possess high PTE values. In contrast to our previous study 4.2, we did not need to fix any threshold but rather considered a whole range of them for the network construction.

Concerning network motifs, we observed an overexpression of motif 78 in line with our previous study 4.2. Two other motifs, 14 and 74, which can be regarded as degenerated forms of motif 78 missing one unidirectional link, have also been identified as overexpressed in both of our studies. Thanks to the overview

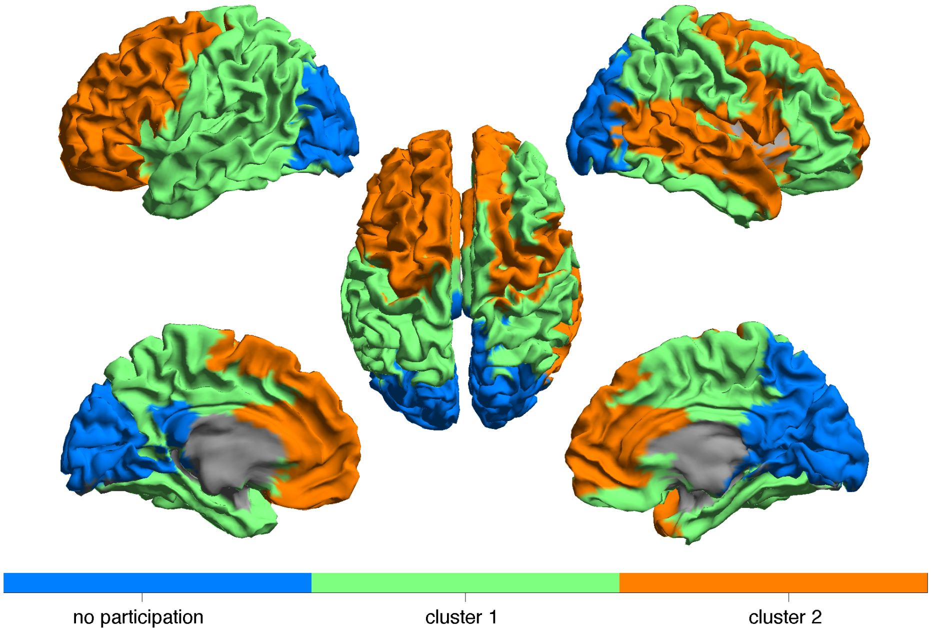

Figure 4.11: Partition of brain networks for *alpha2* frequency band data based on motif 78 into two clusters of nodes. 15 out of 78 nodes did not participate in any motif instance and are shown as a separate third cluster.

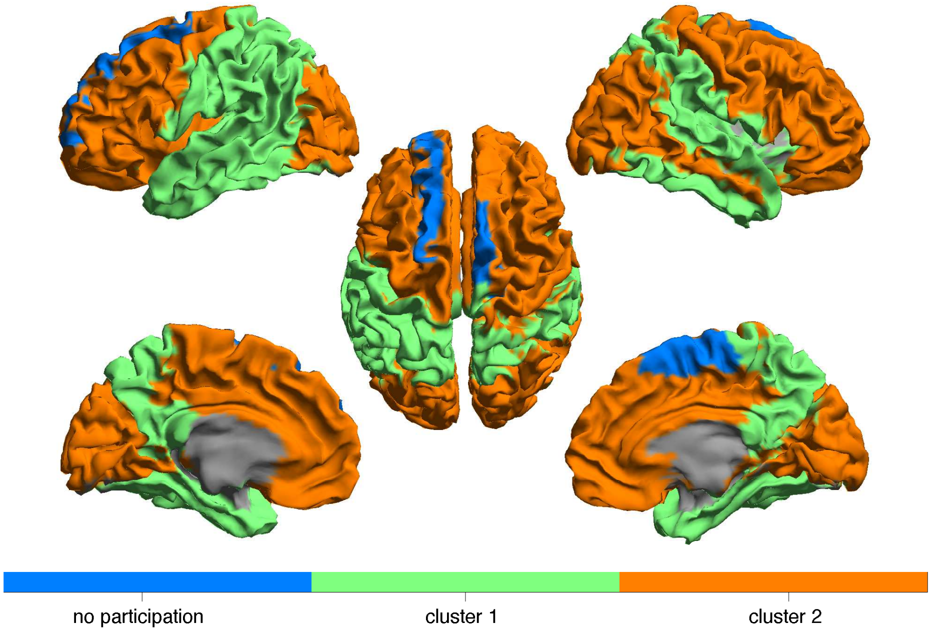

Figure 4.12: Partition of brain networks for *theta* frequency band data based on motif 78 into two clusters of nodes. 2 out of 78 nodes did not participate in any motif instance and are shown as a separate third cluster.

over a range of thresholds in this extended study, we can explain the origins of the overexpression of these related motifs: Since motifs 14 and 74 are only overexpressed for higher thresholds τ and, thus, only for sparser networks, this result seems to be a direct consequence of the applied threshold removing the weakest link in motif 78. Thus, motifs 14 and 74 are most likely consequences of the applied threshold not representing new triangular relations but supporting the overall dominance of motif 78.

The overexpression of motif 78 is also in line with other previous research stating the same result for the structural brain networks of the macaque and the cat [88]. The connectivity profile of motif 78 identifies a central node connecting two otherwise disconnected brain regions. Thus, the central node in motif 78 acts as a *bridge* for the information flow between its neighbors and the overexpression of motif 78 could represent the basic principle of segregation and integration on the macroscopic level of brain regions [88]. The principle of segregation and integration originates from neuronal dynamics where signals from spatially segregated neurons are integrated with each other into one coherent signal [86, 103, 129]. Further, Honey and coauthors [52] showed a high correlation for nodes between being a hub and frequent participation in the motif 78. The overexpression of motif 78 together with its close relation to hubs confirms previous findings identifying hubs as drivers for the integration of information flow [38, 87, 107]. In addition, the overexpression of motif 78 in both frequency bands, *alpha2* and *theta*, strengthens the claim even further that motif 78 is a general building block of effective connectivity networks and therefore an important feature for the information flow in brain networks.

When analyzing the global intertwined organization of motif 78, we identified spatially coherent clusters in both frequency bands. Overall, the motif-based clustering algorithm split the brain in three major parts, the frontal lobe, the occipital lobe and the rest corresponding to a joint cluster of temporal and parietal lobe. Without including any spatial information in the construction of the directed networks or any restriction on locations for the performed clustering, we were able to recognize this well-known global spatial organization of the human brain in our obtained clusters. As a commonality between the *alpha2* and *theta* frequency band, the frontal regions seem to be nearly consistently together in one cluster. However, in alignment with the recent study of Hillebrand et al. [50] we also observe differences in the global patterns between high and low frequency bands: Whereas in the *theta* frequency band, the posterior regions (more precisely the occipital lobe) belong together with the frontal lobe in one cluster and thus participate in motif 78 together with the frontal lobe, the occipital lobe in the *alpha2* frequency band does not participate in motif 78. For the *theta* frequency band, the frontal and the occipital lobe apparently share many interactions in the form of motif 78 because the clustering algorithm does not split them. This strong higher-order interaction between posterior and frontal brain regions could facilitate the discovered global information flow between frontal and posterior regions [20, 50].

4.3.5. CONCLUSION

The motif search for different frequency bands resulted in the dominant overexpression of motif 78 over a wide range of thresholds. This motif, which was also observed in previous studies, seems to represent a general building block for the information flow in functional brain networks resembling the organizational principle of segregation and integration. The motif-based clustering revealed the higher-order organization of effective connectivity on a global scale. The differences between higher and lower frequency bands could be traced back to the interaction pattern between the occipital lobe and the frontal brain regions. In the *theta* frequency band, the frontal regions participated in many instances of motif 78 together with the occipital regions pointing towards a strong information flow between those spatially segregated areas. Future work should not only investigate different data sets of healthy controls but also analyze the possible disruptions of information flow and its higher-order organization for patients suffering from neurological disorders.

5

A MAPPING BETWEEN THE STRUCTURAL AND FUNCTIONAL BRAIN NETWORKS

5.1. INTRODUCTION

The collection of the functional connections in the human brain is often referred to as the functional network and is facilitated by the underlying structural network, i.e. the set of physical connections between neuronal populations. At the same time, functional connections influence modulations of these physical connections by long-term potentiation, plasticity or neuromodulation. In recent years, there has been an increasing interest to understand the emergence of functional brain networks given the constraints of the underlying structural network [1, 24, 51, 83]. However, the mutual relationship between the structural and functional networks remains highly debated [23, 77, 78].

Empirical studies have revealed an overlap between structural and (resting-state) functional connections, i.e. the presence of both a structural and functional connection between two brain regions [47, 85, 108]. However, this overlap is imperfect as functional interactions between brain regions exist in absence of direct structural connections, and also indirect structural connections with the length of two links cannot fully account for these functional connections either [51]. Moreover, the overlap between structural and functional connections also depends on the time scale considered, where functional connections estimated from larger time windows strongly overlap with the underlying structural connections, for smaller time windows there can be a structural-functional network discrepancy due to distributed delays between neuronal populations that cause transient phase (de-)synchronization [52, 66, 102].

On larger time scales, several properties of the underlying structural network have been shown to play an essential role in shaping the functional networks, such as the Euclidian distance between two brain regions [3]. However, taking into account Euclidean distance alone is insufficient to explain the emergence of long-range functional connections [119]. Two recent studies showed that such long-range functional connections may be explained by the product of the degree of two nodes in the structural network, indicating the crucial role of structural hubs for explaining long-range functional connections [90, 96]. Moreover, Goñi and colleagues [41] demonstrated that shortest paths in the structural network and perturbations from these paths are strong predictors for functional connections as these paths are favorable because of metabolic efficiency and fast communication.

Given these dependencies between structural and functional networks, the challenge is to integrate these different interdependencies into a single framework, for which we may need a more abstract representation. For example, a significant overlap in the connectivity profile of structural and functional networks suggests that part of the functional network connectivity matrix is a linear mapping from its structural counterpart. In addition, functional connections can also be accounted for by several other higher order features of the structural network as outlined above, which refer to non-linear relationships (see [96] for an example of such non-linearity). Based on the presence of these linear and non-linear features of the relationship between structural and functional networks, we go one step further by assuming that there is a mathematical function

---

This chapter has been published in J. Meier, P. Tewarie, A. Hillebrand, L. Douw, B.W. van Dijk, S.M. Stufflebeam and P. Van Mieghem, *A mapping between structural and functional brain networks*, *Brain Connectivity*, **6**(4), pp. 298-311 (2016).

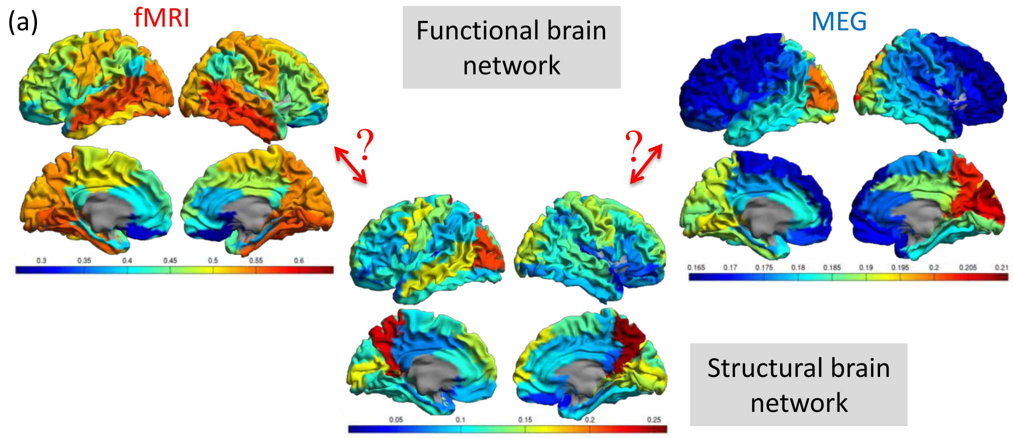

(b) Mapping between their adjacency matrices.

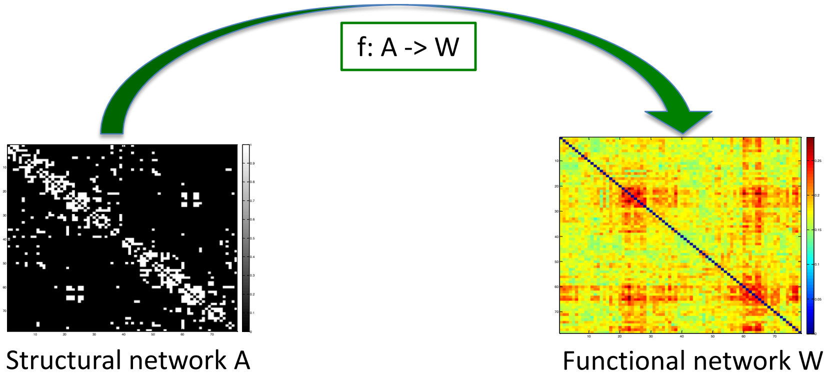

Figure 5.1: (a) Visualization of the structural and functional brain network (for fMRI and MEG) for the group-averaged data set, the colors of the different regions represent here their node strength (i.e. the sum of their surrounding link weights). (b) Visualization of the mapping between their adjacency matrices.

that maps the adjacency matrix of the structural network onto that of the (resting-state) functional network and vice versa (see Figure 5.1(b) and Eq. (5.1) below). If we further assume that our mathematical function is analytic [101, 124], then the map between structural and functional network can be expressed by a weighted sum of the matrix powers as explained in Section 5.2.2. Our method consists of a *data-driven approach*, from which the successive coefficients of this matrix mapping are determined. The major advantage of our method is that an a-priori specific form of a function is not needed. Another implication of such a function is the possible existence of an inverse function, i.e. a mapping from functional networks back to structural networks.

Most previous studies have found relationships between structural and functional networks using a single functional neuroimaging modality [19, 51], often using functional MRI (fMRI). As the fMRI response is an indirect measure for neuronal activity and contains non-neuronal signals, a structure-function dependency based on this modality could deviate from the same dependency derived from neuroimaging modalities that directly measure neuronal activity and connectivity. In contrast to fMRI, magnetoencephalography (MEG) measures neuronal activity and connectivity directly with excellent temporal resolution. However, given the increasing interest in multimodal imaging approaches there is a need to understand the modality dependency of the structure-function relationship in a single framework. A data-driven approach in the form of a matrix function may be helpful when investigating the modality dependency of the structural-functional network relationship: different modality-dependent coefficients may point to different specific functions for each modality. The relevance of elucidating the modality dependency of a mathematical function can be extended to the clinical field where we could answer questions such as: which modality would be the most sensitive for picking up functional network changes given disease-specific structural network damage?

The aim of the present study is to analyze the structural-functional network relationship through a mathematical function in a multimodal framework. We use two datasets containing multimodal imaging data ranging from diffusion tensor imaging (DTI) data to MEG and fMRI data. We extend our analysis by also considering the relationship between structural and functional networks at the subject level in a third data set and finally discuss how that relationship can be interpreted neurobiologically.

5.2. MATERIALS AND METHODS

5.2.1. PARTICIPANTS AND DATA ACQUISITION

In total, we use three data sets, which all have been used in different previous studies. The first two data sets are group-averaged data sets, obtained from two different centers, but analyzed together in one mapping.

(i) A group-averaged structural imaging data set, i.e. a DTI network from 80 healthy subjects in 78 cortical automated anatomical labeling (AAL) brain areas [40].

(ii) Two group-averaged data sets with functional imaging data, i.e. resting-state MEG and fMRI signals in the same 78 AAL cortical areas, one with 17 and another with 21 healthy subjects [96, 98].

(iii) An individual data set from 11 healthy subjects structural and functional imaging data, i.e. with DTI, resting-state MEG and fMRI time-courses in 219 brain areas [27].

For the group-averaged structural connectivity matrix, we use a literature-based structural network (data set (i)) [40]. In every subject, cortical regions in the AAL atlas were considered to be connected if the end points of two white matter tracts were located in these regions [40]. Then, a group-averaged structural connectivity matrix was obtained by testing each possible connection for its significance using a non-parametric sign test.

For the group-averaged functional imaging data set (data set (ii)), we use data obtained from our own imaging center. We employ the first data set with 17 healthy controls for our main analysis and the second data set from 21 healthy controls only for validation [96, 98]. The study was approved by the institutional ethics review board of the VUmc and all subjects gave written informed consent prior to participation. Both fMRI and MEG data sets underwent to some extent different pipelines [96, 98] and are obtained from two different MEG scanners (CTF and Elekta). Detailed information about data acquisition and post-processing can be found in the previous papers. In short, for both MEG and fMRI cortical networks were constructed using the same cortical AAL regions as for the structural network consisting of 78 cortical regions [40]. The Pearson correlation coefficient was computed between time signals to construct functional networks for fMRI for each subject (the absolute value was taken to avoid negative matrix elements). For MEG, a beamformer approach was used to reconstruct neuronal activity in AAL regions. Subsequently, the phase lag index (PLI), a measure for phase-synchronization, was computed between time series to reconstruct a functional connectivity matrix for each subject in the *alpha2* frequency band (10 – 13 Hz) [91]. The present study can be considered as a continuation from previous work where we found a strong relationship between structural and functional networks in the *alpha2* band and therefore we limited our analysis to this frequency band, although the fit could be generalized [96]. Similar to the structural connectivity matrix, we averaged functional connectivity matrices across subjects for fMRI and MEG separately to obtain one group-averaged functional connectivity matrix for each modality. The averaging over multiple subjects was pursued in the attempt of reducing noise.

For the individual data set (data set (iii)), eleven healthy participants were included, exclusion criteria being psychiatric or neurological disease and use of medication influencing the central nervous system. This study was approved by MGHs institutional review board, and was performed in accordance with the Declaration of Helsinki. All participants gave written informed consent before participation. Pre-processing methodology of the DTI and fMRI data has been described in detail before [27]. In short, a surface-based atlas approach was used for connectivity analysis of the fMRI and DTI data, using a parcellation scheme with 219 cortical surface parcels [18, 37]. In addition, for every entry of the fMRI-based adjacency matrix the absolute value was taken to avoid negative matrix elements. MEG eyes-open resting-state data were collected in a magnetically shielded room with a 306-channel whole-head system (Elekta-Neuromag, Helsinki, Finland) and a sampling rate at 1037 Hz. Vertical and horizontal electro-oculograms were acquired simultaneously for off-line eye-movement artifact rejection. Head positions relative to the MEG sensors were recorded from four head-position indicator coils attached to the scalp. Landmark points of the head were digitized using a 3-D digitizer (Polhemus FASTRAK). MEG data underwent a number of pre-processing steps: (1) bad channel and bad epoch rejection, (2) eye-movement artifact removal via Signal Space Projection (SSP), (3) downsampling with a decimate factor of 8 (to reduce computational expense). To compute the physical forward solution (lead fields), a single-layer boundary element method was applied to model the brain volume conduction, following an established procedure [46]. The lead field of freely-oriented dipoles was then evaluated at each location. In solving the inverse problem, current density at each source location was approximated by a minimum 2-norm estimate in the same six frequency bands as was used for the second dataset [45], with noise covariance computed from empty-room recordings on the same day (also band-pass filtered). For each subject, the cortical surface defined by the boundary between the gray and the white matter was reconstructed using FreeSurfer [32], after which time series from the abovementioned 219 cortical surface parcels were reconstructed. The PLI was used as a connectivity measure on these time series [91]. An average connectivity matrix per participant was calculated over all epochs.

5.2.2. MATHEMATICAL BACKGROUND

We will refer to matrix A as the binary adjacency matrix of the structural network for the group-averaged data (data set (i)) and to matrix W as one of the possible representations of the functional networks, W_{MEG} for MEG functional networks and W_{fMRI} for fMRI functional networks. Both A and W are $N \times N$ symmetric matrices, where N equals the number of cortical regions ($N = 78$ for data set (i) and (ii); $N = 219$ for data set (iii)). For both group-averaged and individual data, the matrix W has real elements w_{ij} between 0 and 1. In the case of the individual data, the structural network is described by a weighted adjacency matrix V with real elements between 0 and 1. As mentioned before, we assume that there exists a function f such that

$$W = f(A) \tag{5.1}$$

or $W = f(V)$ in the case of a weighted structural connectivity matrix V (see also Figure 5.1). Under quite mild conditions [62], the inverse f^{-1} of the function f exists such that

$$A = f^{-1}(W). \tag{5.2}$$

If $f(z)$ is a function of the complex number z and analytic in a disk with radius R around z_0, then $f(z)$ possesses a Taylor series in the complex plane $\mathbb{C}$ that converges for all points z that lie in a disk with radius R around the point z_0,

$$f(z) = \sum_{k=0}^{\infty} f_k(z_0)(z - z_0)^k \qquad \text{with} \qquad f_k(z_0) = \frac{1}{k!}\left.\frac{d^k f(z)}{dz^k}\right|_{z=z_0}, \tag{5.3}$$

where $|z - z_0| < R$ and R is called the radius of convergence [101, 124]. It can be shown [48, 111] that, if $f(z)$ is analytic around z_0 and, hence, possesses a Taylor series (5.3), then for all matrices A, the matrix function $f(A)$ also satisfies this Taylor series, provided each eigenvalue λ of A obeys $|\lambda - z_0| < R$. Caley-Hamilton's famous theorem [111] states that any square matrix A satisfies its own characteristic polynomial, which implies that we can write $A^N = p_{N-1}(A)$, where $p_n(z)$ is a polynomial of degree n in z. Iteratively using the Caley-Hamilton theorem to the powers of $k \geq N$ in Eq. (5.1),

$$f(A) = \sum_{k=0}^{N-1} f_k(z_0)(A - z_0 I)^k + \sum_{k=N}^{\infty} f_k(z_0)(A - z_0 I)^k$$

shows that $\sum_{k=N}^{\infty} f_k(z_0)(A - z_0 I)^k$ can be written as a polynomial of order at most $N - 1$ in A. In summary, any analytic function f, defined by (5.3), of a matrix A is a polynomial in A of degree at most $N - 1$ (N is the number of nodes, here cortical regions, in the network),

$$f(A) = \sum_{k=0}^{N-1} c_k[f]\, A^k, \tag{5.4}$$

where $c_k[f]$ are coefficients depending on the function f (provided each eigenvalue λ of A lies within the disk, i.e. obeys $|\lambda - z_0| < R$). Because all the analyzed matrices have only zeros on the diagonal, their *trace* is 0. Since the *trace* equals the sum of the eigenvalues of a matrix [111], the average of the eigenvalues of the empirical matrices here is zero, which suggests us to choose $z_0 = 0$.

5.2.3. MATHEMATICAL METHODOLOGY

The first term $c_0[f] \cdot I$ in Eq. (5.4), which is the product of the constant coefficient $c_0[f]$ and the identity matrix I, provides an offset to adjust the diagonal elements of our fitted matrix. In order to obtain a better goodness of fit, we introduce an offset also for all non-diagonal elements of our matrix. We define this offset as the error matrix $E = c \cdot J$, where $J = u \cdot u^T$ is the all-one-matrix, $c \in \mathbb{R}$ and u is the all-one vector, $u = (1, \ldots, 1)^T$. The constant error matrix E can be justified as a first approximation of the part that we do not know yet about the mapping between the structural and functional brain network. Thus, our fitting function is defined as

$$f_{(K)}(A) = \sum_{k=0}^{K} c_k[f] A^k + E \tag{5.5}$$

where $K \leq N - 1$ is the maximal fitted exponent (N is the dimension of matrix A). We use the non-linear regression algorithm in MATLAB (using the routine *nlinfit.m* version *R2015a*) to estimate the coefficients in Eq. (5.5) by iterative least-squares estimation (for details see SI Section 5.6.7). Denoting $\widetilde{W} := f_{(K)}(A)$, we evaluate the goodness of fit of our mappings using the Frobenius norm [113, p. 549]. In particular, we compute the sum of squared errors (SSE), slightly modified as

$$SSE := \sum_{i=1}^{N} \sum_{j=1}^{i} (w_{ij} - \widetilde{w}_{ij})^2 \tag{5.6}$$

where $N = 78$ regions in the case of the group-averaged data and $N = 219$ in the case of the individual data. Here, we only sum the elements of the lower triangular and the diagonal, because all our matrices are symmetric. Since the sum of squared errors is proportional to the number of fitted elements and to compare the different data sets with each other, we introduce a normalized version of SSE where we divide SSE by the degrees of freedom, which is in our case the number of fitted elements minus one

$$SSE_{norm} := \frac{\sum_{i=1}^{N} \sum_{j=1}^{i} (w_{ij} - \widetilde{w}_{ij})^2}{df_{top}}, \tag{5.7}$$

where $df_{top} = N \cdot (N-1)/2 + N - 1$, N number of regions. Similarly, we can define the goodness of fit measure from Eq. (5.7) for the function $f^{-1} : W \to A$ by interchanging W and A in the description above. When we map all entries of one matrix onto the entries of another matrix, we implement our matrix mapping in the so-called topological domain (at the level of the whole adjacency matrix). The same mapping can also be analyzed in the spectral domain, i.e. at the level of the eigenvalues of the matrices (see SI Section 5.6.1).

5.3. RESULTS

MAPPING STRUCTURAL NETWORKS TO FUNCTIONAL NETWORKS

Mapping structural networks to functional networks Firstly, we estimated the coefficients in Eq. (5.5) for the mapping from structural networks to functional networks at the group level (see SI Table 5.3 for $K = 6$). For both modalities, we can observe that the SSE_{norm} becomes lower, i.e. the fit becomes better, for increasing number of terms (Figure 5.2b). Similarly, with an increasing number of fitted coefficients in Eq. (5.5), the patterns of the fitted functional connectivity matrices resemble better the empirical fMRI and MEG connectivity matrices (Figure 5.2a, for a complete list of the ROIs see SI 5.6.2). However, for the group-averaged data, there seems to be a limit for the number of terms, since including terms of 6th order and higher did not significantly improve the estimation anymore for both MEG and fMRI under the 5% significance level. For these group-averaged networks, the best fit was reached for the mapping $f : A \to W_{MEG}$. We obtained significantly different values of the estimated coefficients for the two different modalities under the 5% significance level (see SI Figure 5.15, 95% confidence intervals did not overlap), indicating a modality-dependent mapping. For the mapping $f : A \to W_{fMRI}$, estimated coefficient values showed a clear decrease when going from lower to higher order terms, indicating that lower order terms in the expansion (5.5) contribute more to the estimation of the fMRI network (SI Figure 5.15). For the mapping $f : A \to W_{MEG}$, this steep decline in coefficients for higher order terms was not observed (see SI Figure 5.15). The SSE_{norm} for the data set of individual healthy controls was slightly higher (i.e. worse) than for the group-averaged matrices (Figure 5.2c). Similar to the group level results, the mapping from structural to MEG networks provided better fits than from structural to fMRI networks also at the individual level.

We repeated the same analysis where either the structural or functional connectivity matrices were substituted by a reshuffled version of the empirical matrix (for details see SI Section 5.6.7). The results of this analysis are also displayed in Figure 5.2b, showing a higher SSE_{norm} for all reshuffled cases compared to the original matrices, that is, the empirical results differed significantly ($p < .001$) from the reshuffled results. In addition, we observe that the decline in SSE_{norm} was in most cases for the reshuffled matrices rather narrow in comparison with the empirical matrices (Figure 5.2b). Thus, the observed relationship between structure and function can hardly be reproduced by any reshuffled versions of the matrices. For individual networks, the average performance of the reshuffled matrices was also worse than the empirical original results (Figure 5.2c). We tested the empirical results versus their reshuffles for significant difference with a Mann-Whitney-Wilcoxon (MWW) test and displayed the p-values in Table 1. From this test results, we can conclude that the mapping $f : V \to W_{fMRI}$ was able to outperform its random reshuffle for all subjects (see Table 1). But the goodness of fit for the mapping $f : V \to W_{MEG}$ was for 5 out of 11 subjects not better than the random reshuffles, indicating that the relation between the two matrices is less unique than for the anatomical matrix and the fMRI matrices. In order to cross-validate our mapping, we ran the same analysis on a second group-averaged data set (with similar processing pipeline) and found overlapping confidence intervals for the estimated coefficient values (Figures 5.3a and 5.3b).

MAPPING FUNCTIONAL NETWORKS TO STRUCTURAL NETWORKS

By reversing the role of A and W and following the same approach as before, we obtained goodness of fit values for the inverse mapping. More specifically, for the group-averaged data, we acquired better fits when starting from W_{fMRI} than from W_{MEG} (see Figures 7 and 8). Similar to the mapping from structural to functional networks, the estimated coefficients were significantly different under the 5% significance level for the two modalities for the group-averaged data pointing towards a modality-dependent mapping (see SI Figure 5.16, 95% confidence intervals did not overlap). An overview of the estimated coefficients for this data set is given in SI Table 5.3. Furthermore, similar to the mapping f, no significant improvement of the goodness of fit level was found by including terms of a higher order than 5 for $f^{-1} : W_{MEG} \to A$. Even including W_{fMRI} in the mapping $f^{-1} : W_{fMRI} \to A$ hardly improved the fit (no significant improvement under the 5% significance level). Applying the same approach for the individual data, we were able to reach a lower overall error, thus a better fit, for f^{-1} than for f and the differences in modalities with respect to the residuals were very small for f^{-1} (see Figure 5.4c).

To have a benchmark for the overall residuals, we again repeated the same analysis with reshuffled matrices. Similar to f, the function f^{-1} outperformed the random reshuffles for group-averaged networks (see Figure 5.4b, p-value of 0% for MWW-test). On the subject level, the function f^{-1} obtained significantly better results for the empirical matrices than their random reshuffles for most of the individuals under the 5% significance level (two outliers for the p-values of the MWW-test for $f^{-1} : W_{fMRI} \to A$, see Table 5.1 and Figure 5.4c). Again, the same analysis using the second group-averaged data set for MEG revealed only for the estimated coefficients $c_1[f]$ and $c_2[f]$ from Eq. (5.5) significant differences between the first and the second data set (for $K = 5$, Figures 5.5a and 5.5b). For fMRI, a significant difference could only be determined for $c_1[f]$ but not for the other estimated coefficients from Eq. (5.5), which again cross-validates our mapping between different data sets.

Moreover, the whole analysis was repeated multiple times to check for the stability of the estimated coefficients, which resulted in exactly the same coefficients every time, underlining the robustness of our results. We also analyzed in more detail which connections were well predicted by our approach and which were estimated less accurately (see SI Figures 5.21 - 5.28). A corresponding analysis in the spectral domain (see SI Section 5.6.2 for the results) illustrated that the estimated coefficient values were similar to those in the topology domain for the function f but not for f^{-1} (see SI Figures 5.11 - 5.14). The dissimilarities between the spectral and topology domain are most probably due to eigenvector perturbations between the different analyzed empirical matrices. These eigenvector perturbations can probably be traced back to noisy measurements (see SI 5.6.6).

5.4. DISCUSSION

In this study, we have analyzed the mutual dependency of structural and (resting-state) functional networks in a multimodal framework by assuming that there exists a mathematical function that allows for a mapping between the two networks. This function was then analyzed without assuming a priori any specifics and by estimating the coefficients for the mappings in both directions (i.e. structural to functional and functional to structural networks). Our analysis convincingly implicated that our assumption of a mapping between the two networks was justified because we reached overall good fits outperforming random reshuffles and

(a) Visualization of fitted vs. empirical matrices.

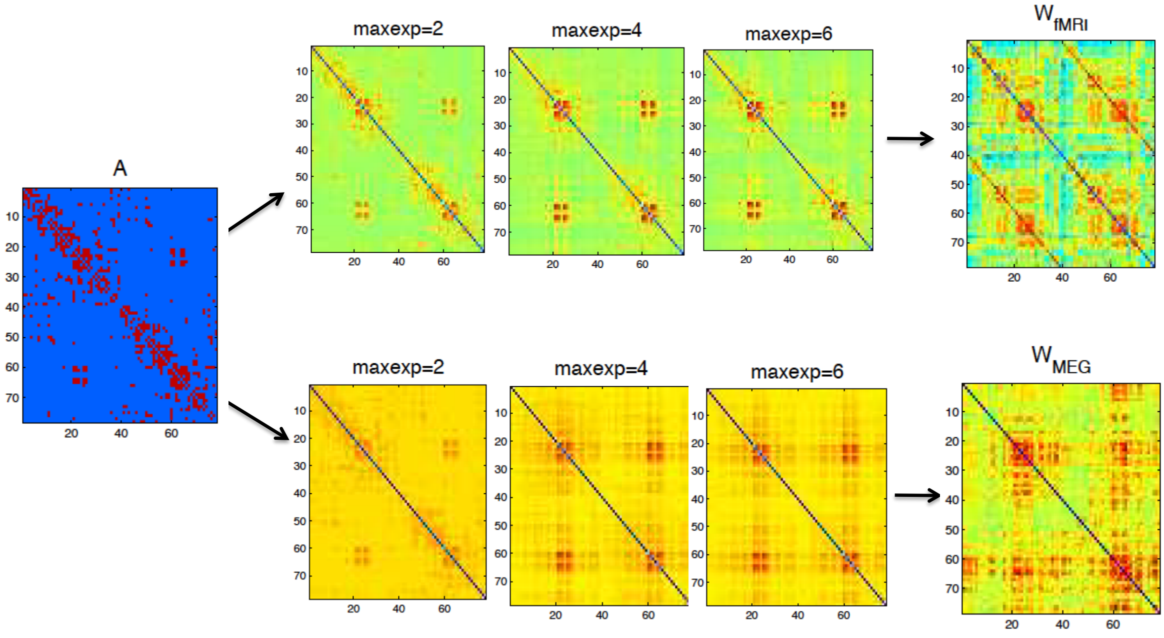

(b) SSE_{norm} for group-averaged data.

(c) SSE_{norm} for individual data.

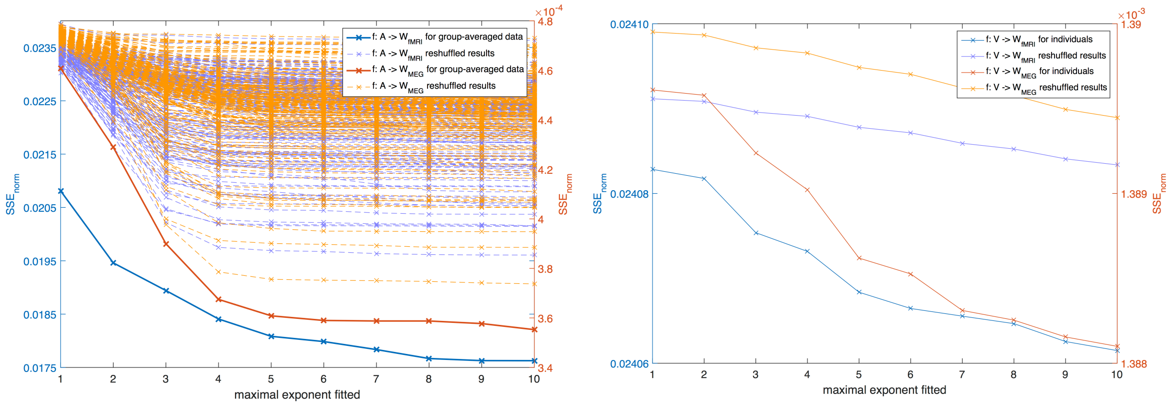

Figure 5.2: (a) Visualization of the fitted matrices for different maximal fitted exponents K (abbreviation: *maxexp*) for the function $f : A \to W_{fMRI}$ and $f : A \to W_{MEG}$ vs. the empirical matrices for the group-averaged data set. (b) SSE_{norm} for the group-averaged data set for different maximally fitted exponents K displayed together with the results of the reshuffled matrices. For each mapping we ran the same analysis with 100 reshuffled versions of the matrix A and with 100 reshuffled versions of matrix W. (c) SSE_{norm} for the individual data set for different maximally fitted exponents K (after averaging over all 11 individual SSE_{norm} results) displayed together with the averaged result of the reshuffled matrices. For each mapping we ran the same analysis with 100 reshuffled versions of the matrix V and with 100 reshuffled versions of matrix W.

(a) $f : A \rightarrow W_{MEG}$.

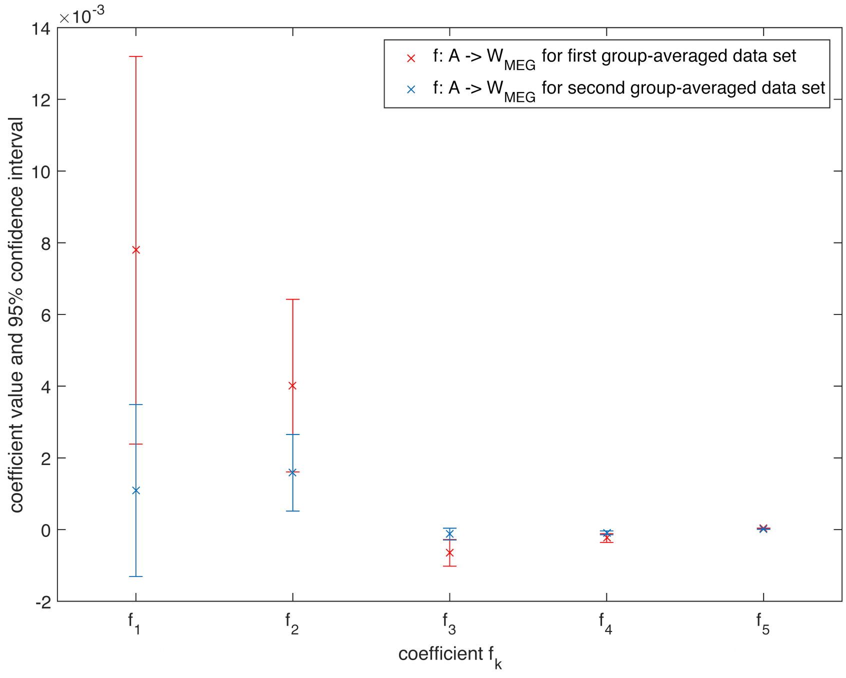

(b) $f : A \rightarrow W_{fMRI}$.

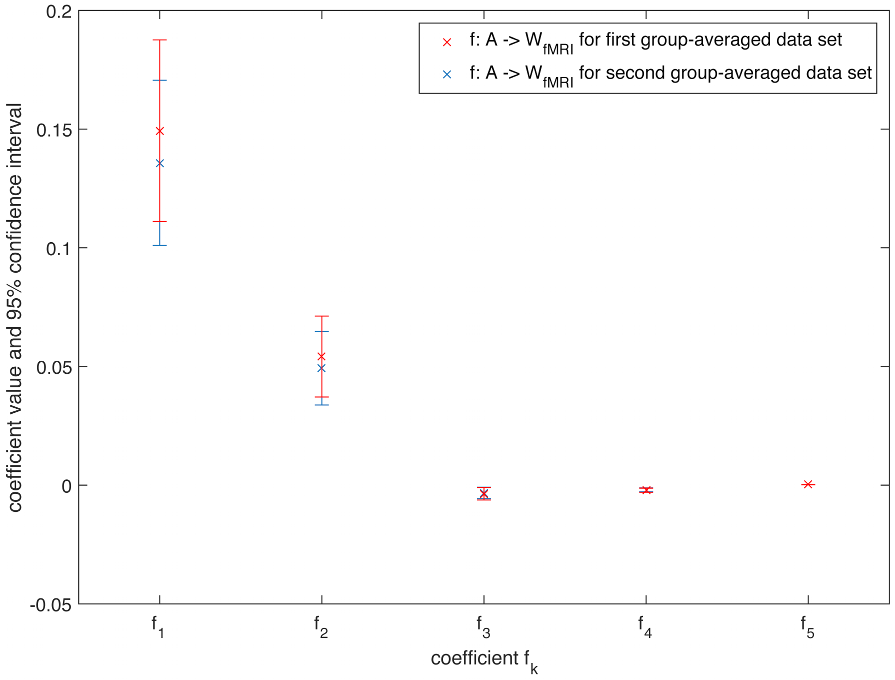

Figure 5.3: (a) Estimated coefficients for the mapping $f : A \rightarrow W_{MEG}$ for $K = 5$ together with their 95% confidence interval for the first group-averaged data set and a second group-averaged data set. (b) Estimated coefficients for the mapping $f : A \rightarrow W_{fMRI}$ for $K = 5$ together with their 95% confidence interval for the first group-averaged data set and a second group-averaged data set.

(a) Visualization of fitted vs. empirical matrices.

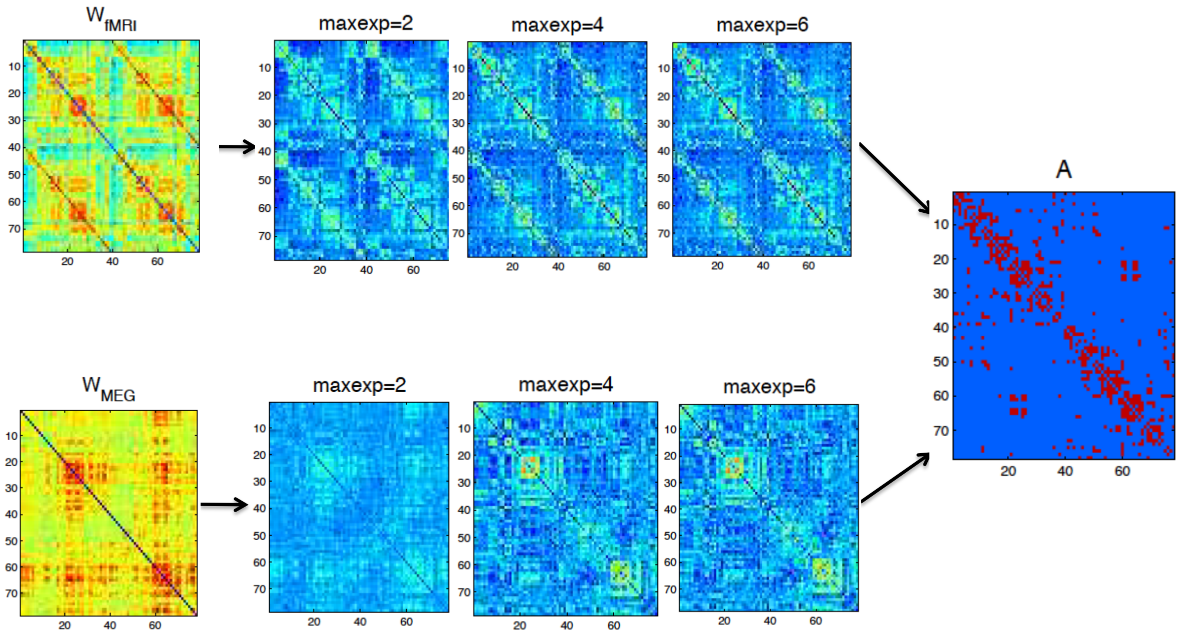

(b) SSE_{norm} for group-averaged data.

(c) SSE_{norm} for individual data.

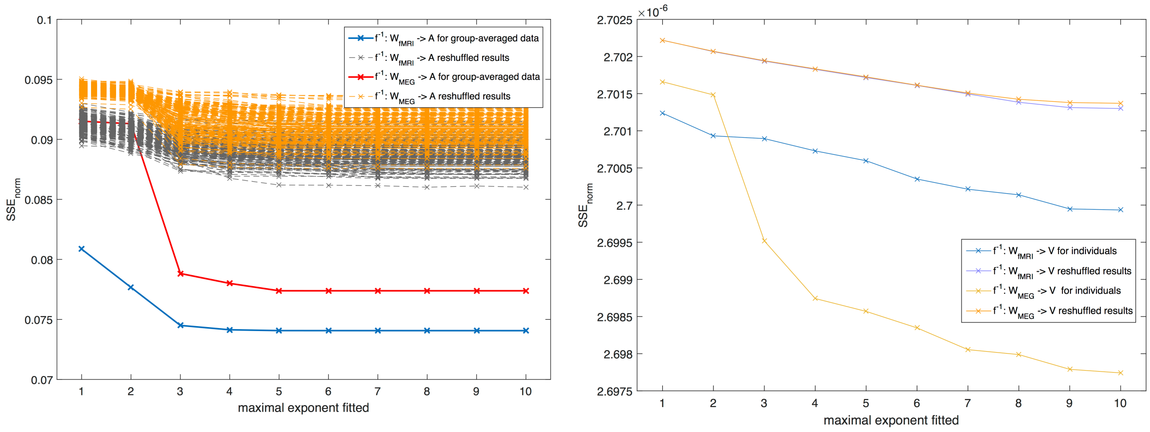

Figure 5.4: (a) Visualization of the fitted matrices for different maximal fitted exponents K (abbreviation: *maxexp*) for the function $f^{-1}: W_{fMRI} \rightarrow A$ and $f^{-1}: W_{MEG} \rightarrow A$ vs. the empirical matrices for the group-averaged data set. (b) SSE_{norm} for the group-averaged data set for different maximally fitted exponents K displayed together with the results of the reshuffled matrices. For each mapping we ran the same analysis with 100 reshuffled versions of the matrix A and with 100 reshuffled versions of matrix W. (c) SSE_{norm} for the individual data set for different maximally fitted exponents K (after averaging over all 11 individual SSE_{norm} results) displayed together with the averaged result of the reshuffled matrices. For each mapping we ran the same analysis with 100 reshuffled versions of the matrix V and with 100 reshuffled versions of matrix W.

(a) $f^{-1}: W_{MEG} \rightarrow A$.

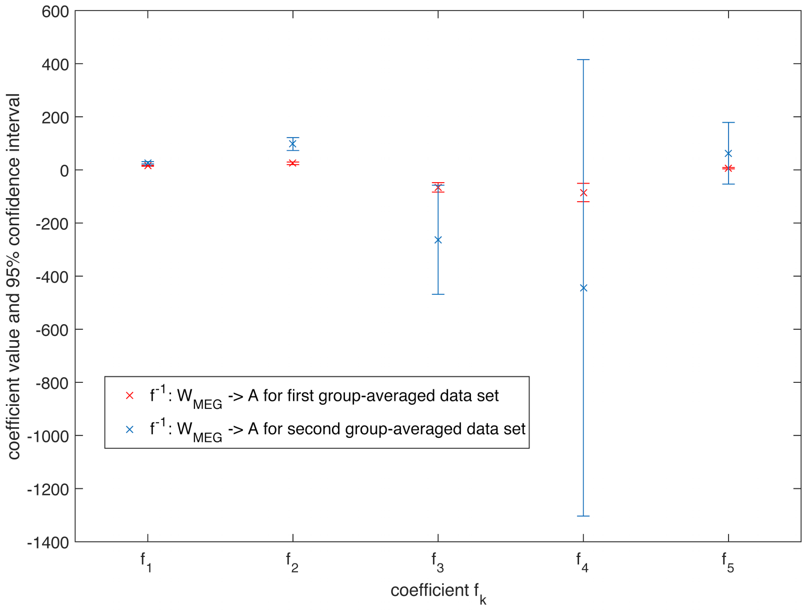

(b) $f^{-1}: W_{fMRI} \rightarrow A$.

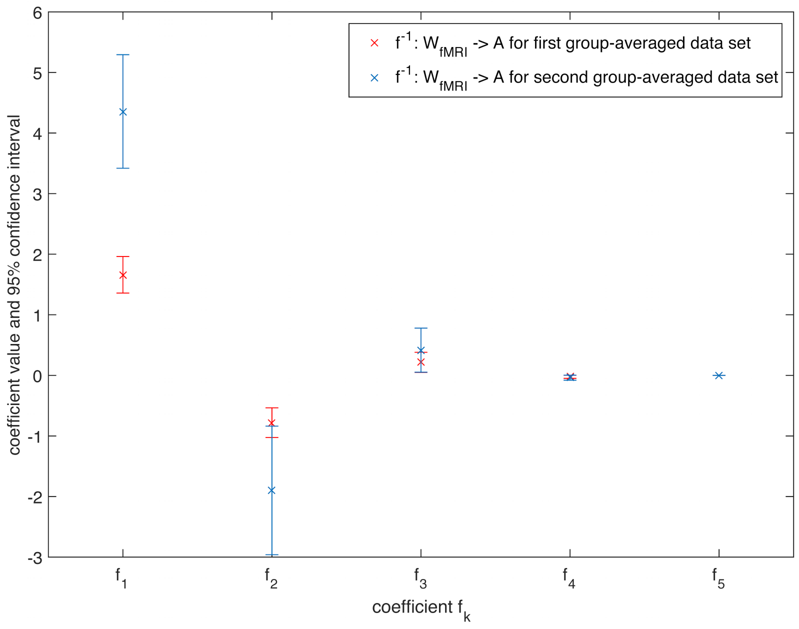

Figure 5.5: (a) Estimated coefficients for the mapping $f^{-1}: W_{MEG} \rightarrow A$ for $K = 5$ together with their 95% confidence interval for the first group-averaged data set and a second group-averaged data set. (b) Estimated coefficients for the mapping $f^{-1}: W_{fMRI} \rightarrow A$ for $K = 5$ together with their 95% confidence interval for the first group-averaged data set and a second group-averaged data set.

Table 5.1: p-values for the comparison between SSE_{norm} for the empirical and reshuffled matrices. The matrix V denotes the structural network matrices for the individual data and the different columns are for the different 11 analyzed persons (*p1* till *p11*). Note that in most cases a significantly better goodness-of-fit was obtained for the empirical matrices than for the reshuffled matrices ($p < .05$, indicated with *).

Mapping	p1	p2	p3	p4	p5	p6	p7	p8	p9	p10	p11
$f^{-1} : W_{fMRI} \rightarrow V$	.887	<.001*	<.001*	<.001*	.002*	.003*	<.001*	.390	<.001*	<.001*	<.001*
$f : V \rightarrow W_{fMRI}$	.001*	<.001*	<.001*	<.001*	.011*	<.001*	<.001*	<.001*	<.001*	<.001*	<.001*
$f^{-1} : W_{MEG} \rightarrow V$	.001*	<.001*	<.001*	<.001*	<.001*	<.001*	<.001*	<.001*	.001*	<.001*	.002*
$f : V \rightarrow W_{MEG}$	.339	<.001*	.018*	<.001*	<.001*	.827	<.001*	.975	.815	<.001*	.130

resulting in similar matrix patterns. However, our results also indicated that the mapping was modality-dependent as the coefficients for mappings with MEG- or fMRI-based networks significantly differed.

The existence of such a mathematical function points towards the fact that the functional connectivity of the brain can be described by a combination of the underlying structural connections. Because of the stability of the estimated coefficients and their cross-validation across different data sets, such a mathematical function could potentially be used to predict structure from function or vice versa in future studies. Also, once we can use this mathematical framework to predict 'healthy' functional connectivity, we can compare the matrix to the actual measured functional network of the patient and identify possible malicious connections indicating disease.

5.4.1. NEUROBIOLOGICAL INTERPRETATION

If we consider the case of a binary structural adjacency matrix, then the matrix element $(A^k)_{ij}$ equals the number of walks of length k between node i and node j. Each term $c_k[f]A^k$ can be considered as the contribution of walks with hopcount k to the functional network (see SI Figure 5.17). Here, hopcount is defined as the number of intermediate links between two nodes in a walk (length of the walk). Our approach confirms the ideas postulated by Robinson and co-workers that a functional connection can be regarded as a sum of all possible walks between two regions [77, 78]. Additionally, our approach returns the coefficients $c_k[f]$, which can be interpreted as the influence of all walks with hopcount k (see SI Table 5.3 and Figure 5.17). In contrast to a path, a walk can traverse the same node more than once. Potential loops in walks are also in line with the belief that re-entry loops can act as a resonating system to enhance a signal that needs to be spread over a long distance [41].

In contrast to most previous studies, we followed a multimodal approach analyzing the mapping for MEG and fMRI data. As opposed to studies that assumed a specific function beforehand, we followed a data-driven approach by fitting coefficients of the general expression (5.5). More precisely, fMRI networks seemed to be shaped by walks of lower hopcount in the structural network since the coefficients were higher for these configurations (see SI Figure 5.15). In contrast, for MEG networks all walks from the underlying structural network up to hopcount 5 appeared to contribute more or less equally to the resulting fitted functional network matrix (see SI Figure 5.15). Overall, we found that estimations from structural networks were more accurate when predicting MEG networks on both individual and group level than when predicting fMRI networks. However, when the functional network was used to predict the structural one, we saw only small differences at the individual level between the modalities but at the group level the fitting using fMRI matrices performed better. These observations together with the significantly different coefficients for MEG and fMRI confirm the modality dependency of the mapping. If ρ denotes the diameter of the network, defined as the hopcount of the longest shortest path in a graph [111], our analysis for both fMRI and MEG suggests that the diameter of the unweighted structural network ($\rho = 6$) is directly related to the number of terms $K = 5$ in Eq. (5.5) that are sufficient for the best fit of the mapping from structural to functional networks. Hence, a functional connection between two regions seems only to be shaped by walks in the structural network that are shorter than the diameter of this structural network. The important role of the diameter in this fitting procedure can also be mathematically justified (see also SI Section 5.6.1).

Besides the possibility of predicting the functional network using the structural network, our analysis also has practical implications on how communication processes shape brain activity. Bullmore and Sporns proposed the hypothesis that the brain is optimized for efficiency and robustness [15]. Our findings seem to be in line with this idea since the brain seems to use not only (structural) shortest paths (most efficient from a network perspective) for communication but is also transmitting information through less efficient paths or walks. Thus, there seems to be some kind of degeneracy in the brain [76]. From a network science perspective, spreading information not only through the shortest path makes the (healthy) brain function more robust against link breakage. However, there seems to be an upper bound for the length of the paths that the brain uses for communication, which corresponds to the diameter of the structural brain network. Walks that are longer than the diameter are highly inefficient for communication. The diameter therefore seems to symbolize the trade-off between efficiency and robustness [15]. It is this degeneracy and robustness that could keep two regions functionally connected when the direct structural connection is damaged in disease. In multiple sclerosis, the structural network gets damaged due to lesions and diffused white matter damage. With this theory we could predict which detours are likely to be taken for functional connections in order to uphold (sub)-optimal network efficiency. Thus, based on the damaged structural network we could be able to make predictions on how this damaged structural network might map onto a functional network. These practical implications seem to agree with several studies that have shown that the averaged path length is higher in diseases than in the healthy brain [89].

Our mathematical approach incorporates previous models on the relationship between structural and functional networks into one single model. For example, a previous study found that the shortest paths and detours along these paths in the structural network were the strongest predictors for functional connections [41]. This result agrees with our finding of the structural-functional network mapping being dependent on the combination of walks with small hopcounts (corresponding to the shortest paths in the network) and detours from these shortest paths. Also the suggestion that network diffusion has the ability to predict functional connections [1] is in line with our work. Network diffusion indicates that information is not merely transmitted through the shortest paths, but also through less efficient paths. Furthermore, our mathematical function also includes the predictive value of common neighbors for functional connections [119]. The term $c_2[f]A^2$ in Eq. (5.5) corresponds to the weighted number of walks between any pair of nodes with hopcount 2, i.e. walks from any node i to a node j via a common neighbor. In a previous study, Tewarie and coworkers [96] demonstrated that the degree product between nodes in the structural network together with the Euclidean distance has the ability to predict the functional connections between these nodes. We observed here that our approach with the sum of structural matrices A^k in Eq. (5.5) is correlated not only with the degree product (SI Figure 5.18) but also with the complete previous model (including Euclidean distance, SI Figure 5.19).

Predicting the structural network from the functional network has received relatively little attention [1, 23, 77, 78]. We assumed that the structural network is a weighted sum of powers of the functional network matrix W. However, unlike the structure-to-function mapping f, the interpretation of this mathematical function is less straightforward: If we define the weight of a walk as the product of all weights along this walk, then the matrix entry $(W^k)_{ij}$ represents the summed weights of all possible walks with hopcount k between node i and node j. Similar to the function f, we find for f^{-1} that higher powers of W do not contribute substantially to the goodness of fit of our mapping. In contrast to the powers of a binary matrix, W^k does not only contain the number of walks with hopcount k but also incorporates information about their weight structure. Still, we can conclude that longer walks in the functional network seem to influence the structural brain network less. Practically, this result not only helps us to reconstruct the structural connections when we have only the functional connectivity matrices, but it also indicates that a direct structural connection between two brain regions seems to be influenced not only by their direct functional connectivity but also by the (functional) communication within a small hopcount neighborhood of those two regions.

Using an additional data set of individual healthy controls (data set (iii)), we found that our mapping can also be generalized to the individual level. For the individual mappings, we also found that nearly all mappings were able to outperform their reshuffled benchmark except for some outliers (see Table 1). Furthermore, we compared the results of the group-averaged data and the individual data (each of these containing data from multiple modalities). In the case of the mapping from structural to functional networks, the performance when using individual fits was similar to that obtained when using the group-averaged matrices (see Figures 5.2b and 5.2c). However, for the inverse mapping, the individual mappings provided a much better fit than the group-averaged mappings. These results could potentially be explained by the following factors: (1) there exists an even stronger relationship between function and structure at the individual level, (2) the use of weighted structural connectivity matrices (instead of the binary group-averaged structural connectivity matrix), which are more representative of the underlying fiber bundle structure or (3) the fact that the structural and functional information were gathered from the same group for data set (ii) (in contrast, the group-averaged structural and functional connectivity matrices were based on two different sets of healthy controls).

5.4.2. TECHNICAL IMPLICATIONS

Our approach may provide important information about the DTI-obtained structural network that is generally missed due to methodological issues with crossing versus kissing fibers which usually affect inter-hemispheric connections. Given the functional networks, a mapping to the structural network could also allow to distinguish between genuine and false positive connections, which are inherently present in DTI data [100]. For example, in the structural networks estimated from MEG and fMRI networks we observed more homologous inter-hemispheric connections than in the actual empirical structural network (see the off-diagonal in SI Figure 5.8). In addition, for MEG functional connectivity metrics, there are well known methodological issues with volume conduction, signal leakage and field spread. By using our approach and trying out different functional connectivity metrics, one could aim to find the common properties of these mappings, i.e. those that are invariant of the functional metric that was used.

5.4.3. METHODOLOGICAL CONSIDERATIONS

Firstly, we investigated the relationship between the structural network and static patterns of (resting-state) functional connectivity, as functional connectivity was estimated over epochs of several seconds. Therefore, our approach does not consider the dynamical aspects of functional connectivity. It is well known that functional networks obtained from smaller time windows correspond less to the structural network [52, 66, 102] and therefore our approach could be less applicable to these smaller time scales.

Secondly, the mapping employed in this study can certainly be influenced by the choice of the parcellation of brain regions. However, as long as the ratio between genuine (functional or structural) connections and noise in the matrices remains similar between parcellation atlases, we do not expect it to have a significant impact on the goodness of fit of our mapping. Despite the well-known limitations of the AAL atlas, it still provides a commonly used framework in neuroimaging studies. By using it, the results from our study are directly relevant for this existing body of work. We also provided a suggestion of how to overcome the dimension differences of the matrices of different parcellations mathematically in SI Section 5.6.9.

Thirdly, our mapping can be influenced by noise in the matrices, such as the presence of false positives in the structural connectivity matrix. However, by randomly adding some connections on top of the existing connections to the structural network and redoing the analysis, we observed that the fluctuation in goodness of fit was relatively small (see SI Figure 5.20).

Fourthly, we have chosen the *alpha2* band because of high SNR for this frequency band. The mapping between structure and function may be different in terms of coefficients for the other frequency bands because we face there to some extent a different structure in the matrices. To explore the mapping for different frequency bands is a goal for future studies. Since the PLI probably underestimates the connectivity strengths [91], future research should apply our methods on other connectivity measures as well which will probably lead to different mappings in terms of different coefficients. Previous studies have used the amplitude envelope correlation to study MEG/fMRI similarity [12]. This metric may be used in future studies to analyze structural versus functional network mappings but this is beyond the scope of the present study.

5.5. CONCLUSION

In the present study, we have demonstrated that, irrespective of the functional imaging modality, the relationship between structural and functional networks can be described by a mapping. Such a mathematical function can predict resting-state functional networks from the structural network and vice-versa. This mathematical function can be described by a weighted sum of matrix powers which represent in the binary case the number of walks up to a certain hopcount in the network. Thus, according to our analysis, a functional connection seems to be shaped by shorter walks up to the diameter in the underlying structural network. This result provides a general framework that incorporates previously published models on the relationship between structural and (stationary) functional networks. Also when analyzing the mapping from functional to structural networks, longer walks in the functional brain network appear not to have a big influence on the structural connections. We found different coefficients for MEG and fMRI for our mapping, which point towards a modality dependency for the structure-function relationship. Furthermore, this mathematical function could help to reduce noise and artifacts for the empirical estimation of structural and functional networks. We were also able to extend this mapping relationship to the subject level. For future work, differences in individual mappings between patients and healthy controls may provide insights in the disrupted relationship between the structural and functional brain networks in various diseases.

5.6. SUPPLEMENTARY INFORMATION

5.6.1. THEORY

We provide here some mathematical background of our method.

MATRIX FUNCTIONS

If $f(z)$ is a function of the complex number z and analytic in a disk with radius R around z_0, then it can be shown (see Section 2.2) that for all matrices A, the matrix function $f(A)$ can be expressed as a polynomial of degree at most $N-1$,

$$f(A) = \sum_{k=0}^{N-1} c_k[f]\, A^k$$

where the coefficients $c_k[f]$ can be specified as

$$c_k[f] = \frac{1}{k!}\sum_{m=1}^{N} \frac{f(\lambda_m)}{\prod_{j=1;j\neq m}^{n}\left(\lambda_m-\lambda_j\right)}\, \frac{d^k}{dx^k}\prod_{j=1;j\neq m}^{N}\left(x-\lambda_j\right)\Bigg|_{x=0}$$

Only if f is a polynomial of degree m at most $N-1$, we find, for all $0 \le k \le N-1$, that

$$f_k(0) = c_k[f],$$

where $f_k(0)$ is the k-th coefficient of the Taylor series of f for the development point $z_0 = 0$.

ROLE OF THE DIAMETER

An explanation for the importance of the diameter could be as follows: The matrix powers $I, A, A^2, A^3, \ldots$ are all linearly independent of each other up to A^{ρ} [111]. For higher powers, we cannot be sure of their dependency. Our analysis shows that using higher powers of the structural connectivity matrix than its diameter ($\rho = 6$) does not improve the goodness of fit of our estimation. Furthermore, in the binary matrix A, the sum $\sum_{k=1}^{m} A^k$ can have zero entries for all $m < \rho$. Reducing the number of zero entries can also be a reason why the goodness of fit increases gradually until adding A^{ρ} and then converges.

ANALYSIS IN THE SPECTRAL DOMAIN

If a mapping postulated in the previous section is valid, then such a mapping should also hold in the spectral domain [111]. Provided A is symmetric such that $A = X\Lambda X^T$, where the matrix X contains the eigenvectors of A in the columns and $\Lambda = \mathrm{diag}(\lambda_k)$, $1 \le k \le N$, with $\lambda_1 \ge \lambda_2 \ge \ldots \ge \lambda_N$ the real eigenvalues of A, then there exists an alternative to compute $f(A)$. Since eigenvectors are orthogonal, the matrix X is an orthogonal matrix satisfying $X^T X = I$ and $XX^T = I$, where the latter follows from the fact that $X^{-1} = X^T$ and the fact that a matrix and its inverse commute. We assume here that all eigenvalues are different, as is the case in most real-world networks [111]. Then,

$$f(A) = X f(\Lambda) X^T = \sum_{k=0}^{N} f(\lambda_k)\, x_k x_k^T \tag{5.8}$$

where x_k is the eigenvector of A belonging to the eigenvalue λ_k. Using the spectral form (5.8) in our assumption Eq. (5.1) reveals that

$$W = X f(\Lambda) X^T, \tag{5.9}$$

Since W is symmetric, the spectral decomposition equals

$$W = Y \Upsilon Y^T \tag{5.10}$$

where Y is the orthogonal matrix containing the eigenvectors $y_1, y_2, \ldots, y_N$ belonging to the eigenvalues $\mu_1 \ge \mu_2 \ge \ldots \ge \mu_N$ and $\Upsilon = \mathrm{diag}\left(\mu_k\right), 1 \le k \le N$ is the diagonal matrix of the eigenvalues of W. Using the properties of orthogonal matrices, we find from (5.9) the diagonal matrix $f(\Lambda) = \mathrm{diag}\left(f(\lambda_k)\right)$ as

$$f(\Lambda) = X^T W X.$$

With (5.10), we obtain

$$f(\Lambda) = \left(X^T Y\right) \Upsilon \left(Y^T X\right). \tag{5.11}$$

Since both $f(\Lambda)$ and Υ are diagonal matrices and $\left(X^T Y\right) = \left(Y^T X\right)^{-1}$, there must hold that

$$f(\lambda_k) = \mu_k \tag{5.12}$$

for each $1 \leq k \leq N$. Furthermore, from Eq. (5.11) follows that

$$\left(Y^T X\right) f(\Lambda) = \Upsilon \left(Y^T X\right). \tag{5.13}$$

From Eq. (5.12) and the fact that we multiply the matrix $Y^T X$ with the same diagonal matrix from both sides, we can conclude that (under the condition that all eigenvalues are different) $Y^T X = I$ and therefore $X = Y$.

In summary, Eq.(5.1) implies that both the structural matrix A and the functional matrix W must have the same eigenvectors and that the function f maps the eigenvalues (ordered) of A onto those of W (also ordered, see (5.12)). Moreover, (5.12) shows that $f(x)$ is non-decreasing in x.

If the empirical matrices have different eigenvectors, then that difference may be due to noise of the measurement. If the difference cannot be explained by noise perturbation, our assumption in Eq. (5.1) that there exists an analytic function f needs to be revisited and a more general form of our fitting function can be considered with matrix coefficients instead of scalar ones

$$F(A) = \sum_{k=0}^{\infty} F_k (A - z_0 I)^k \tag{5.14}$$

where F_k are $N \times N$ matrices, which reduces when $N = 1$ again to our previous assumption (5.3).

5.6.2. DATA ANALYSIS

VISUALIZATION OF BEST FITS

In Figures 5.6, 5.7 and 5.8, we visualized the best fitted matrices of the group-averaged data set on a bigger scale to better localize the biggest discrepancies between our best fits and the empirical findings. The numbers on the axes of the matrices, 1 to 78 refer to specific brain regions. You can find in Table 5.2 a complete list of the regions of interest (ROIs) that we display mostly with numbers.

We can see that the patterns of the fitted matrices seem to be similar to the empirical ones and that the value range is overlapping. Therefore, we can conclude that also only from visual inspections of the fitted matrices our mapping seems to be convincingly accurate.

SPECTRAL DATA ANALYSIS

After plotting the eigenvalue couples $\left(\lambda_k, \mu_k\right)$ in a scatter plot, we can obtain the function f in the spectral domain (see Eq.(5.12)). Polynomial functions were fitted to all possible combinations of scatter plots (i.e. for the combinations structure-function (MEG/fMRI) and vice versa) by minimizing the sum of squared errors. An example of such a fit is depicted in Figure 5.9.

For the goodness of fit in the spectral domain, we computed the adjusted R^2 value for the different mappings (see Figure 5.10). Overall, we reached already for $K \geq 4$ with all combinations of matrices an adjusted R^2 value of higher than 0.9 indicating a good fit of our mapping. We followed the same approach here as we did for the topology domain, and reversed A and W to repeat the spectral analysis for the function $f^{-1}: W \rightarrow A$. Results of this analysis can also be found in Figure 5.10. For this spectral approach, the adjusted R^2 value did not improve much after adding the same number of terms as was used for the mathematical function in the topology domain (compare Figures 5.10 with Figure 5.2b). Thus, a functional expression with $K = 5$ was again sufficient for the analyzed mappings. This conclusion held for both modalities (fMRI and MEG) and for both functions $f: A \rightarrow W$ and $f^{-1}: W \rightarrow A$.

Since we conducted a similar analysis in the topology and in the spectral domain respectively for the functions f and f^{-1}, we compared the estimated coefficient values for the spectral and topology domain. For a correct comparison, we must omit the error matrix E in Eq. (5.5) in the topology domain. A plot of the estimated coefficient values and confidence intervals (obtained by the least squared parameter estimation in MATLAB) is illustrated in SI Figures 5.11 and 5.12 for the mapping of structural to functional matrices and in SI Figures 5.13 and 5.14 for the other direction. For the mapping f, we only faced small differences between the coefficients (see SI Figures 5.11 and 5.12) and in most cases their confidence intervals were overlapping. But for the other direction, function f^{-1}, we observed quite different estimated coefficients. In the case of $f^{-1}: W_{MEG} \rightarrow A$ we obtained large confidence intervals when many (> 5) coefficients were fitted (see SI Figure 5.13), implying insecure estimations of their exact value. This result is in agreement with the finding that 5

Table 5.2: Complete list of the regions of interest (ROIs) that we mostly display with numbers of the AAL atlas.

1	Rectus-L	40	Rectus-R
2	Olfactory-L	41	Olfactory-R
3	Frontal-Sup-Orb-L	42	Frontal-Sup-Orb-R
4	Frontal-Med-Orb-L	43	Frontal-Med-Orb-R
5	Frontal-Mid-Orb-L	44	Frontal-Mid-Orb-R
6	Frontal-Inf-Orb-L	45	Frontal-Inf-Orb-R
7	Frontal-Sup-L	46	Frontal-Sup-R
8	Frontal-Mid-L	47	Frontal-Mid-R
9	Frontal-Inf-Oper-L	48	Frontal-Inf-Oper-R
10	Frontal-Inf-Tri-L	49	Frontal-Inf-Tri-R
11	Frontal-Sup-Medial-L	50	Frontal-Sup-Medial-R
12	Supp-Motor-Area-L	51	Supp-Motor-Area-R
13	Paracentral-Lobule-L	52	Paracentral-Lobule-R
14	Precentral-L	53	Precentral-R
15	Rolandic-Oper-L	54	Rolandic-Oper-R
16	Postcentral-L	55	Postcentral-R
17	Parietal-Sup-L	56	Parietal-Sup-R
18	Parietal-Inf-L	57	Parietal-Inf-R
19	SupraMarginal-L	58	SupraMarginal-R
20	Angular-L	59	Angular-R
21	Precuneus-L	60	Precuneus-R
22	Occipital-Sup-L	61	Occipital-Sup-R
23	Occipital-Mid-L	62	Occipital-Mid-R
24	Occipital-Inf-L	63	Occipital-Inf-R
25	Calcarine-L	64	Calcarine-R
26	Cuneus-L	65	Cuneus-R
27	Lingual-L	66	Lingual-R
28	Fusiform-L	67	Fusiform-R
29	Heschl-L	68	Heschl-R
30	Temporal-Sup-L	69	Temporal-Sup-R
31	Temporal-Mid-L	70	Temporal-Mid-R
32	Temporal-Inf-L	71	Temporal-Inf-R
33	Temporal-Pole-Sup-L	72	Temporal-Pole-Sup-R
34	Temporal-Pole-Mid-L	73	Temporal-Pole-Mid-R
35	ParaHippocampal-L	74	ParaHippocampal-R
36	Cingulum-Ant-L	75	Cingulum-Ant-R
37	Cingulum-Mid-L	76	Cingulum-Mid-R
38	Cingulum-Post-L	77	Cingulum-Post-R
39	Insula-L	78	Insula-R

(a) W_{MEG}

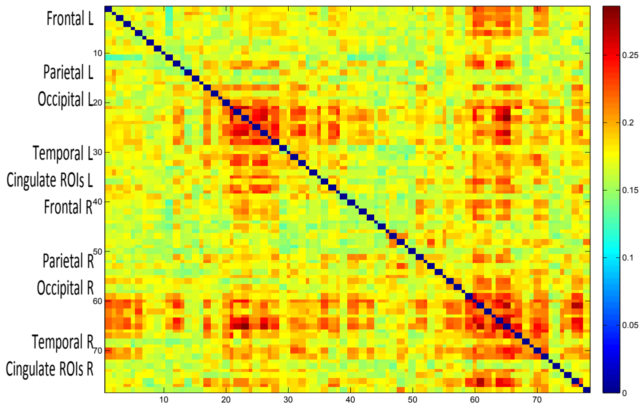

(b) $\widetilde{W}_{MEG}$

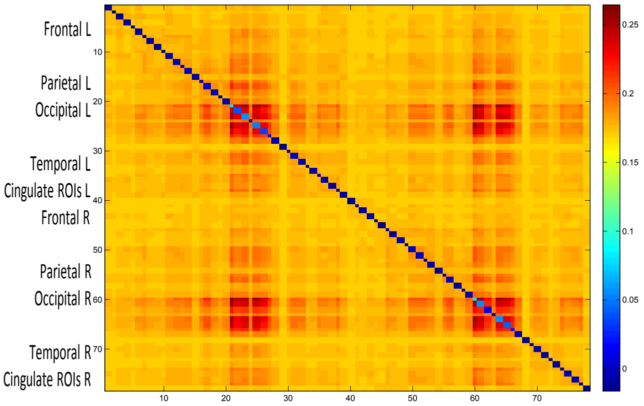

Figure 5.6: Visualization of the best fits for the function f, which was $\widetilde{W}_{MEG}$ (for $K = 6$ with an error matrix E), under the empirical adjacency matrix W_{MEG} for the group-averaged data set.

(a) W_{fMRI}

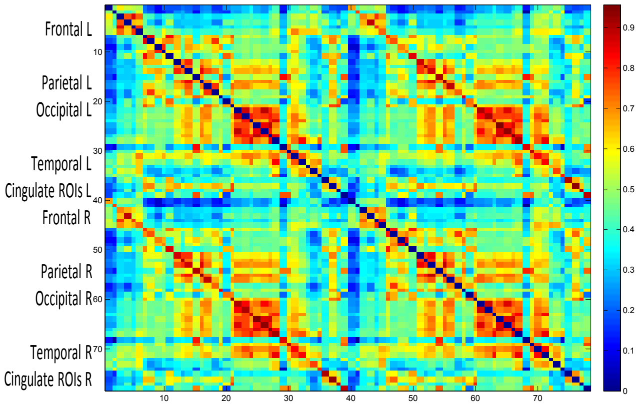

(b) $\widetilde{W}_{fMRI}$

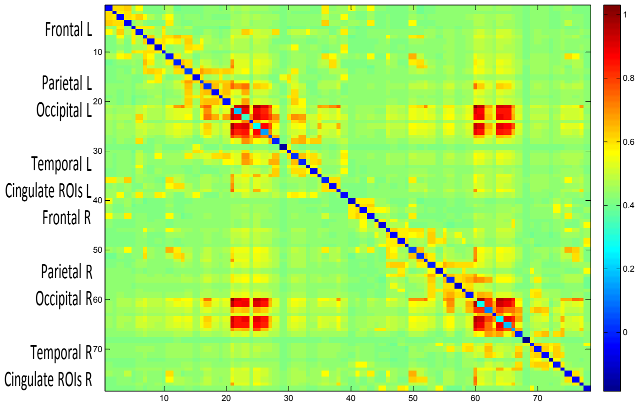

Figure 5.7: Visualization of the best fits for the function f, which was $\widetilde{W}_{fMRI}$ (for $K = 6$ with an error matrix E), under the empirical adjacency matrix W_{fMRI} for the group-averaged data set.

(a) A

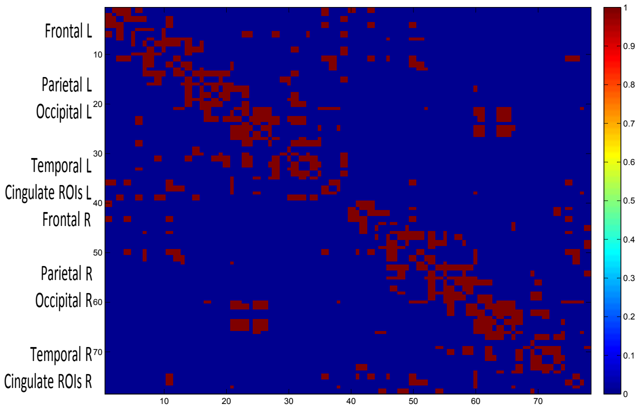

(b) $\widetilde{A}$

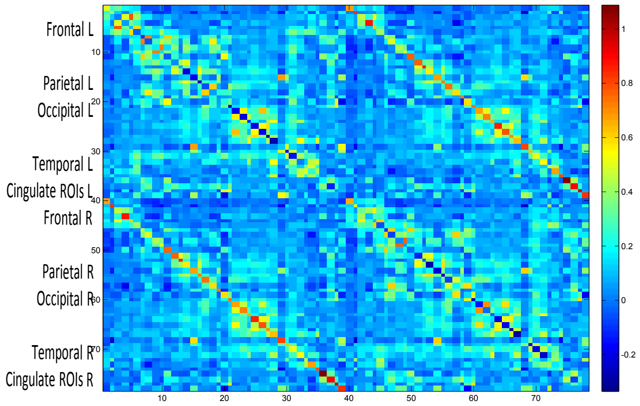

Figure 5.8: Visualization of the best fits for the function f^{-1}, which was $\widetilde{A}$ (again for $K = 6$ with an error matrix E) under the empirical adjacency matrix A for the group-averaged data set.

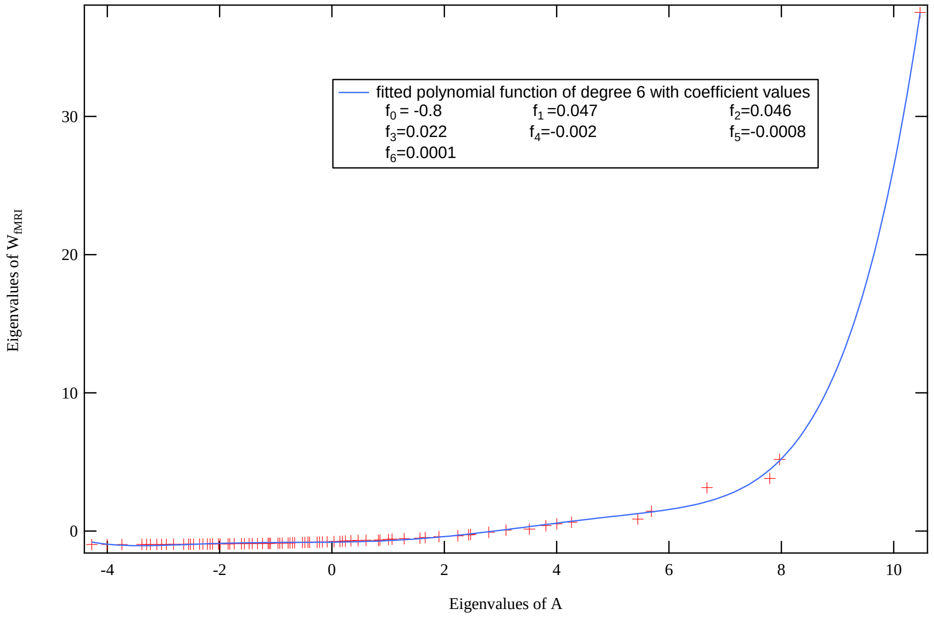

Figure 5.9: Scatter plot of the eigenvalues of the structural matrix A against the eigenvalues of W_{fMRI} with a least-squared fitted polynomial function with a maximal fitted exponent of $K = 6$ (including the intercept f_0) for the group-averaged data set.

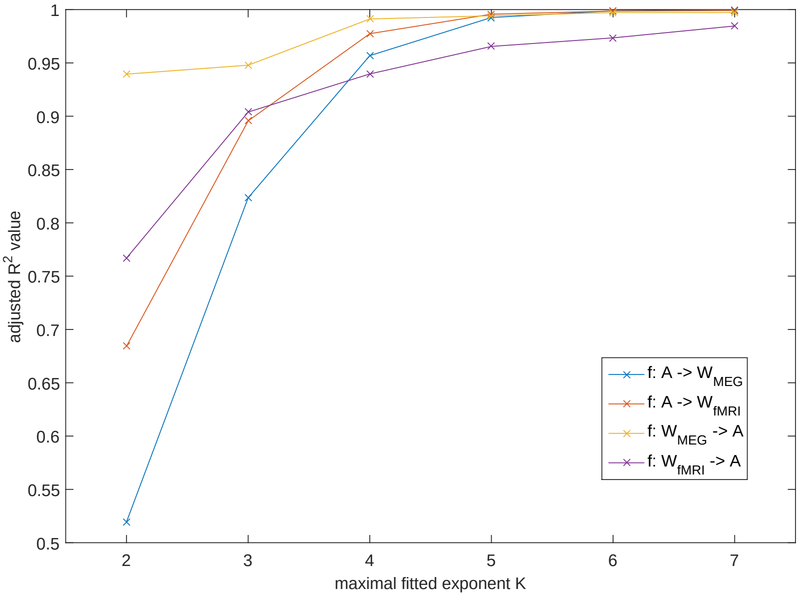

Figure 5.10: Adjusted R^2 value of the different mappings in the spectral domain for different maximal fitted exponents K for the group-averaged data set for $z_0 = 0$.

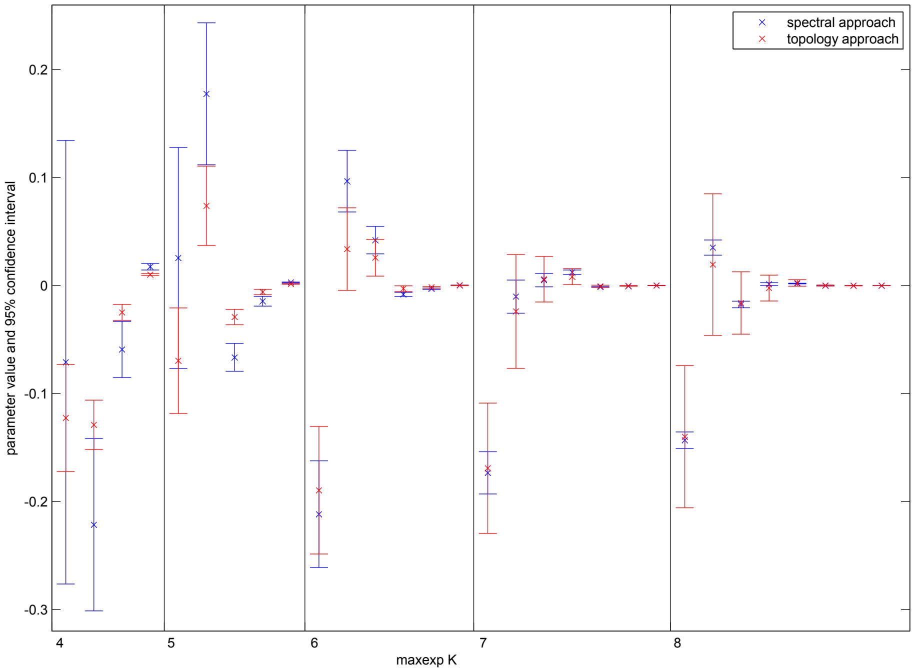

Figure 5.11: Plot of the estimated coefficient values for different maximal exponents K with their 95% confidence interval as an errorbar for the mapping $f : A \rightarrow W_{MEG}$ for the group-averaged data set. The spectral and topology approach are marked in blue and red, respectively. Note that, the confidence intervals of the coefficient values overlap and the distance between the estimated coefficient values is becoming smaller when more coefficients are used.

coefficients were sufficient to describe the mapping between W and A (Figure 5.2b), and that these extra coefficients did not contribute relevant information to the mapping. The discrepancies between the estimated coefficient values in the topology and spectral domain could be originating from the different eigenvectors of the 3 analyzed empirical matrices. These eigenvector perturbations can potentially be caused by noise in the different measurement techniques.

5.6.3. COMPARISON OF FITTED COEFFICIENT VALUES FOR DIFFERENT MODALITIES

In Table 5.3, we displayed the different estimated values for the coefficients of our mapping for a maximal fitted exponent of $K = 6$ and $z_0 = 0$ for the group-averaged data set. In addition, in Figures 5.15 and 5.16 we show the different coefficient values (without the offset estimates) for the two modalities for both mappings together with their 95% confidence intervals, from structure to function and from function to structure. In both displayed figures, the 95% confidence intervals for the estimated coefficients of the different modalities do not overlap indicating significantly different coefficients using the 5% significance level. This table and these confidence intervals show clearly the differences between the different analyzed mappings pointing towards a modality-dependent mapping.

5.6.4. INTERPRETATION WITH WALKS

In Figure 5.17, we visualized our mapping in terms of the number of walks of the structural brain network (without the error matrix E).

5.6.5. COMPARISON WITH A PREVIOUS STUDY

In Figures 5.18 and 5.19, we compare our results with a previous study [96]. Tewarie and coworkers [96] demonstrated that the degree product between nodes in the structural network together with the Euclidean distance has the ability to predict the functional connections between these nodes. If we merely focus on the degree product, we observe that our approach with the sum of structural matrices A^k (see Eq. (5.5)) is correlated with the degree product (SI Figure 5.18). The correlation between those two measures is indeed positive with a Spearman correlation of $R = 0.57$ (p-value < 0.001). There are two clouds in the scatterplot: the upper cloud corresponds to direct connections whereas the lower cloud corresponds to all possible indirect connections, consisting of all walks larger than one. If we investigate the relationship between the previous

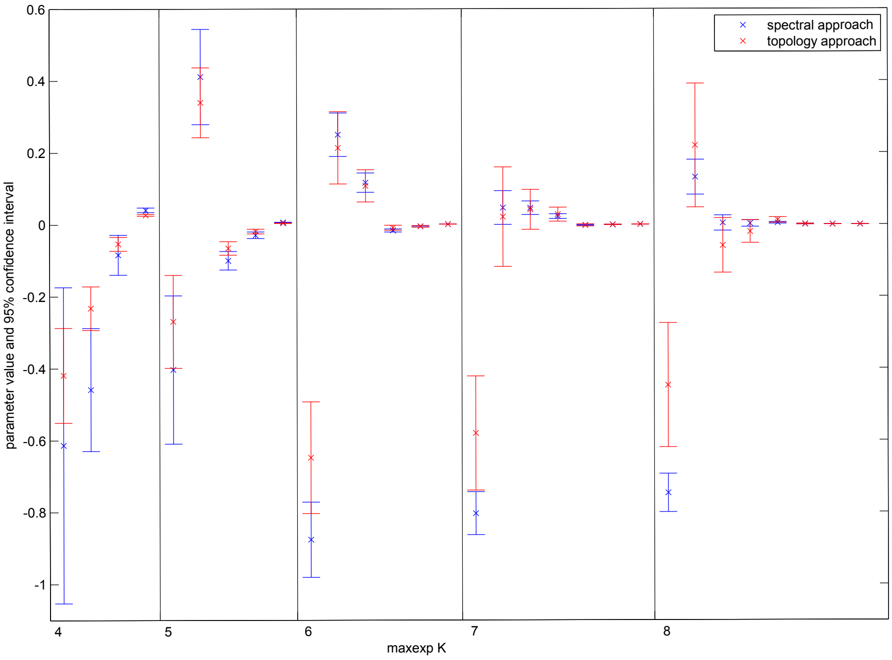

Figure 5.12: Plot of the estimated coefficient values for different maximal exponents K with their 95% confidence interval as an errorbar for the mapping $f : A \to W_{fMRI}$ for the group-averaged data set. The spectral and topology approach are marked in blue and red, respectively. Note that, in nearly all cases, the confidence intervals of the coefficient values overlap pointing towards similar estimated coefficients for the spectral and topology domain.

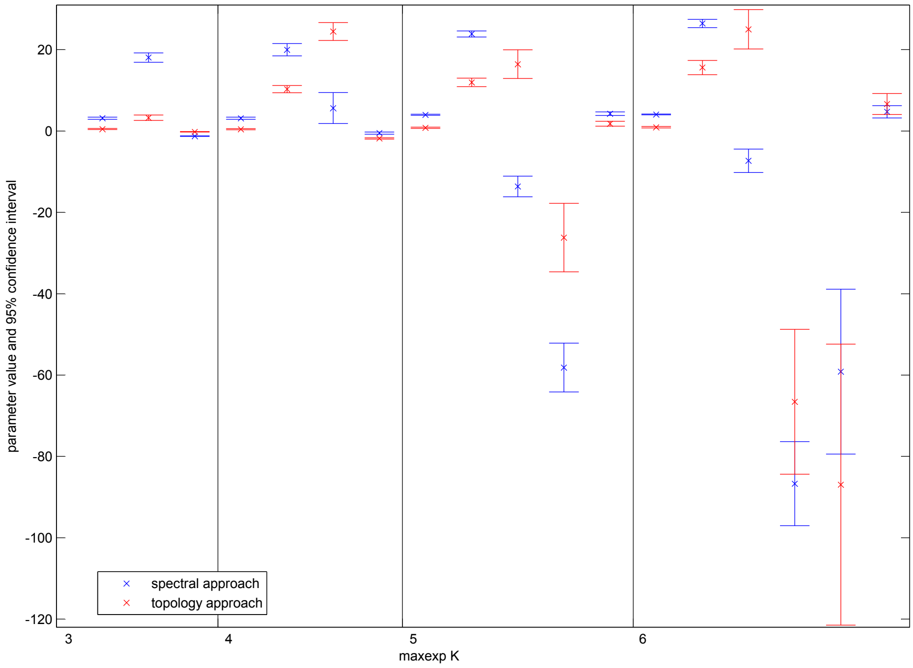

Figure 5.13: Plot of the estimated coefficient values for different maximal exponents K with their 95% confidence interval as an errorbar for the mapping $f^{-1} : W_{MEG} \to A$ for the group-averaged data set. The spectral and topology approach are marked in blue and red, respectively.

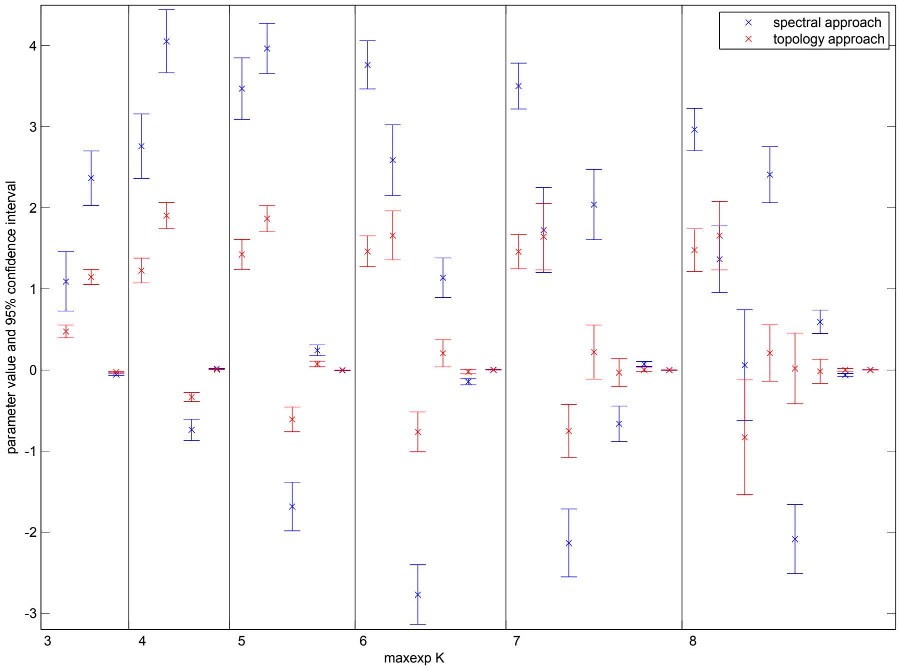

Figure 5.14: Plot of the estimated coefficient values for different maximal exponents K with their 95% confidence interval as an errorbar for the mapping $f^{-1} : W_{fMRI} \rightarrow A$ for the group-averaged data set. The spectral and topology approach are marked in blue and red, respectively.

Table 5.3: Estimated coefficient values for a maximal exponent of $K = 6$ and $z_0 = 0$ for the group-averaged data set.

parameter in front of	f: A -> W_{MEG}	f: A -> W_{fMRI}	parameter in front of	f^{-1}: W_{MEG} -> A	f^{-1}: W_{fMRI} -> A
I	-0.186244926	-0.622088682	I	0.931541504	1.472348531
E	0.170142739	0.417817587	E	-0.226229939	-0.098880043
A	-0.002689163	0.073378816	W	15.61376486	1.633796259
A^2	0.000397359	0.027965465	W^2	25.77141943	-0.760008801
A^3	0.00136165	0.010963972	W^3	-64.46444579	0.241736267
A^4	-7.34E-05	-0.000932557	W^4	-92.90312812	-0.03937664
A^5	-5.42E-05	-0.000401534	W^5	-6.670779246	0.002673357
A^6	5.47E-06	3.96E-05	W^6	0.993949647	-4.75E-05

model (including degree product and Euclidean distance as predictors for functional connectivity) and the mapping approach from this chapter, the Spearman correlation R becomes higher ($R = 0.64$, p-value < 0.001, see Figure 5.19). This result raises the question whether the Euclidean distance as a separate term in a model for explaining functional connections is required [3]. In our approach, we only incorporated topological distance, which means the distance with respect to intermediary nodes and links in the structural network, and not Euclidean distance; however, these findings might suggest that topological distance and Euclidean distance between nodes are related.

5.6.6. ERROR ANALYSIS

The equation Eq. (5.1) assumes that W and A are known exactly. In reality, all types of error mask the true structure so that we actually measure

$$\widetilde{W} = W + \varepsilon_W R_W$$

where R_W is a realization of a random matrix with unit norm and ε_W is the maximum amplitude of the error. Similarly,

$$\widetilde{A} = A + \varepsilon_A R_A$$

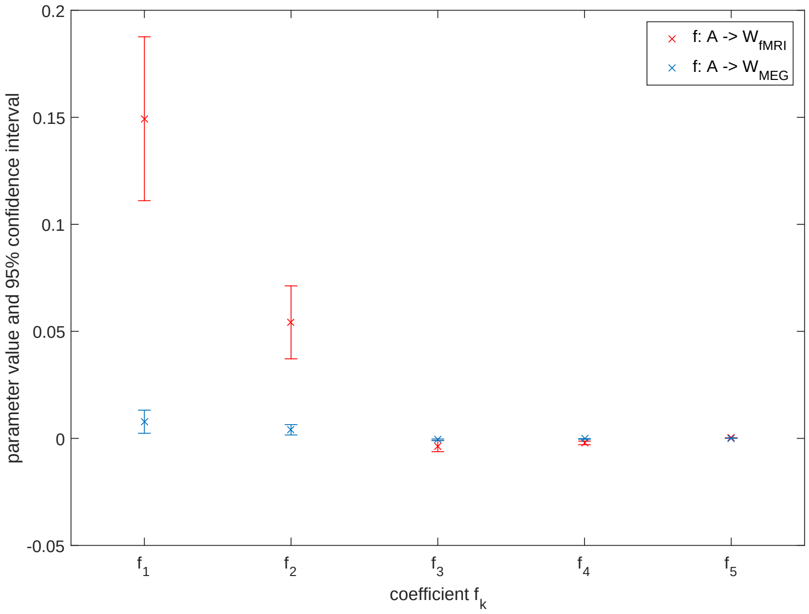

Figure 5.15: Plot of the estimated coefficient values for maximal fitted exponent $K = 5$ with their 95% confidence interval as an errorbar for the mapping from structural to functional networks for the group-averaged data set. Note that the displayed intervals do not overlap, thus we face here significantly different estimated values.

and the assumption becomes

$$\widetilde{W} = f\left(\widetilde{A}\right)$$

or

$$W + \varepsilon_W R_W = f\left(A + \varepsilon_A R_A\right)$$

Using the Taylor expansion (5.3),

$$f\left(A + \varepsilon_A R_A\right) = \sum_{k=0}^{\infty} f_k\left(A\right) \varepsilon_A^k \left(R_A\right)^k$$

up to first order (assuming that ε_A is sufficiently small!), then

$$W + \varepsilon_W R_W = f\left(A\right) + f_1\left(A\right) \varepsilon_A R_A + O\left(\varepsilon_A^2\right)$$

Invoking the assumption (5.1) shows a relation between the different types of errors

$$\varepsilon_W R_W = f_1\left(A\right) \varepsilon_A R_A + O\left(\varepsilon_A^2\right)$$

Given that the assumption (5.1) is correct and that A is known exactly, we could derive a method to improve the measurements $\widetilde{W}$ based on Section SI-5.6.1, which suggests that all eigenvectors of W are fixed and known (i.e. X is the same as for A), so that $\widetilde{W}$ needs to be modified to incorporate this property. This analysis is a suggestion for future work.

To investigate the influence of false positives in the structural matrix, we randomly added connections (1 % new connections) in the structural matrix of the group-averaged data set and redid the analysis (power series in topology domain with 6 terms). The results can be found in the boxplots of the goodness of fit (SSE_{norm}) in SI Figure 5.20. If we define the change in SSE_{norm} due to noise as the noise influence NI whereas $NI(SSE_{norm}) := standard\ deviation(SSE_{norm})/mean(SSE_{norm})$, then we can calculated

$$\begin{aligned}
NI(SSE_{norm})(W_{fMRI} \rightarrow A) &= 0.0174\\
NI(SSE_{norm})(W_{MEG} \rightarrow A) &= 0.0169\\
NI(SSE_{norm})(A \rightarrow W_{fMRI}) &= 0.0124\\
NI(SSE_{norm})(A \rightarrow W_{MEG}) &= 0.0158.
\end{aligned}$$

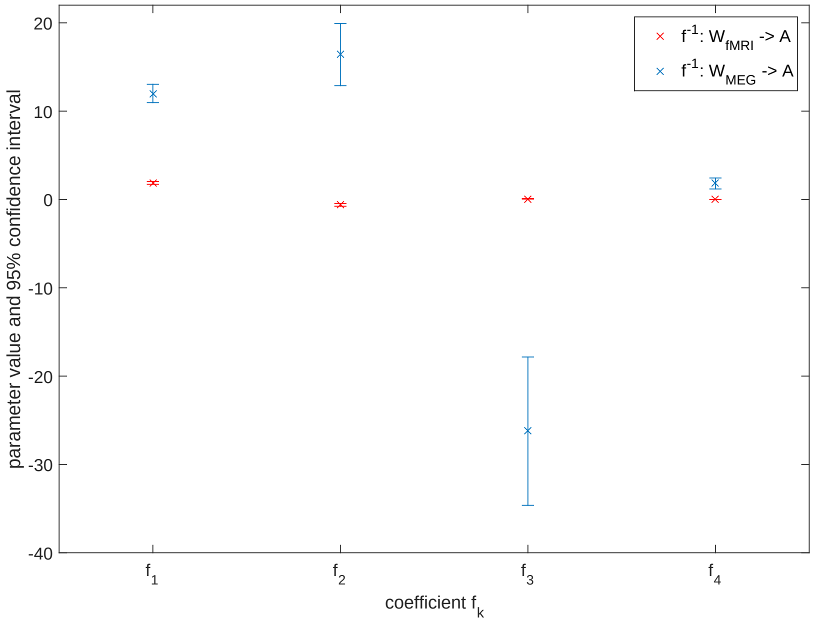

Figure 5.16: Plot of the estimated coefficient values for maximal exponents $K = 4$ with their 95% confidence interval as an errorbar for the mapping from functional to structural networks for the group-averaged data set. Note that the displayed intervals do not overlap, thus we face here significantly different estimated values.

It can be observed from the above that the change in goodness of fit is small in the presence of little noise (in the order of 1%), thus the mapping does not seem to be sensitive to small noise fluctuations.

If we analyze the region-to-region variability, we find that the inter-hemispheric connections were often quite different between the empirical matrix and its fitted version (see the secondary diagonal in Figures 5.21 - 5.24 where we displayed the absolute error). This result confirms our interpretation about the more homologous inter-hemispheric connections in the fitted networks than in the empirically observed networks. Furthermore, we were also interested in which regions benefitted more from an increasing number of coefficients (darker regions in SI Figures 5.25-5.28). Those regions that benefitted from an increasing number of fitted coefficients were possibly most influenced by longer walks in the underlying structural network. For the estimated structural and functional networks by our mapping we observe as a result quite a diverse homogenous spreading of the benefitting regions over the entire group of regions except for the diagonal and secondary diagonal. Thus, we can again conclude that the inter-hemispheric connections are probably benefitting most from our mapping approach.

5.6.7. RESHUFFLED MATRICES

We used one reshuffling technique on all matrices: we selected two matrix entries at random and then exchanged their entries in the matrix (their link weights in the network). We repeated this step 5000 times to obtain a reshuffled version of every matrix, which is again symmetric. Thereby we preserved the distribution of the weights. After generating 100 reshuffled matrices, we compared the goodness of fit distribution of the mappings using reshuffled matrices to our empirical results (see SI Figures 5.29 and 5.30). More precisely, for each mapping from any matrix M to N, we first replaced the underlying matrix M with a reshuffled version of this adjacency matrix and ran the same mapping analysis on it. Then we replaced the image matrix N with a randomly reshuffled version of itself (keeping the underlying matrix M as the original empirical matrix) and ran the fitting algorithm on that combination (thus always one empirical matrix with one reshuffled version of the other matrix together).

For the group-averaged data set, the fit errors of 100 reshuffled matrices were larger compared to those obtained using the experimental data for all analyzed mappings (see SI Figures 5.29 and 5.30). Therefore, we can conclude that the mapping from structure to function (and vice versa) fails when reshuffled connections are used. Therefore, the empirical matrices seem to possess a special structure making the relationship between the structural and functional brain network closer than when reshuffled version of those matrices are used.

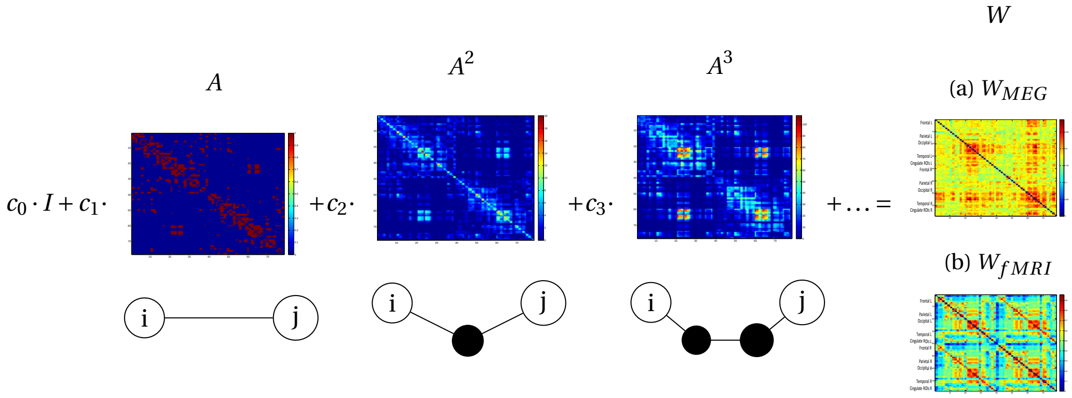

Figure 5.17: Visualization of a simplified version of our model (from Eq. (5.4) where $c_k = c_k[f]$): Walks of different length between node i and j, first the direct connection, then with one intermediate node, with two and so on, adding up to the functional connectivity matrix.

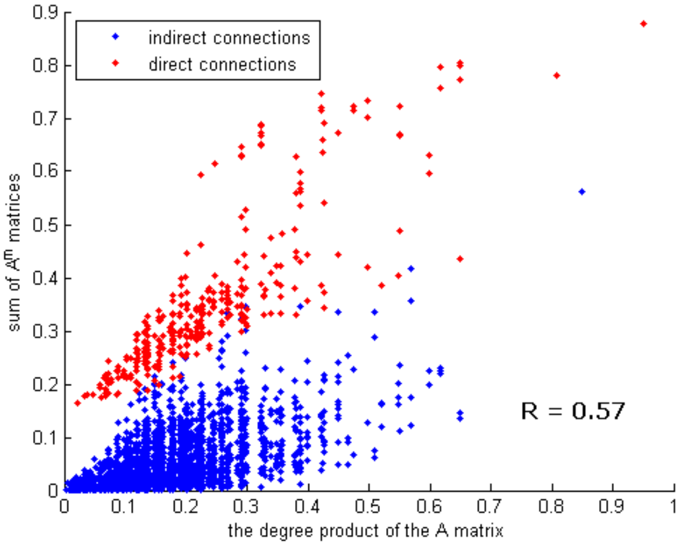

Figure 5.18: Scatter plot of the structural degree product against the sum of the powers of the structural matrix A (from power $k = 1$ up to $k = 6$).

For the data set of individual healthy controls, we also used 100 reshuffled matrices of their structural and functional networks, respectively, and displayed the percentage of those matrices that achieved better goodness of fit than our empirical data (see SI Figures 5.31 and 5.32).

When using 5 coefficients or more, we obtained good results for the mapping $f : V \rightarrow W_{fMRI}$ for nearly all subjects. Only subject number 5 seems to be an exception which could be due to some measurement errors or specific individual attributes of that subject. We also identified two individuals as outliers whose goodness of fit level did not outperform the random reshuffles for the mapping $f^{-1} : W_{fMRI} \rightarrow V$. The function f^{-1} starting from MEG networks obtained good results for $K > 2$. The only mapping that was not able to outperform the reshuffled matrices as a benchmark for most of the subjects was $f : V \rightarrow W_{MEG}$ in the individual healthy control data. To sum up, for the individual structure-function relationships, in most of the cases the mapping performs worse when we apply it to random reshuffles indicating a high goodness of fit level for the mapping between the original empirical matrices.

5.6.8. DETAILS OF THE FITTING PROCEDURE

In order to use the non-linear regression algorithm in MATLAB (using the routine *nlinfit.m* version *R2015a*) to determine the coefficients in Eq. (5.5) by iterative least squares estimation, we need to adapt our data

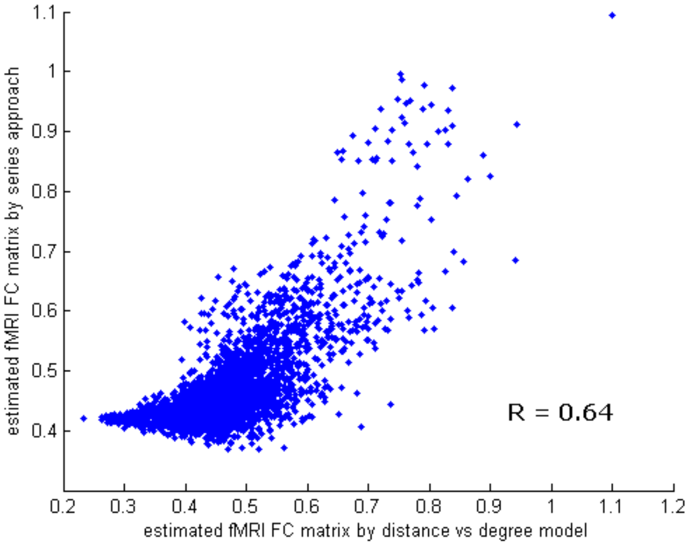

Figure 5.19: Scatter plot of the estimated fMRI correlation matrix from the distance and degree model described in a previous study (Tewarie et al., 2014) against the estimated values using the mapping approach on the structural matrix A.

(a) $f^{-1}: W_{fMRI} \rightarrow A$ and $f^{-1}: W_{MEG} \rightarrow A$

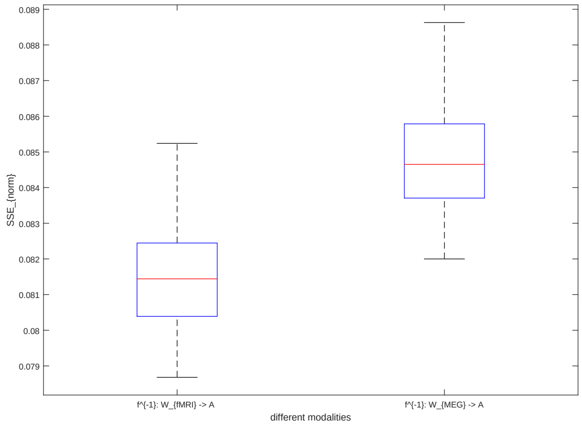

(b) $f: A \rightarrow W_{fMRI}$

(c) $f: A \rightarrow W_{MEG}$

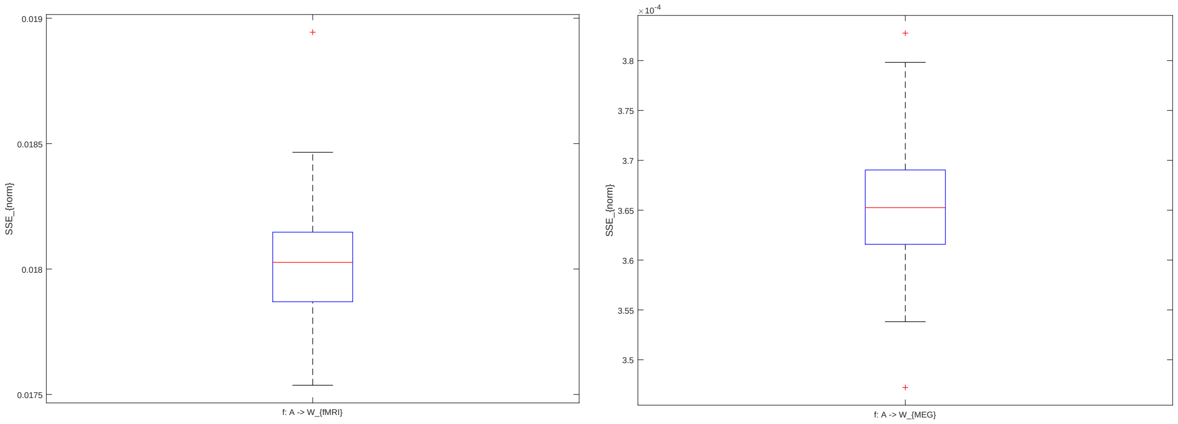

Figure 5.20: Boxplot of the variations in SSE_{norm} in the topology domain for $K = 6$ with group-averaged data for $z_0 = 0$. To investigate the influence of false positives in the structural connectivity matrix, we randomly added connections (1% new connections) in the structural matrix and redid the analysis.

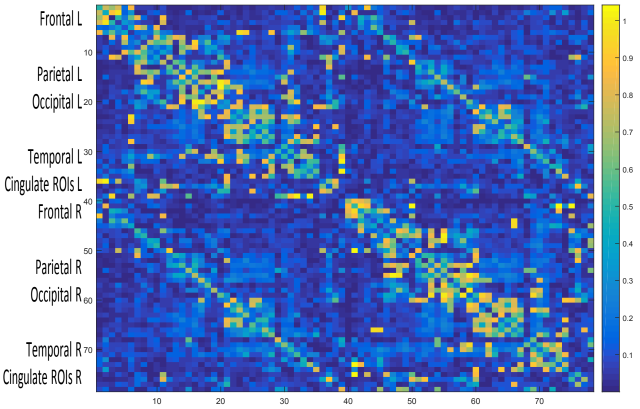

Figure 5.21: Absolute distance matrix between the best fit for $\widetilde{A} = f(W_{fMRI})$ $(K = 6, z_0 = 0)$ and the empirical matrix A for the group-averaged data set.

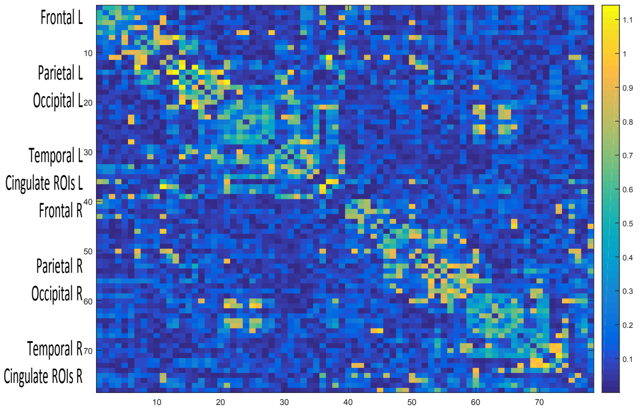

Figure 5.22: Absolute distance matrix between the best fit for $\widetilde{A} = f(W_{MEG})$ $(K = 6, z_0 = 0)$ and the empirical matrix A for the group-averaged data set.

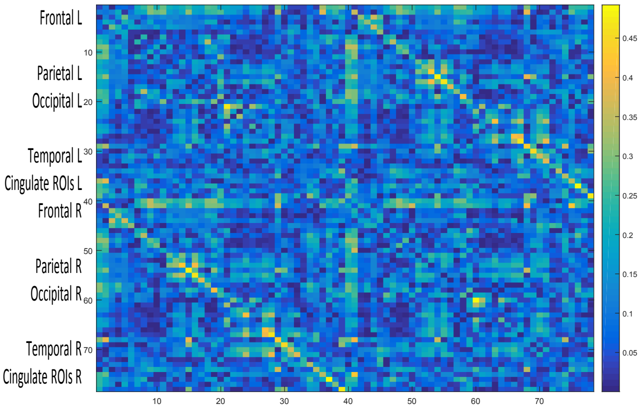

Figure 5.23: Absolute distance matrix between the best fit for $\widetilde{W}_{fMRI} = f(A)$ $(K = 6, z_0 = 0)$ and the empirical matrix W_{fMRI} for the group-averaged data set.

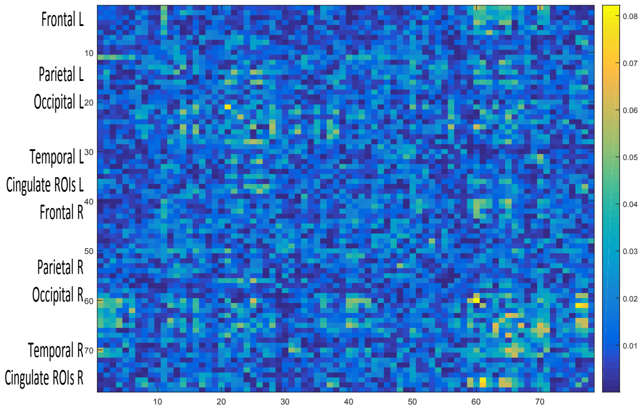

Figure 5.24: Absolute distance matrix between the best fit for $\widetilde{W}_{MEG} = f(A)$ ($K = 6$, $z_0 = 0$) and the empirical matrix W_{MEG} for the group-averaged data set.

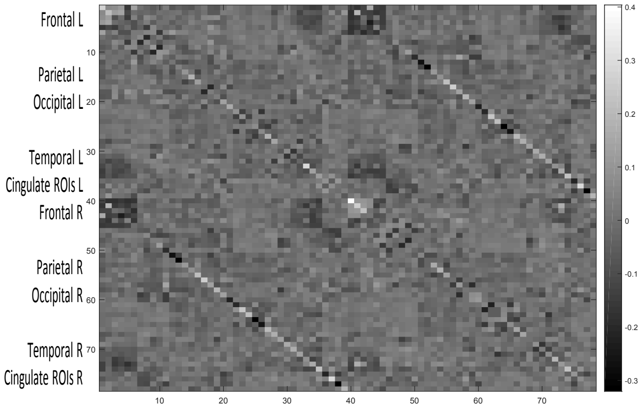

Figure 5.25: Absolute differences in the error for 2 in comparison with the error for 6 fitted coefficients ($K = 6$, $z_0 = 0$) for the mapping $f^{-1} : W_{fMRI} \rightarrow A$ for the group-averaged data set. Note that darker areas correspond here to regions that benefitted more from a higher number of coefficients.

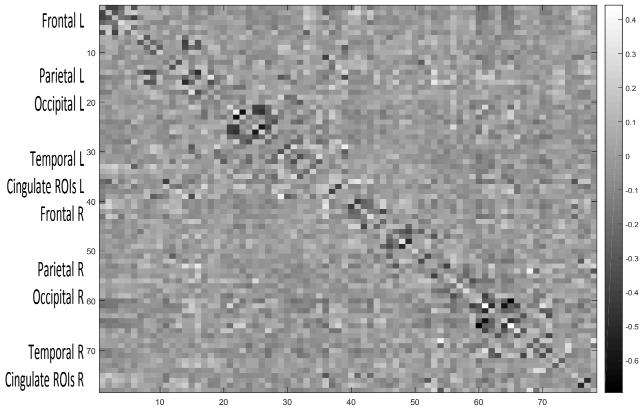

Figure 5.26: Absolute differences in the error for 2 in comparison with the error for 6 fitted coefficients ($K = 6$, $z_0 = 0$) for the mapping $f^{-1} : W_{MEG} \to A$ for the group-averaged data set. Note that darker areas correspond here to regions that benefitted more from a higher number of coefficients.

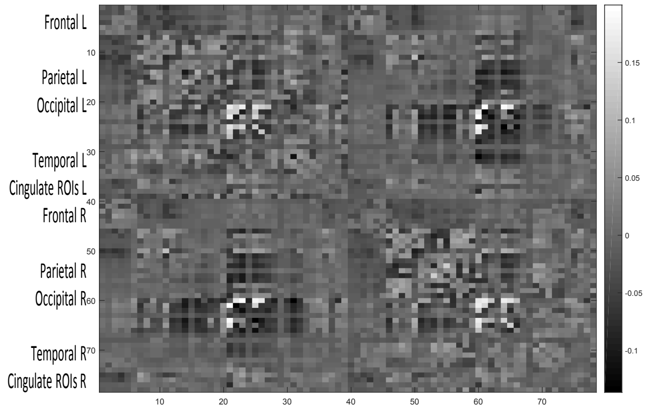

Figure 5.27: Absolute differences in the error for 2 in comparison with the error for 6 fitted coefficients ($K = 6$, $z_0 = 0$) for the mapping $f : A \to W_{fMRI}$ for the group-averaged data set. Note that darker areas correspond here to regions that benefitted more from a higher number of coefficients.

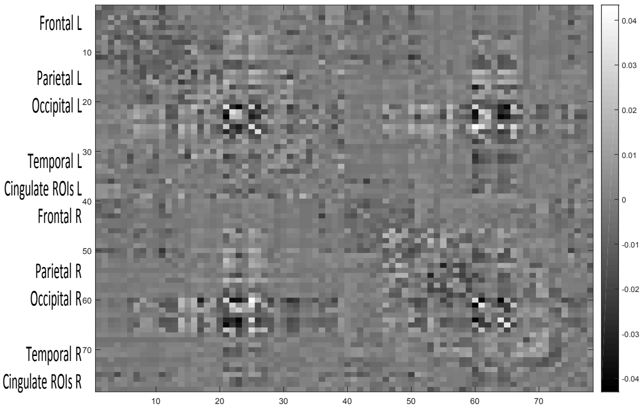

Figure 5.28: Absolute differences in the error for 2 in comparison with the error for 6 fitted coefficients ($K = 6$, $z_0 = 0$) for the mapping $f : A \to W_{MEG}$ for the group-averaged data set. Note that darker areas correspond here to regions that benefitted more from a higher number of coefficients.

first. Because all involved matrices are symmetric, we only need to fit the lower triangular matrices and the diagonal to get our fitting results. Thus, we first write all matrices in a vectorized form only containing their lower triangular and diagonal entries. For any matrix M of dimension $N \times N$ this vector will be denoted by $ltd(M)$. To be able to use the standard equation $Y = X \cdot \beta$ (with X design matrix, β parameter vector and Y image matrix) for a linear model, we need to define the variables for our case. In the case of $f(A) = W$, the response Y is just the image matrix W written as a vector containing the lower triangular and diagonal entries, $Y = ltd(W)$. The design matrix X is in the case of K as the maximal exponent

$$X = \begin{pmatrix} ltd(J) & ltd(I) & ltd(A) & ltd(A^2) & \dots & ltd(A^K) \end{pmatrix}$$

Therefore, the parameter vector β has the length $(K+2)$, where the first entry will be the coefficient c in front of the all-one matrix J and the second one is the coefficient for the identity matrix I and the others are in front of the matrix powers of A. Because the matrix powers of A are exploding in magnitude quickly, we normalize all the matrices beforehand dividing every entry by the absolute maximum entry of each matrix, which has the consequence that all matrices now have values between 0 and 1. Then, the *nlinfit.m* algorithm can be applied to our data using the underlying function *myfun.m* displayed here

```
function F = myfun(beta,xdata)

        F = xdata*beta;
end
```

where **xdata** refers to our design matrix X and **beta** is the parameter vector β. Because our model resembles a GLM, we could also use the pseudo-inverse of our design matrix **xdata** (*pinv(**xdata**))* and multiply it with the vectorized matrix Y in order to obtain the same estimated coefficients. In order to obtain the coefficient values for the original powers of the A matrix, we have to denormalize the estimated values by dividing the estimated coefficients each by the absolute normalization value from before.

(a) $f: A \rightarrow W_{fMRI}$

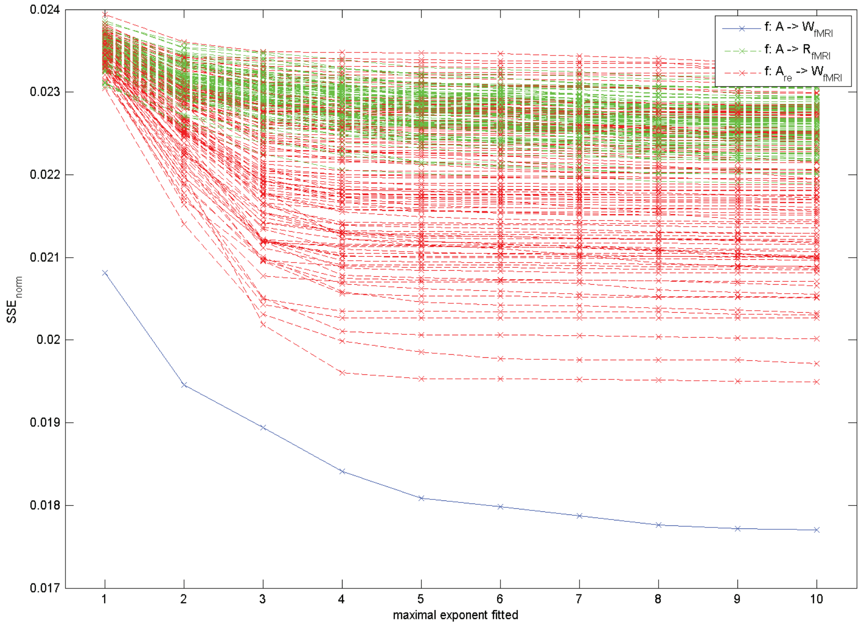

(b) $f: A \rightarrow W_{MEG}$

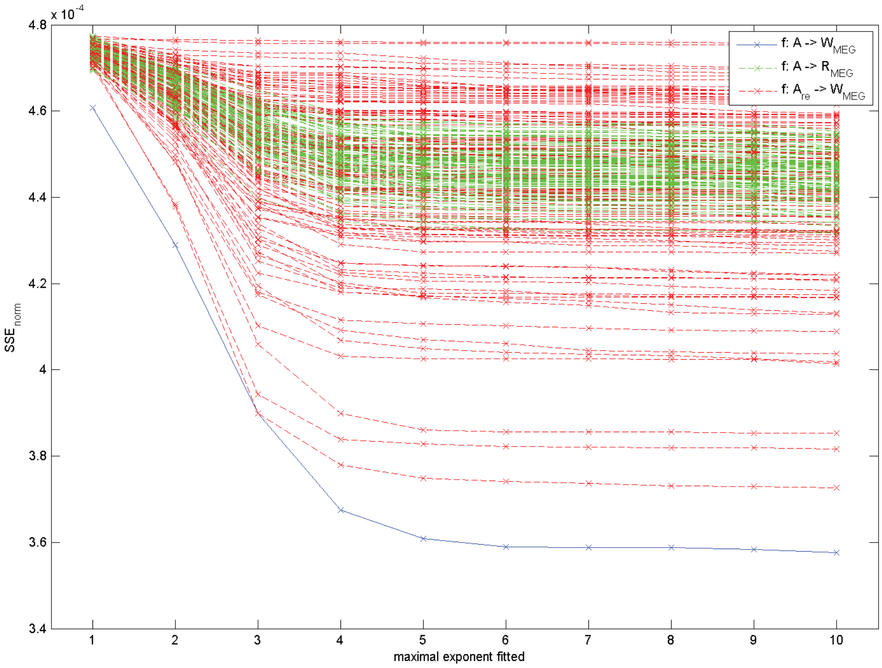

Figure 5.29: Plot of the normalized sum of squared errors (SSE_{norm}) of the function f in the topology domain for different maximal fitted exponents K and always in combination with a randomly reshuffled matrix R (R_{MEG}, R_{fMRI} and A_{re} denoting the reshuffled versions of W_{MEG}, W_{fMRI} and A, respectively) averaged over a range of z_0 values from -3 till 3 (always including an error matrix E) for the group-averaged data set.

(a) $f^{-1}: W_{fMRI} \rightarrow A$

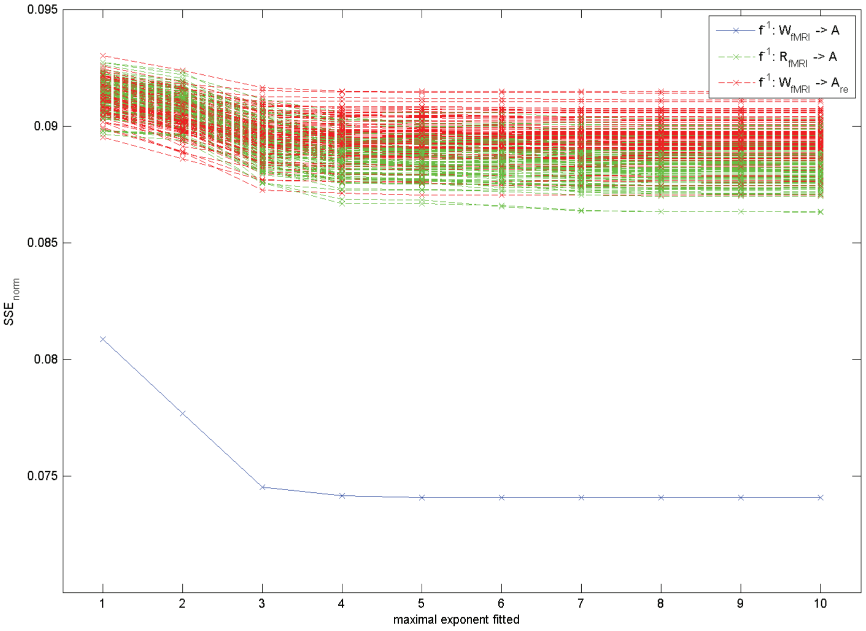

(b) $f^{-1}: W_{MEG} \rightarrow A$

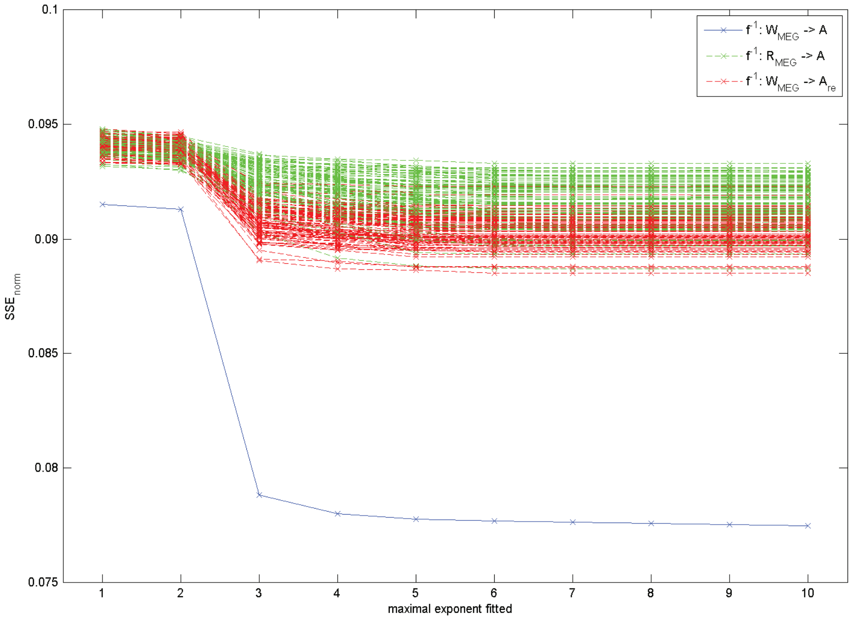

Figure 5.30: Plot of the normalized sum of squared errors (SSE_{norm}) of the function f^{-1} in the topology domain for different maximal fitted exponents K and always in combination with a randomly reshuffled matrix R (R_{MEG}, R_{fMRI} and A_{re} denoting the reshuffled versions of W_{MEG}, W_{fMRI} and A, respectively) averaged over a range of z_0 values from -3 till 3 (always including an error matrix E) for the group-averaged data set.

(a) $f : V_{re} \rightarrow W_{MEG}$

(b) $f : V \rightarrow R_{MEG}$

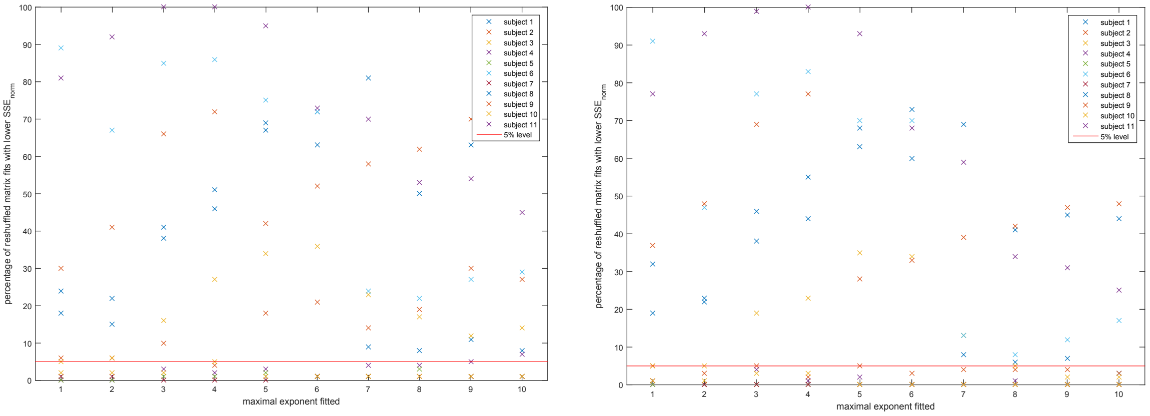

(c) $f^{-1} : R_{MEG} \rightarrow V$

(d) $f^{-1} : W_{MEG} \rightarrow V_{re}$

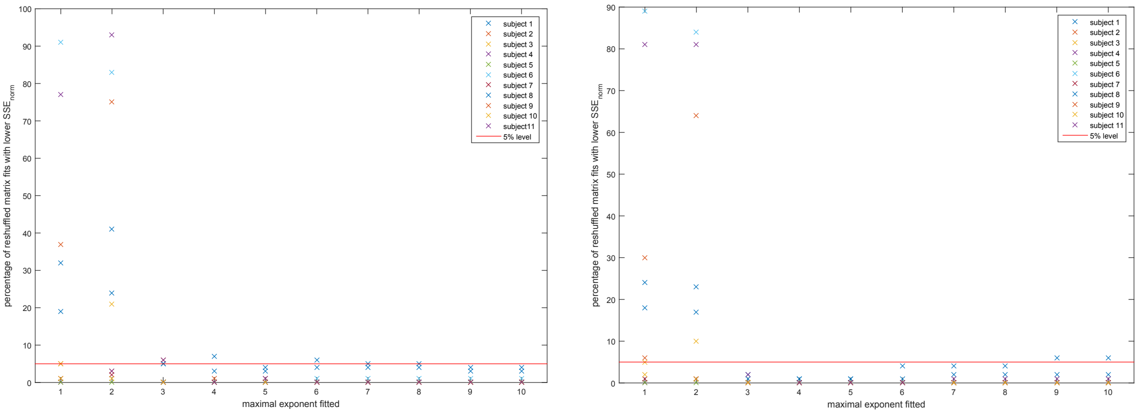

Figure 5.31: Plot of the percentages of reshuffled matrices that resulted in a lower normalized sum of squared errors (SSE_{norm}) in the topology domain for different maximal fitted exponents K with individual healthy controls results for all mapping including MEG (V denoting the weighted structural matrix and V_{re} denoting its randomly reshuffled version) for $z_0 = 0$ (with an error matrix E).

(a) $f : V_{re} \to W_{fMRI}$ (b) $f : V \to R_{fMRI}$

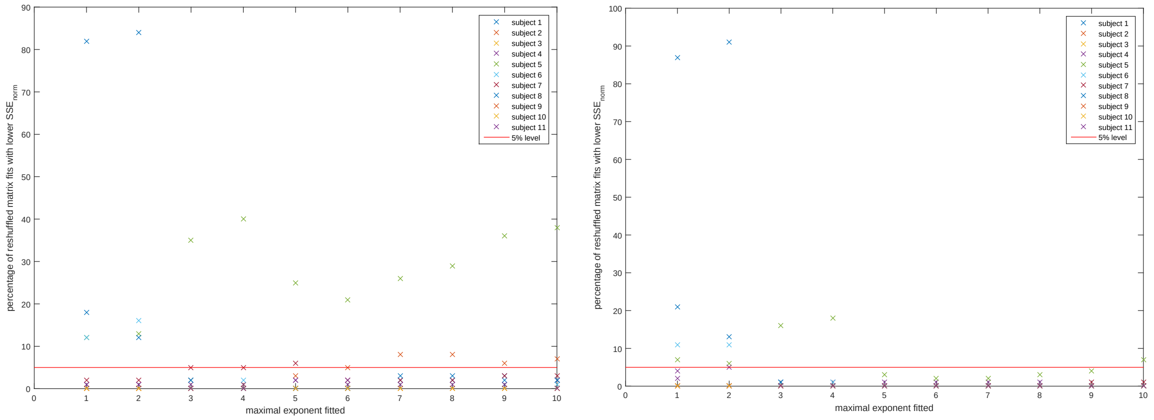

(c) $f^{-1} : R_{fMRI} \to V$ (d) $f^{-1} : W_{fMRI} \to V_{re}$

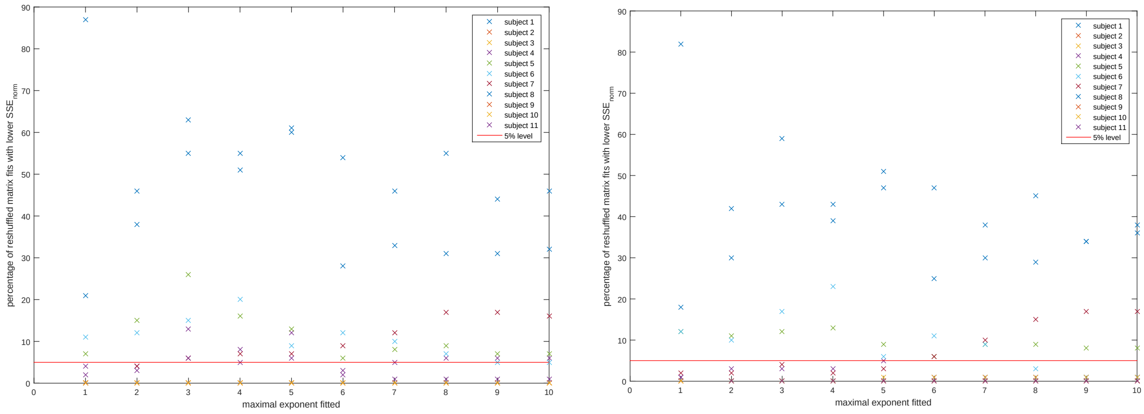

Figure 5.32: Plot of the percentages of reshuffled matrices that resulted in a lower normalized sum of squared errors (SSE_{norm}) in the topology domain for different maximal fitted exponents K with individual healthy controls results for all mappings including fMRI (V denoting the weighted structural matrix and V_{re} denoting its randomly reshuffled version) for $z_0 = 0$ (with an error matrix E).

5.6.9. DIMENSION DIFFERENCES

In practice, the $m \times m$ measured matrix W^* may be of a different dimension than the $N \times N$ matrix W. If $m \geq N$, then we can transform the measured matrix W^* to W as follows. Since W^* is symmetric, the spectral decomposition is

$$W^* = Y^* \Upsilon^* Y^{*T}$$

where the diagonal matrix $\Upsilon^* = \operatorname{diag}\left(\mu_1^*, \ldots, \mu_N^*, \mu_{N+1}^*, \ldots, \mu_m^*\right)$ with the real eigenvalues ordered as $\left|\mu_1^*\right| \geq \left|\mu_2^*\right| \geq \ldots \geq \left|\mu_m^*\right|$. The ordering here is different than the usual ordering in Section 5.6.1, because eigenvalues of W may be negative (in principle; although those of a correlation matrix are non-negative). Next, we let $\mu_k = \mu_k^*$ for $1 \leq k \leq N$ and $\mu_k = 0$ for $k > N$ and

$$Y^* = \begin{bmatrix} (Y_{11})_{N \times N} & (Y_{12})_{N \times (m-N)} \\ (Y_{21})_{(m-N) \times N} & (Y_{22})_{(m-N) \times (m-N)} \end{bmatrix}$$

so that

$$\widetilde{W}^* = \begin{bmatrix} Y_{11} & Y_{12} \\ Y_{21} & Y_{22} \end{bmatrix} \begin{bmatrix} \Upsilon & O \\ O & O \end{bmatrix} \begin{bmatrix} Y_{11} & Y_{12} \\ Y_{21} & Y_{22} \end{bmatrix}^T = \begin{bmatrix} Y_{11} \Upsilon Y_{11}^T & Y_{11} \Upsilon Y_{21}^T \\ Y_{21} \Upsilon Y_{11}^T & Y_{21} \Upsilon Y_{21}^T \end{bmatrix}$$

from which we choose $W = Y_{11} \Upsilon Y_{11}^T$. This method is well-known in the theory of singular value decompositions (see e.g. [39]) and provides the best $N \times N$ (in the mean-square sense) approximation of an $m \times m$ matrix.

6

THE EPIDEMIC SPREADING MODEL AND THE DIRECTION OF INFORMATION FLOW IN BRAIN NETWORKS

6.1. INTRODUCTION

Analyzing the human brain as a network led to the discovery of many interesting properties [15, 89, 93]. However, different measurement techniques capture different aspects of brain networks. Techniques such as diffusion tensor imaging (DTI) allow for the reconstruction of the structural brain network, which consists of a map of anatomical connections between brain regions. Functional imaging techniques, such as magneto-/electro-encephalography (MEG/EEG) and functional magnetic resonance imaging (fMRI), measure, either directly or indirectly, the activity of brain regions, from which functional brain networks can be reconstructed. Based on the brain regions' time series of activation we can extract two types of connectivity information: Functional connectivity refers to the existence of a statistical relationship between the activation time series, whereas effective connectivity captures the causal effect of one region's activity to the other regions' activities [2, 35]. While most studies have analyzed functional connectivity, recent approaches have focused on effective connectivity to gain knowledge about directionality [50, 70, 94]. Patients suffering from brain disorders often have altered structural brain networks [17]. In order to understand how these structural changes influence changes in the functional networks, we need to reveal the properties of the underlying connectome that facilitate the information flow and its direction in the functional networks.

The measure of transfer entropy (TE) has been used for MEG and EEG data for the estimation of effective connectivity [82]. Transfer entropy from node i to node j measures how much better a prediction of a next value of j becomes when we not only include the previous value of j but also the previous value of i. In the sense of Wiener's principle [125], transfer entropy can be interpreted as the causal influence of one brain region on another. Recently, the measure of transfer entropy has been expanded to a measure for phase-based connectivity, the so-called Phase Transfer Entropy [61, 74]. By applying the Phase Transfer Entropy, Hillebrand et al. [50] recently found a surprisingly consistent global spreading pattern from posterior to anterior brain regions in empirical MEG data in the higher frequency bands (*alpha1*, *alpha2*, and *beta* band) and a mirrored information flow from anterior to posterior regions in the *theta* band, where the latter has also been observed in EEG data [20]. The origin of these global patterns is still unclear. Hillebrand and co-authors [50] hypothesized that this global direction of information flow could be driven by strong hub connections in the posterior regions possessing the highest levels of neuronal activity in the network during the resting-state [21, 70].

Recent studies have shown that simple models of activity spread can contribute to our understanding of brain dynamics [1, 24]. For example, Mišić et al. [69] applied a simple deterministic cascade model and discovered that hubs and the shortest paths of the structural brain network have a high influence on the efficiency of spreading dynamics. Even though those simple models ignore microscopic details of the spreading

---

This chapter has been published in J. Meier, X. Zhou, A. Hillebrand, P. Tewarie, C.J. Stam and P. Van Mieghem, *The Epidemic Spreading Model and the Direction of Information Flow in Brain Networks*, *NeuroImage*, **152**, pp. 639-646 (2017).

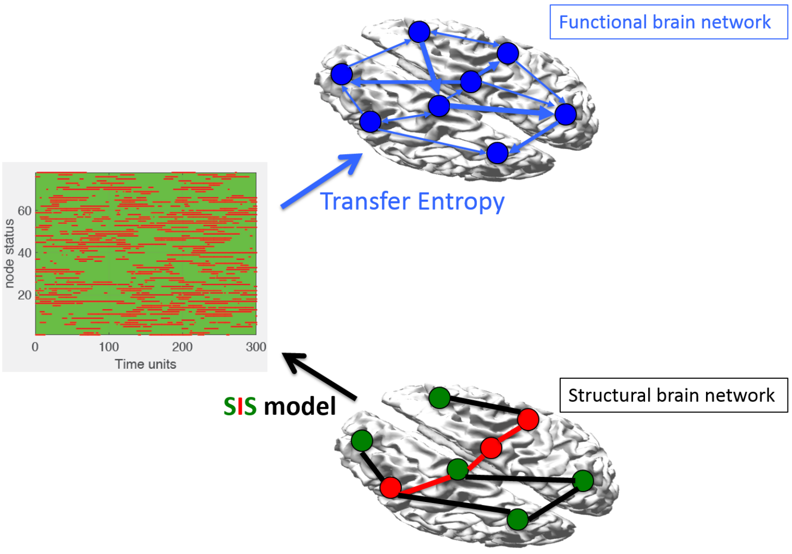

Figure 6.1: **Schematic overview of performed modelling.** We ran a Susceptible-Infected-Susceptible (SIS) process on the underlying structural brain network. Based on the activation time series of the nodes (see left panel, red represents the activated state and green the excitable state), we calculated all pairwise transfer entropies to construct a network of the same nodes but with the link weights representing the functional interactions between node activities.

process, the scarcity of parameters simplifies the exposure of underlying general principles. Further, there is evidence that the brain operates near a critical phase transition [44, 80, 97, 127]. It is known from statistical physics that the details of the applied model become irrelevant near such a transition. This vicinity of a phase transition could explain why simple models [24, 44] have been successful in capturing more complicated model findings [51, 52].

A simple epidemic process often approximates empirical spreading processes on networks for various applications, e.g. information propagation and gossip spreading in social networks [75]. The Susceptible-Infected-Susceptible (SIS) epidemic is one of the simplest models of an epidemic. In an SIS epidemic process, a node can be in two states, either infected or susceptible (and can be infected by its infected neighbors). The advantages of the epidemic spreading model are that the effective spreading rate τ is the only a-priori chosen parameter and that we can also study the model analytically. A previous study [90] applied a discrete-time epidemic process on the structural brain network and identified the structural degree product as a driving force for the effective connectivity between two nodes. In the case of the functional brain network, brain regions can be activated (infected) and spread this activation to their anatomically neighboring excitable (susceptible) regions. Applying the well-developed theory of epidemics may lead to a better understanding of the activity spreading in the brain and in particular reveal the structural properties that drive the global spreading dynamics.

The SIS process can analytically be described as a continuous-time Markov chain with 2^N states where N is the number of nodes in the network. The embedded Markov chain approximates the continuous-time SIS process as a discrete-time process and contains the transition probabilities but no longer the precise timing of the events [113]. For this study, we simulated an epidemic spreading process on the structural brain network in a continuous-time framework since we were interested in the smaller time-scale dynamics (see Figure 6.1) [113]. We used the transfer entropy (instead of the Phase Transfer Entropy) for the estimation of pairwise directed interactions since the SIS model generates binary time series.

The aim of this chapter was to elucidate the topological properties of the structural brain network that give rise to the empirically observed effective connectivity patterns in functional brain networks. To this end, time series were generated by applying a continuous-time SIS model on a human connectome, following which effective connectivity was estimated using pairwise transfer entropies for different time delays. Because previous studies [69, 90, 96] and analytic reasoning (see Appendix 6.6.5) identified the degree as a driving force behind spreading dynamics, we directed a special focus on the relationship between the structural degree and the outcome of the SIS spreading process.

6.2. METHODS

STRUCTURAL NETWORK

For the structural network, we used a literature-based DTI network from a previous study based on 80 healthy subjects (for details see [40]), where a node corresponds to a cortical region in the automated anatomical labeling (AAL) atlas [104]. In short, every two cortical regions from the 78 AAL atlas regions were considered to be connected if the end points of two white matter tracts were located in these regions [40]. Via a non-parametric sign test only the significant links were included in the group-averaged structural connectivity matrix. This processing resulted in a binary connectivity matrix for the structural brain network, which we will further refer to as the structural adjacency matrix A.

SIS PROCESS

In an SIS epidemic process on an undirected and unweighted graph G with N nodes and L links, the state of a node i at time t is specified by a Bernoulli random variable $X_i(t) \in \{0,1\}$: $X_i(t) = 0$ for an excitable node and $X_i(t) = 1$ for an activated node. Here, we have replaced the states 'susceptible' and 'infected' from classic epidemic theory with 'excitable' and 'activated' to indicate the status of a brain region. Only an active node can activate its direct neighbors that are still excitable. We assume that the infection (activation) process and the curing process (change to excitable status) are Poissonian with rates β (infection rate) and δ (curing rate), respectively [113]. The infection and curing process are independent of each other. The continuous-time SIS model is defined by the differential equation for the expected status of any node j, $E[X_j]$,

$$\frac{dE[X_j]}{dt} = E[-\delta X_j + (1-X_j)\beta \sum_{k=1}^{N} a_{kj} X_k] \,, \tag{6.1}$$

where $\sum_{k=1}^{N} a_{kj} X_k$ counts the number of activated neighbors of node j. The effective infection rate is denoted by $\tau = \beta/\delta$.

DETAILS OF THE SIMULATION

As mentioned in the introduction, there is evidence that the brain operates with its dynamics near a critical phase transition [44, 80, 127]. As in [90], we chose β and δ such that the SIS dynamics are slightly above the critical epidemic threshold τ_c which we verified with continuous-time simulations (Figure 6.2). We used the continuous-time simulator SIS simulator (SISS) [105] to simulate an SIS-epidemic on the structural network with $\beta = 0.1$ and $\delta = 0.5$ [90] resulting in an effective spreading rate $\tau = \beta/\delta = 0.2$. For each simulation run, we initially activated 15 nodes at random, which is approximately 20% of the whole network, to enable a comparison with previous results [90]. Initially infecting 15 nodes also ensures that the probability for the activity-spread to die out is nearly zero [59] (see Appendix Figure 6.5).

We ran a simulation of 4096 time units [90]. We applied 0.1 time units as a sample interval resulting in 40960 time points for one simulation, forming for each node an activation time series of zeros (node is not activated at time instance t) and ones (node is activated at time instance t) (for an example of an activation time series see Figure 6.1). To focus on the metastable (quasi-stationary) state [113], we disregarded the initial phase of the spreading process by calculating all our results based on the second half of the simulation time (from 2048 to 4096 time units). There exists no analytic reasoning for the metastable state of an epidemic spreading process yet [16, 60] but based on our simulation results we can conclude that extracting the second half of the simulation time assures the exclusion of the initial phase (see Appendix Figure 6.6). All presented results were averaged over 100 simulation runs.

TRANSFER ENTROPY

In order to capture the delayed influence, we calculated for every node pair i and j the transfer entropy (TE) from node i to node j over the whole simulation time series as

$$TE_{i\to j}(h) = \sum_{k,l,m=\{0,1\}} \Pr[X_j(t+h) = k, X_j(t) = l, X_i(t) = m] \cdot \log\left(\frac{\Pr[X_j(t+h) = k | X_j(t) = l, X_i(t) = m]}{\Pr[X_j(t+h) = k | X_j(t) = l]}\right) \tag{6.2}$$

for a certain time delay h. Transfer entropy can be interpreted as a delayed correlation measure that is corrected for auto-correlation, which we can employ for analytic derivations (see Appendix 6.6.4 and 6.6.5). Sim-

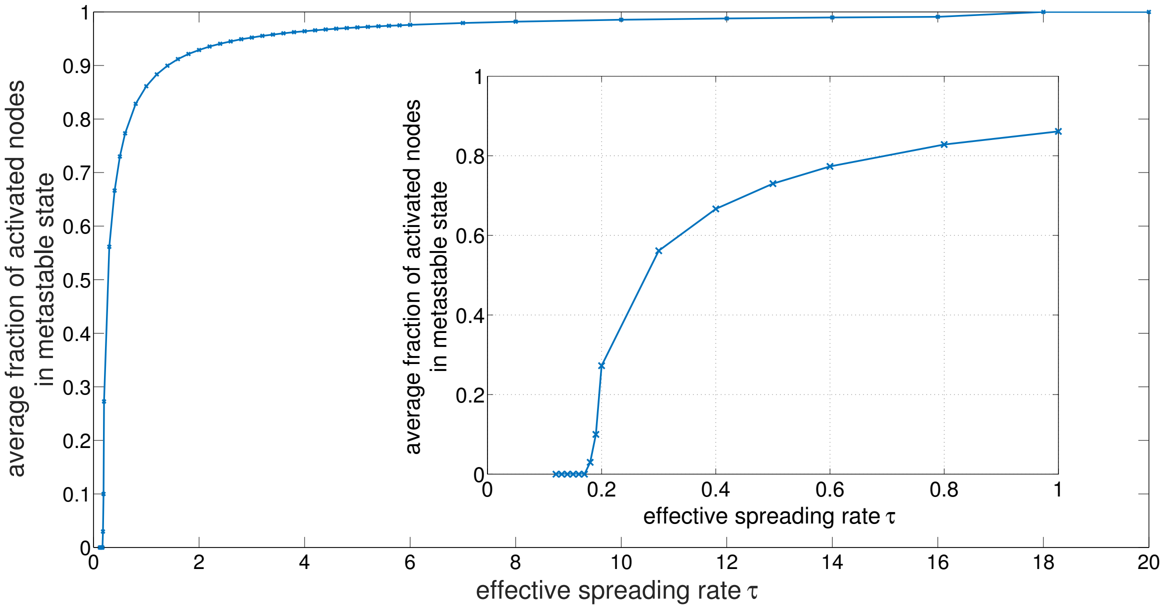

Figure 6.2: **Average fraction of activated nodes.** Average fraction of activated nodes in metastable state for different effective infection rates τ. The smaller graphic is a zoomed-in plot for smaller values of τ.

ilar to [50], we defined the directed transfer entropy (dTE) from node i to node j as

$$dTE_{i\to j}(h) = \frac{TE_{i\to j}(h)}{TE_{i\to j}(h) + TE_{j\to i}(h)}\,, \tag{6.3}$$

which quantifies the preferred direction of flow. Since the transfer entropy can only take positive values, the directed transfer entropy measure is well-defined and ranges from 0 to 1. If the preferred flow of information is from node i to node j, then $0.5 < dTE < 1$, else $0 < dTE < 0.5$. For every node, we calculated the average value of the directed transfer entropy from this node to all other nodes in the network. If this averaged directed transfer entropy for node i was larger (smaller) than 0.5, then node i is a preferred sender (receiver) of information. In order to quantify the global pattern of information flow, we calculated a posterior-anterior (PA) index

$$PA = \overline{dTE}_{posterior} - \overline{dTE}_{anterior}\,,$$

where $\overline{dTE}$ denotes the average over the directed transfer entropy values of all posterior and anterior regions, respectively [50]. Thus, a positive posterior-anterior value indicates a posterior-anterior pattern and a negative posterior-anterior index points towards a pattern of information flow in the opposite direction. The posterior-anterior index was also normalized by the difference between the maximum and the minimum of all observed posterior-anterior values. All observed posterior-anterior values were then tested against the null hypothesis of being significantly high or low by permuting the needed averaged directed transfer entropy values and re-calculating the posterior-anterior value (5000 repetitions).

We repeated the analysis for randomly reshuffled versions of the structural adjacency matrix. We used a reshuffling technique where we selected two matrix entries at random and then interchanged their matrix entries preserving the number of links in the network. We repeated this reshuffling step 1000 times to obtain one reshuffled version of the matrix. In the same way, we generated 100 reshuffled versions of the structural adjacency matrix. This method does not preserve the individual degrees and also not necessarily the degree distribution; it rewires our network connections ignoring any preferences for posterior or anterior regions. Thus, the links of the resulting reshuffled networks are randomly distributed and the spatial distribution of the degrees is uniformly spread over the whole network.

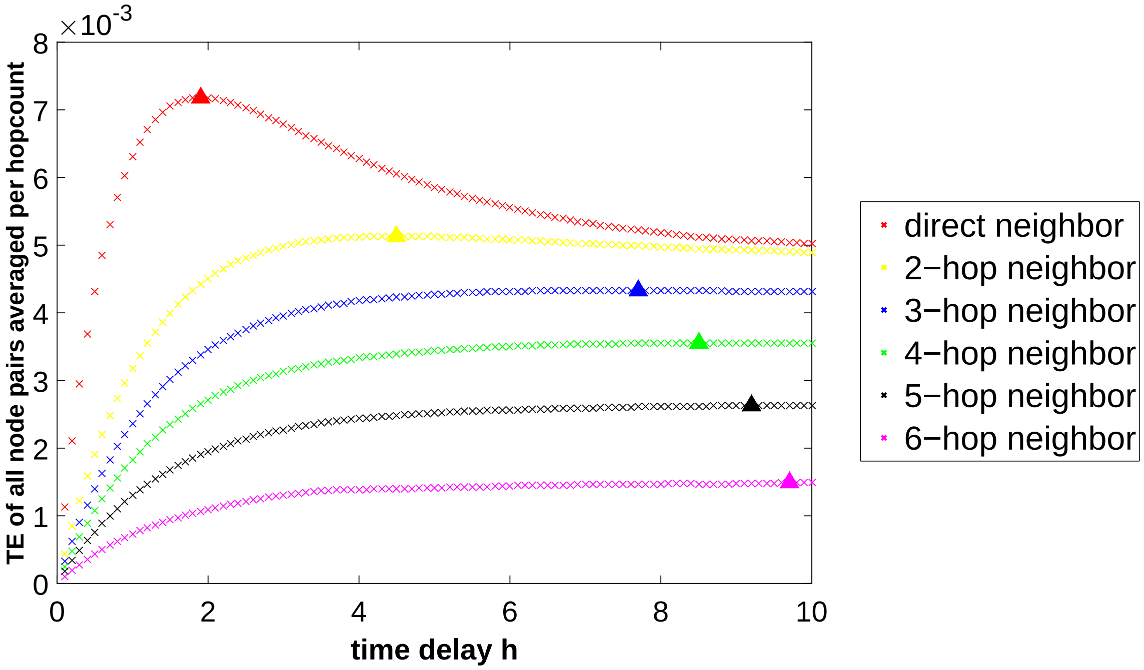

Figure 6.3: **Transfer entropy over different time delays.** Averaged transfer entropy (TE) of all node pairs for different time delays. The transfer entropy values for different node pairs are colored differently according to the hopcount between them. We observe that direct neighbors have the highest transfer entropy and that the further apart two nodes are in terms of hopcount, the smaller the transfer entropy between them. The triangles mark the maximum transfer entropy value for each hopcount over all time delays. The larger the hopcount, the larger is the time delay needed to reach this maximum transfer entropy value.

6.3. RESULTS

We plotted the averaged transfer entropy over all node pairs for different time delays h in Figure 6.3 depending on the hopcount between them (i.e. the number of hops or links in the shortest path connecting the two nodes). The notion of a hopcount refers to the distance between two nodes (cortical regions) measured as the minimal number of links (hops) that one has to traverse in order to reach one node from the other node in the underlying structural network. We observed that a direct structural connection leads to the highest transfer entropy value between two nodes, and that the further two nodes are apart in terms of hopcount, the smaller the transfer entropy between them. For each hopcount, there exists a certain time delay h that maximizes the average transfer entropy (Figure 6.3). We observed that the further another node is away (in terms of hopcount), the longer time delay is necessary to maximize the influence (transfer entropy) on that node.

Concerning the global patterns of information flow, we found three regimes depending on the chosen time delay (see Figure 6.4a). For small time delays, we observed a significantly negative posterior-anterior value, i.e. an information flow from anterior to posterior regions (regime (I), P value < 0.05, Appendix Figure 6.7). After a transition phase (regime (II), no significant posterior-anterior value), the opposite pattern was observed (regime (III)), i.e. a posterior-to-anterior information flow, where the posterior-anterior values for larger time delays were significantly positive (P value < 0.05). In addition, depending on the time delay the structural degree correlated positively or negatively with the average directed transfer entropy (see Figures 6.4b and 6.4c). In regime (I), we observed a significantly negative correlation between the degree and the average directed transfer entropy, which means that higher degree nodes seem to be stronger receivers of information from the network than lower degree nodes (see Figure 6.4d). The significance of the correlation was tested similarly to the posterior-anterior value by permuting the directed transfer entropy values and recomputing the correlation in order to establish a null distribution (5000 repetitions, null hypothesis of observing a significantly higher or lower correlation, Appendix Figure 6.7). From a certain time delay onwards (regime (III)), the correlation between degree and directed transfer entropy became significantly positive (Figure 6.4c), identifying hubs as strong senders of information. When visualizing the directed transfer entropy values on the template brain for the minimum and maximum posterior-anterior value, we recognize a global front-to-back and back-to-front pattern, respectively (see Figures 6.4d and 6.4e). In Figure 6.4d, the anterior regions seem to possess more outgoing flow of information (darker colors) and the posterior regions have a more incoming flow (lighter colors) for $h = 0.2$, whereas the opposite pattern can be perceived for $h = 6$ (Figure 6.4e).

The results for the reshuffled version of the structural adjacency matrix with a uniform degree distribution over posterior and anterior regions show a less variant behavior for different time delays (see Appendix B). For the randomly reshuffled matrices, we observe a significantly positive correlation (yet decreasing for longer time delays) between the node degree and the directed transfer entropy. However, in comparison with the structural adjacency matrix, the reshuffled matrices do not reach such high (low) correlation values for longer (shorter) time delays (see Appendix Figures 6.9 and 6.10). Concerning the resulting global pattern, we observe a slightly positive posterior-anterior value for most of the randomly reshuffled matrices (see Figure 6.8). In line with the correlation values, the randomly reshuffled matrices do not show much variance over different time delays with respect to their posterior-anterior values (Figures 6.8 and 6.10).

We also repeated our analysis on the directed structural macaque brain [52] (see Appendix C). In this directed network, nodes possessing a high total number of connections seem to have a more sending property in general. However, for short time delays, hubs with more incoming than outgoing links, appear to be more receiving (for a detailed description see Appendix C).

6.4. DISCUSSION

Using a simple model of activity spread, we were able to reproduce the empirically observed global patterns of effective connectivity. In addition, the structural degree of a node was identified as a strong indicator for the sending/receiving property of a brain region. Moreover, the further two brain regions were away in terms of hopcount in the structural network, the smaller the transfer entropy between them.

Our study shows that the structural (topological) distance between two brain regions has an influence on their transfer entropy. From our simulation results, we can conclude that the further apart two nodes are in terms of hopcount in the underlying structural brain network, the smaller their transfer entropy. This result is in line with our previous study that identified the structural hopcount as a driving force behind functional connectivity (see Chapter 5). Stam et al. [90] found the highest effective connectivity as the result of a direct structural connection and Honey and colleagues [51] stated that indirect connections with the hopcount 2 have a strong influence on the strength of functional connections between brain regions. Moreover, Goñi an co-authors [41] stated that shortest paths of the structural network and detours along them are good predictors for functional connectivity, which also implicates a lower connectivity for node pairs with larger hopcount between them. These results confirm the common assumption that longer paths in the structural brain network only have a small influence on the functional connectivity between two brain regions [81, 128] (and also in Chapter 5). Our results are in agreement with these earlier studies by identifying the hopcount between two brain regions as an indicator for their functional interaction and show that these general principles also hold for effective connectivity.

We were able to replicate the empirically observed global directionality patterns based on a simple epidemic spreading process. Without imposing any directionality on the pairwise structural interactions, we observed an overall dominant pattern of directionality based on an underlying *undirected* structural network. It therefore seems that the pure presence of an unequal degree distribution with a spatial gradient along the anterior posterior axis is enough to create overall pre-dominant directions of information flow. The observed direction of information flow in our model depended on the chosen time delay for the estimation of the transfer entropy. The empirically discovered anterior-to-posterior pattern in lower frequency bands (*theta*) resembles the patterns observed in our model when using short time delays, whereas the opposite pattern that is empirically observed in higher frequency bands (*alpha1*, *alpha2* and *beta*) coincides with the patterns in our model when applying longer time windows [50]. These opposite directions of information flow probably indicate the presence of a loop between the two interacting subsystems of the Default Mode Network, the temporal and the fronto-parietal system representing a mechanism of integration of brain function [29]. The temporal system is involved in memory and the fronto-parietal system is responsible for self-relevant mental simulations [13]. These two processes, memory and self-relevant mental simulations, seem to be active simultaneously and on different time scales, which could provide a biological interpretation of the mirrored directions of information flow. Furthermore, these opposite directions have also been reported in invasive animal recordings, for e.g. the visual system [4, 109], and could represent the mechanism of memory consolidation [84].

Our modeling results suggest that the opposite directions of the global pattern of information flow reveal

(a) Posterior-anterior (PA) value and correlation between degree and average directed transfer entropy over different time delays.

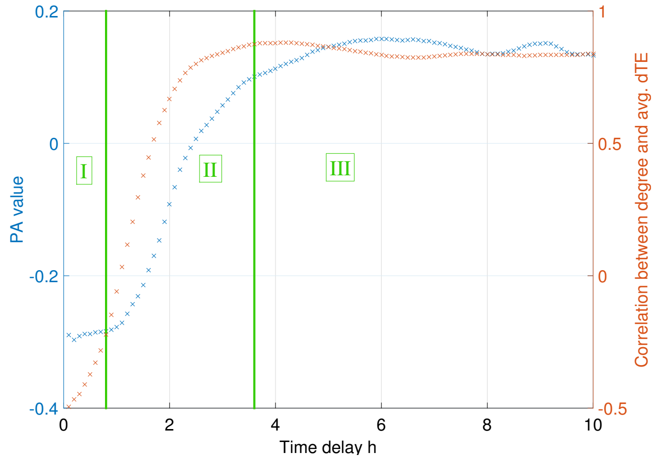

(b) Directed transfer entropy versus degree for $h = 0.2$ (regime (I)).

(c) Directed transfer entropy versus degree for $h = 6$ (regime (III)).

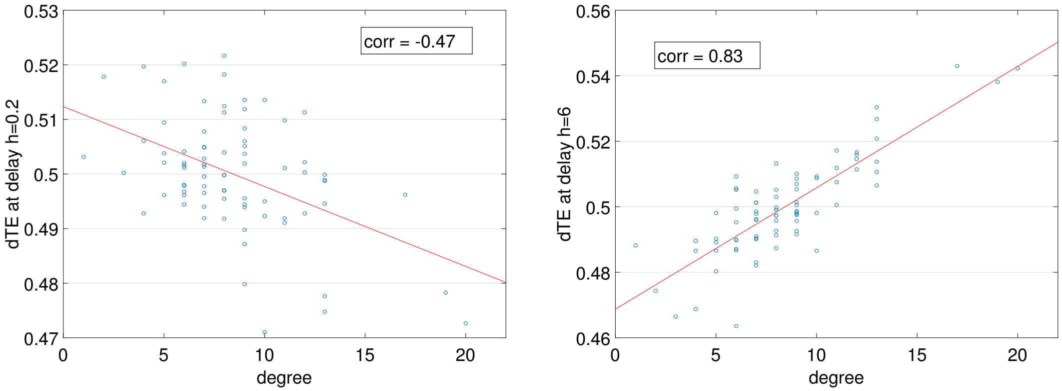

(d) Directed transfer entropy on the template brain for $h = 0.2$ (regime (I)).

(e) Directed transfer entropy on the template brain for $h = 6$ (regime (III)).

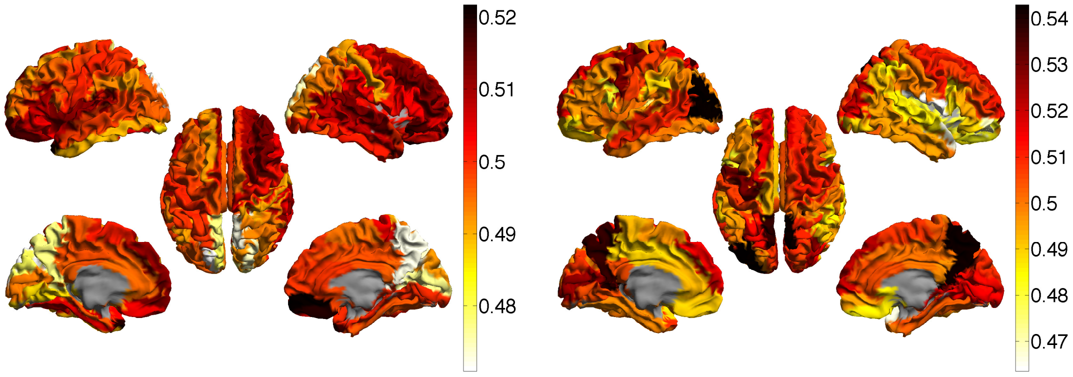

Figure 6.4: **Opposite patterns of information flow.** (a) Posterior-anterior value and correlation between degree and averaged directed transfer entropy (dTE) over different time delays. In regime (I) we observe a significantly negative posterior-anterior value and correlation. In (II) we have a transition phase and in (III) we face a significantly positive correlation and posterior-anterior value. (b) Averaged dTE versus degree for the time delay with minimal posterior-anterior value, $h = 0.2$. (c) Averaged dTE versus degree for the time delay with maximal posterior-anterior value, $h = 6$. (d)+(e) dTE for each brain region on the parcellated template brain for $h = 0.2$ (d) and $h = 6$ (e). We show the brain here in clockwise order from the left, top, right, right midline and left midline.

the different time scales of the spreading process and seem to be linked to the sending/receiving properties of the structural hubs. For short time delays, our results show that direct neighbors influence nodes much more than indirect neighbors (Figure 6.3). Stam et al. [90] showed previously that hubs are overall more often activated (by their direct neighbors) than lower degree nodes. Because of the higher number of potentially activated direct neighbors, the activation of hubs does not only occur more frequently but also with a higher activation rate (see Equation (6.1)) and thus on a shorter time scale than the activation of lower degree nodes. This frequent activation of hubs on a shorter time scale is probably the reason that hubs are strong receivers and, in return, lower degree nodes appear to be strong senders of information flow on short time scales. Since structural brain networks have the strongest hubs in posterior regions [13], these posterior hubs acting as preferred receivers cause the anterior-posterior information flow for short time delays in our model. For longer time delays, the dominant influence of the direct neighbors decreases and the influence of the indirect neighbors increases (Figure 6.3). Because hubs are activated more often and can activate not only more direct but also, on longer time scales, more indirect neighbors, they are strong senders of information for longer time scales. On the contrary, lower degree nodes have less influence on the network and act as strong receivers of information flow for longer time delays in our model. Together, these scenarios provide a possible explanation for the posterior-anterior pattern of information flow in our SIS model in the case of longer time delays. Summing up, the posterior hubs seem to play a dominant role for the global patterns, which are hypothesized to represent a mechanism of integration [50]. The hypothesis is further strengthened by the disappearance of the opposite information flow directions in the randomly reshuffled networks. Thus, the uneven spatial distribution of the degrees seems to be a necessary (but maybe not sufficient) condition for observing mirrored directions of global information flows. This finding is in line with multiple studies that uncover hubs to drive the integration of information in the human brain [87] and to play a special role in both the healthy [40, 42] and diseased brain [17]. [107] have shown that a large amount of the total communication travels through the structural hubs. Therefore, these hubs are very likely both strong senders and receivers, which could lead to a mirrored pattern of information flow. Furthermore, a recent study by Gollo and colleagues [38] concluded for the primate brain that structural hubs are "slaves" of their many connections since they not only have a powerful influence on the global network dynamics but also receive a lot of input from the rest of the network. Our results for the directed structural macaque brain confirm this different behavior for hubs regarding different time scales (see Appendix C). These empirical results provide some intuitive explanation for the opposite directions of information flow, towards the posterior hubs and, simultaneously (though on a different time scale), away from them.

Recent studies applying causality measures like transfer entropy [43] and Granger causality [65] identified a system of anticipatory synchronization as the driving force behind counterintuitive information flow directions. Anticipatory synchronization means that the receiver can learn to anticipate the sender's actions, which requires an adapting system. Hahs and Pethel [43] have shown that in such a system the estimated role of the sender and receiver can switch depending on the applied sampling rate. The simple SIS model does not allow anticipation and the described phenomenon caused by anticipatory synchronization can thus not apply to the modeling results. However, the dynamics of anticipation have already been reported for empirical brain dynamics [55] and for task-related data of the macaque brain [65]. Thus, for empirical observations of counterintuitive directions of information flow, the sampling rate [43] could indeed provide an explanation.

We applied a simple SIS epidemic spreading model that ignored microscopic details of the real underlying neuronal processes in order to analyze global patterns. Even though our model ignored heterogeneity except for the underlying structural network restrictions, we were able to generate the empirically found global, directed spreading patterns [50]. The SIS model can be regarded as a simplified version of the neural transmission dynamics, which deliberately ignores microscopic details of the underlying neural dynamics and neuronal architecture in order to allow macroscopic whole-brain analysis. This type of model is "conceptual": the aim is not to explain neurons, spikes, synapses etc., but the topology of large-scale brain networks and their global network dynamics. Our approach aligns with other recent studies analyzing global spreading dynamic principles with the help of simple dynamic models [69, 95]. Mišić et al. [69] found, applying a deterministic cascade model, that the hubs and a backbone of core pathways facilitate the spreading process and shortest paths accelerate this phenomenon. Similarly, diffusion models have identified the shortest path structure of the structural brain network as a driving force behind the network dynamics [41] and categorized functional modules of the brain [8, 25]. These simple modeling approaches should be considered as complementary to the traditional neural mass and field models from computational neuroscience [22]. Most importantly, these simpler models allow us to study the basic principles of dynamics on brain networks with a minimum set of a-priori assumptions and parameters. For more complex models, the emergence of any global pattern could be ascribed to any of the (many) underlying model properties. In our case, because of the simplicity of the model and the underlying undirected network, the emergence of global patterns of effective connectivity can be traced back to the spatially unequal distribution of hubs.

6.5. CONCLUSION

In this study, we analyzed local and global network dynamics of the brain network by applying an SIS epidemic spreading model on the human connectome. We found that direct structural connections induced higher transfer entropy between two brain regions and that transfer entropy decreased with increasing distance between nodes (in terms of hops in the structural network). Applying the SIS model, we were able to confirm the empirically observed information flow patterns based on an underlying *undirected* structural network where posterior hubs seem to play a dominant role in the network dynamics. For small time scales, when these hubs acted as strong receivers of information, the global pattern of information flow was in the posterior-to-anterior direction and in the opposite direction when they were strong senders. Our analysis suggests that these global patterns of directional information flow are the result of an unequal spatial distribution of the structural degree between posterior and anterior regions and the direction of information flow seem to be linked to different time scales of the spreading process. Based on the developed framework, future studies should investigate how structural changes in patients suffering from brain disorders can influence these global patterns of information flow.

6.6. APPENDIX

6.6.1. ADDITIONAL FIGURES

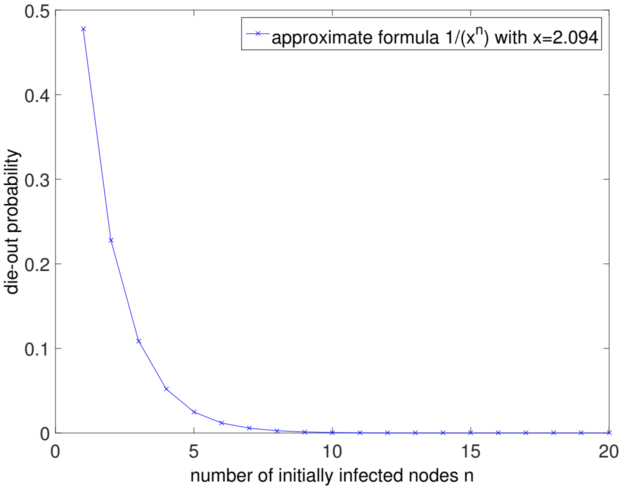

Figure 6.5: **Die-out probability of activity spreading.** Approximate formula for the die-out probability $1/x^n$ (Liu and Van Mieghem, 2016a) depending on the number of initially infected nodes n and $x = \tau \cdot \lambda_1$ the product between the effective infection rate $\tau = 0.2$ and the largest eigenvalue of the structural adjacency matrix A, $\lambda_1 = 10.47$, in our case.

6.6.2. RANDOMLY RESHUFFLED MATRICES

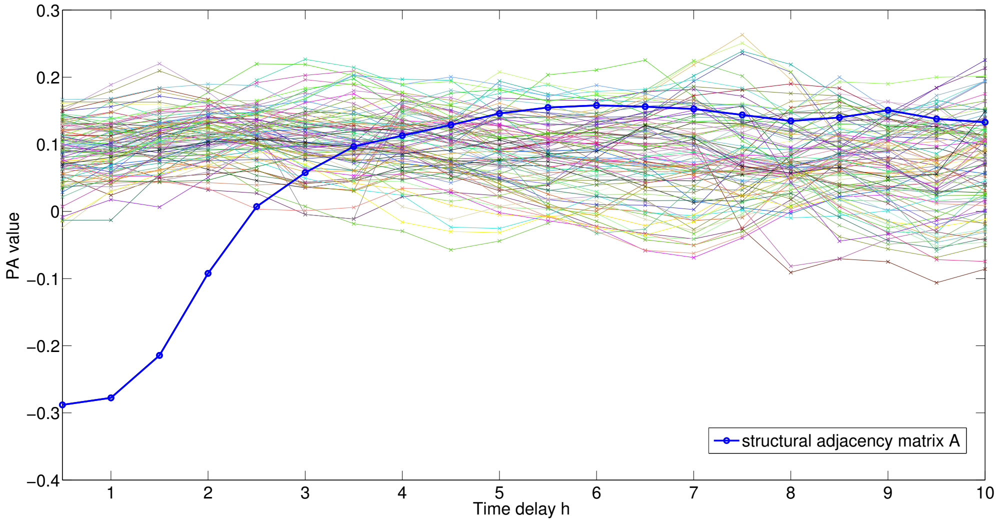

Figure 6.8: **Global pattern in randomly reshuffled networks.** Posterior-anterior (PA) value over different time delays. The blue line represents the already known result for the structural adjacency matrix A and the other lines indicate the PA values for the randomly reshuffled matrices.

6.6.3. DIRECTED STRUCTURAL NETWORK OF THE MACAQUE BRAIN

We repeated the analysis on the directed structural networks of the macaque with $N = 47$ nodes, which has earlier been analyzed by Honey et al. [52]. The SIS model can easily be extended towards a directed underlying network [57]. Applying the same effective infection rate $\tau = 0.2$ as for the human brain, we ran 10 simulation runs on the macaque neocortex. In a directed network, we can calculate different forms of the nodal degree, the in- and the out-degree but also the sum of them both. We plotted the correlation between the different forms of the degree and the directed transfer entropy for different time delays in Appendix Fig-

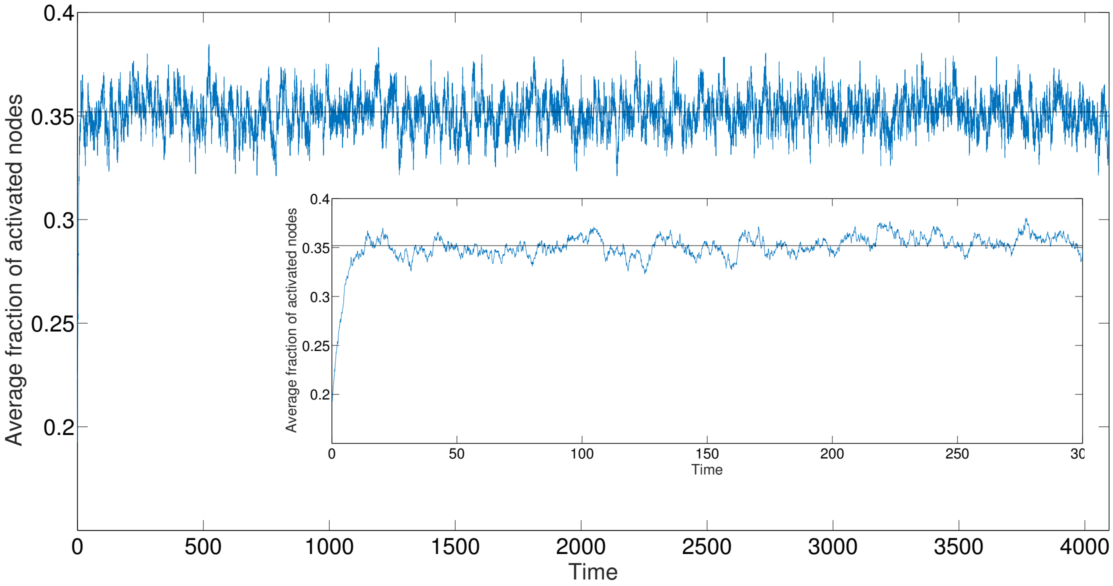

Figure 6.6: **Fraction of activated nodes over whole simulation time.** Mean fraction of activated nodes for every time step averaged over the 100 simulation runs and the whole simulation time for the applied effective infection rate $\tau = 0.2$. The smaller plot shows the first 300 time units. In both figures, the horizontal black line represents the mean fraction of activated nodes in the metastable state.

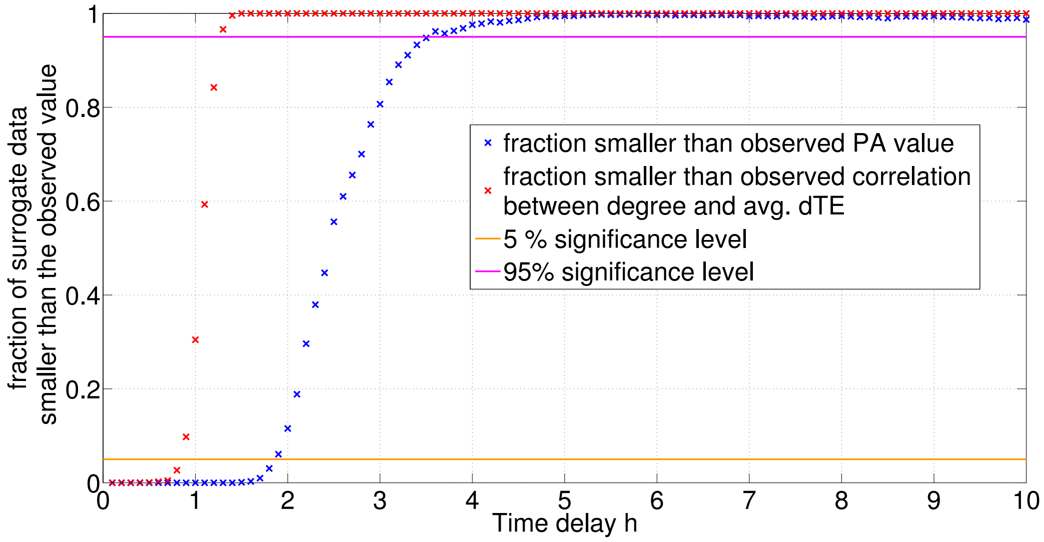

Figure 6.7: **Global pattern in surrogate data.** For different time delays, fraction of surrogate data possessing a smaller value than the observed posterior-anterior (PA) value and the observed correlation between degree and averaged directed transfer entropy (dTE) value, respectively. When the fraction is above 0.95, the observed value is significantly larger based on the 5% significance level. For time delays where the fraction is below the 0.05 line, we observe a significantly smaller value than the surrogate data (P value < 0.05).

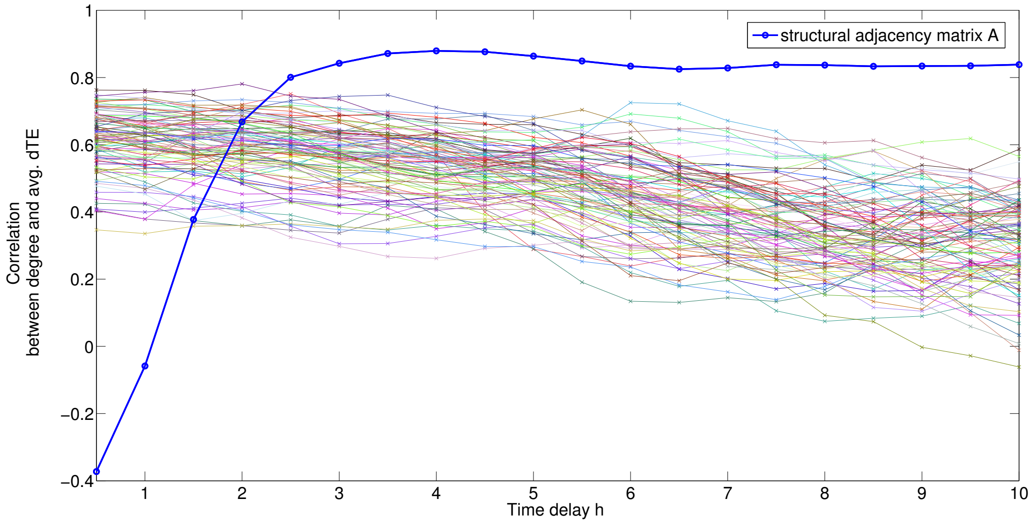

Figure 6.9: **Correlation between degree and dTE in randomly reshuffled networks.** Correlation between degree and averaged directed transfer entropy (dTE) over different time delays. The blue line represents the already known result for the structural adjacency matrix *A* and the other lines indicate the correlation values for the randomly reshuffled matrices.

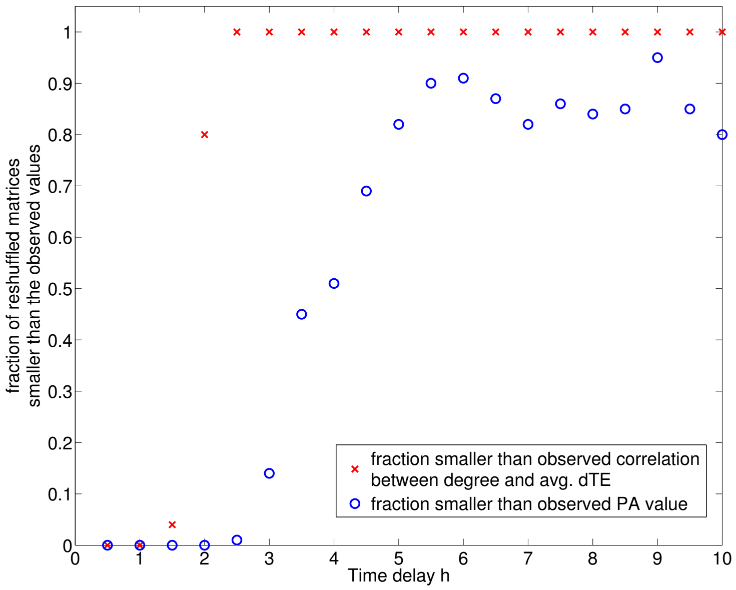

Figure 6.10: **Comparison between reshuffled networks and structural network.** For different time delays, fraction of reshuffled networks possessing a smaller value than the observed posterior-anterior (PA) value (in blue) and the observed correlation between degree and averaged directed transfer entropy (dTE) value (in red), respectively. For small time delays, the behavior of the structural adjacency matrix *A* is significantly different than the behavior of the reshuffled versions. For larger time delays, we observe a significantly larger correlation in the structural network (between degree and dTE) and also a quite large PA value with respect to the reshuffled matrices.

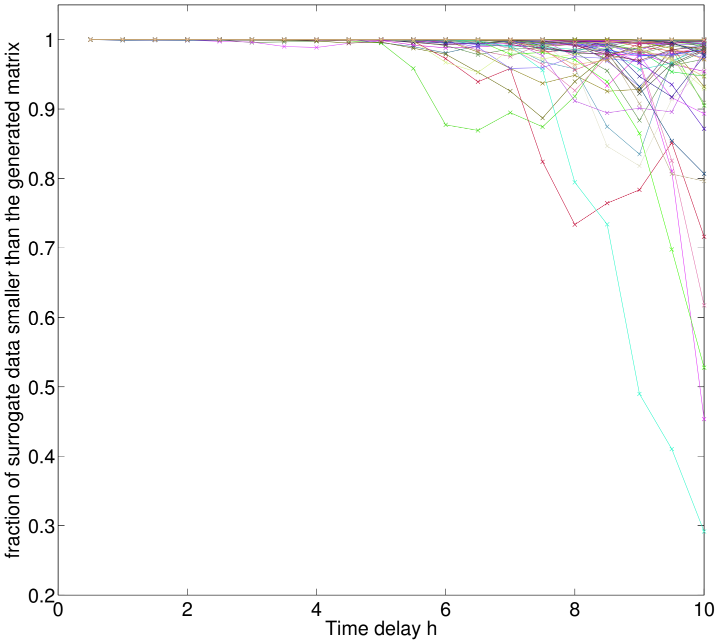

Figure 6.11: **Significant correlation for reshuffled matrices.** For different time delays, fraction of surrogate data possessing a smaller value than the observed PA value and the observed correlation between degree and averaged directed transfer entropy (dTE) value, respectively. When the fraction is above 0.95, the observed value is significantly larger based on the 5% significance level. Up to a certain time delay, all the randomly reshuffled networks exert a significantly positive correlation between degree and directed transfer entropy towards the rest of the network.

ure 6.12. Overall, we observe a positive correlation for the different degrees with the average directed transfer entropy value. However, regarding different time scales, we can see some fluctuations with regard to in- and out-degree. For small time scales, a high out-degree reaches the maximum positive correlation. With regard to longer time scales, the in- and out-degree differences seem to disappear. This result is in line with intuition since for a higher number of (direct) outgoing links one would expect a more sending property of a node (for short time delays). However, the general notion of hubs cannot be extended in a straightforward manner. For the macaque network, nodes with a high sum of in- and out-degrees can have much more incoming than outgoing links or the other way around, which should result in different sending/receiving properties. The different behavior of those nodes is shown by the correlation between the difference of in- and out-degree and the dTE value (purple dots in Figure 6.12). Nodes with a much higher number of incoming than outgoing connections, which can still be hubs related to the overall degree (see Figure 6.15), seem to be more receiving with regard to short time delays but more sending when analyzing longer time delays. We also plotted the out-degree and the difference between in- and out-degree against the dTE values for specific time delays (see Figures 6.13 and 6.14) reaching the maximum and minimum correlation values, respectively.

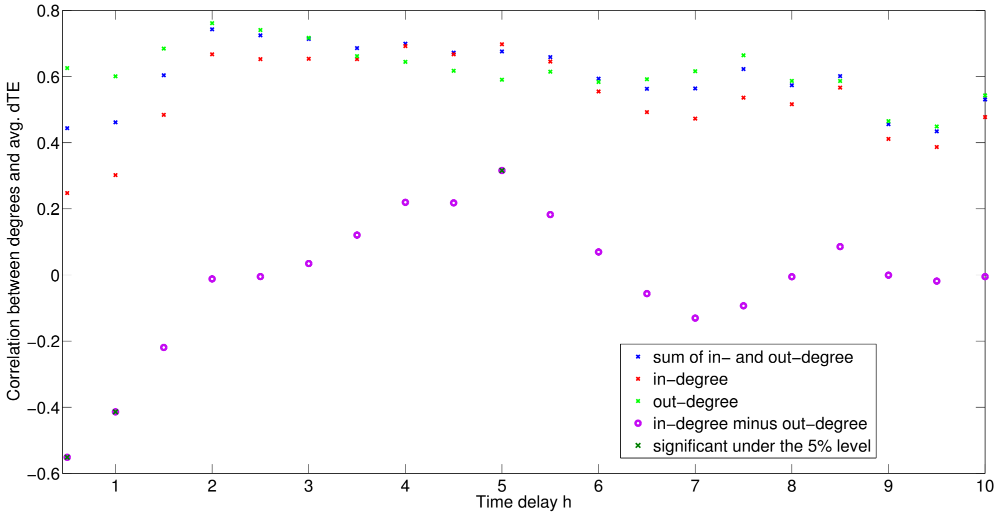

Figure 6.12: **Correlation for macaque brain.** Correlation between different forms of the degree and averaged directed transfer entropy (dTE) over different time delays. For the in-degree, the out-degree and the sum of in- and out-degree the positive correlation values are significant with regard to randomly reshuffled versions of the dTE values. For the difference between in- and out-degree, the three marked points are the only significant correlation values.

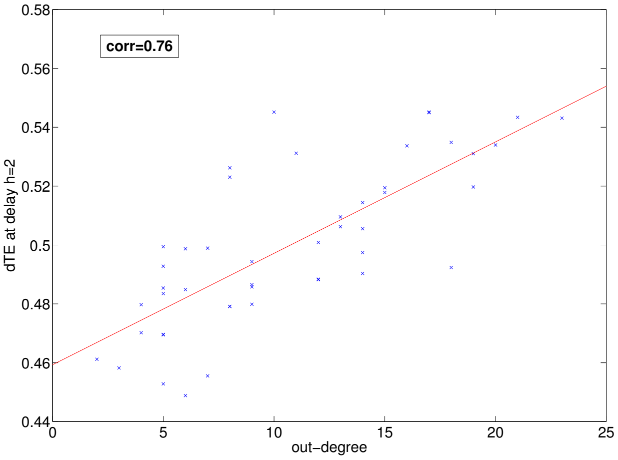

Figure 6.13: **Maximum correlation for macaque brain.** The out-degree for each node in the macaque structural brain network against the directed transfer entropy (dTE) for the time delay $h = 2$ reaching the maximum correlation value.

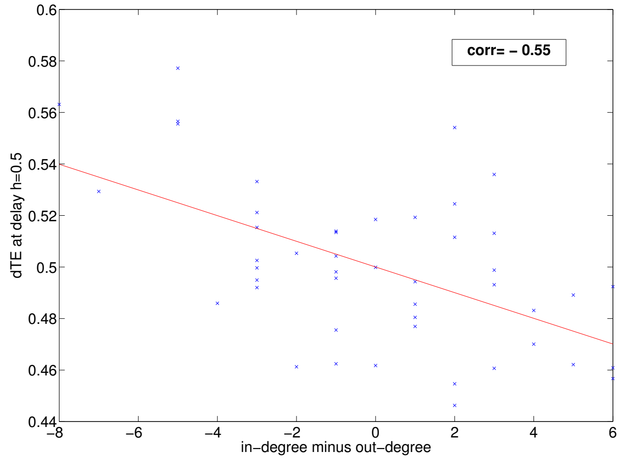

Figure 6.14: **Minimum correlation for macaque brain.** The difference between in- and out-degree for each node in the macaque structural brain network against the directed transfer entropy (dTE) for the time delay $h = 0.5$ reaching the minimum correlation value.

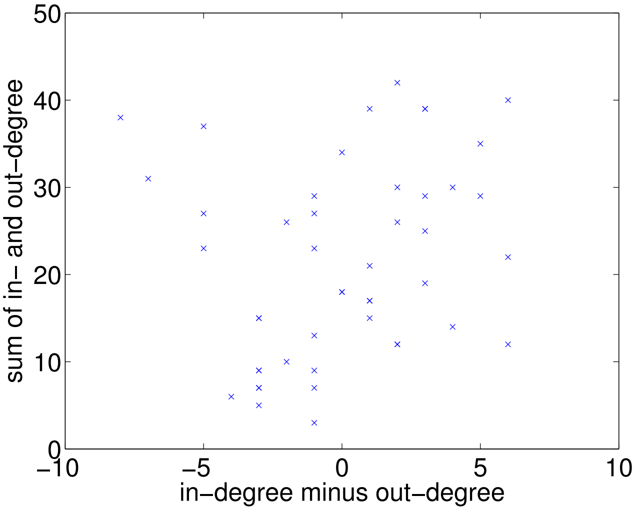

Figure 6.15: **Degrees in the macaque brain.** Sum of in- and out-degree for each node in the macaque structural brain networks versus the difference between in- and out-degree. Some high-degree nodes have big differences in their number of incoming and outgoing links.

6.6.4. CORRELATION VERSUS TRANSFER ENTROPY

The transfer entropy is equal to the conditional mutual information (MI)

$$\begin{aligned}TE_{i\to j}(h) &= MI(X_j(t+h);X_i(t)|X_j(t))\\ &= \sum_{k,l,m=\{0,1\}} \Pr[X_j(t+h)=k,X_j(t)=l,X_i(t)=m]\cdot\log\left(\frac{\Pr[X_j(t+h)=k|X_j(t)=l,X_i(t)=m]}{\Pr[X_j(t+h)=k|X_j(t)=l]}\right)\\ &= \sum_{k,l,m=\{0,1\}} \Pr[X_j(t+h)=k,X_j(t)=l,X_i(t)=m]\cdot\log\left(\frac{\Pr[X_j(t+h)=k,X_j(t)=l,X_i(t)=m]\Pr[X_j(t)]}{\Pr[X_j(t+h)=k,X_j(t)=l]\Pr[X_i(t),X_j(t+h)]}\right),\end{aligned}$$

where we applied the law of Bayes for the last equality.

The mutual information and the measure of correlation want to measure the same underlying property of two random variables, their 'distance to independence'. The covariance is defined as

$$cov(i,j,h)=E[X_i(t)X_j(t+h)]-E[X_i(t)]E[X_j(t+h)]$$

and measures the distance in terms of expected values of the random variables itself whereas the mutual information can be written as

$$MI(X_j(t+h);X_i(t))=E[\log(Pr[X_i(t),X_j(t+h)])]-E[\log(Pr[X_i(t)]Pr[X_j(t+h)])]$$

and measures the distance in terms of the expected value of the logarithm of their probabilities.

For the transfer entropy, we can apply the chain rule of the mutual information and obtain

$$\begin{aligned}TE_{i\to j}(h) &= MI(X_j(t+h);X_i(t)|X_j(t))\\ &= MI(X_j(t+h);X_i(t),X_j(t))-MI(X_j(t+h),X_j(t))\\ &= \sum_{k,l,m=\{0,1\}} \Pr[X_j(t+h)=k,X_j(t)=l,X_i(t)=m]\cdot\log\left(\frac{\Pr[X_j(t+h)=k,X_j(t)=l,X_i(t)=m]}{\Pr[X_j(t+h)]\Pr[X_i(t)=k,X_j(t)=l]}\right)\\ &\quad-\sum_{k,l=\{0,1\}} \Pr[X_j(t+h)=k,X_j(t)=l]\cdot\log\left(\frac{\Pr[X_j(t+h)=k,X_j(t)=l]}{\Pr[X_j(t+h)]\Pr[X_j(t)=l]}\right) \qquad (6.4)\end{aligned}$$

For the second term we followed the derivations in [58] and used that our activation series are binary resulting in an approximative formula

$$MI(X_j(t+h),X_j(t))\approx\frac{1}{2}\left(\frac{auto_j}{Pr[X_j(t)=1](1-Pr[X_j(t)=1])}\right)^2,$$

where $auto_j$ denotes the auto-correlation of j. To reach this result, we did assume that $Pr[X_j(t)=1]\approx Pr[X_j(t+h)=1]$ which could be confirmed by our simulations for small values of the time lag h. Thus, the second term of (6.4) can be interpreted as some correction for the auto-correlation that is included in the transfer entropy.

If we apply the Kirkwood superposition approximation to the first term of (6.4) which involves all three entities, we can approximate the joint probability of the three terms

$$\begin{aligned}MI(X_j(t+h);X_i(t),X_j(t)) = &\sum_{k,l,m=\{0,1\}} \Pr[X_j(t+h)=k,X_j(t)=l,X_i(t)=m]\cdot\\ &\log\left(\frac{\Pr[X_j(t+h)=k,X_j(t)=l]\Pr[X_j(t+h)=k,X_i(t)=l]}{\Pr[X_j(t+h)]^2\Pr[X_i(t)=k]\Pr[X_j(t)=k]}\right)\end{aligned}$$

where e.g. in the case of $k=l=m$ we obtain the element of the sum in the logarithm as

$$\log\left(\frac{\left(auto_j+\Pr[X_j(t)=k]^2\right)}{\Pr[X_j(t)=k]^2}\cdot\frac{\left(corr_{del}(i,j,h)+\Pr[X_j(t)=k]\Pr[X_i(t)=k]\right)}{\Pr[X_j(t)=k]\Pr[X_i(t)=k]}\right)$$

where $corr_{del}(i,j,h)$ is the delayed correlation function between node i and node j which will be further studied in the next section. For the other elements of the sum we can derive similar results in the logarithm reducing the expression to a combination of the auto-correlation of j and the delayed correlation between i

and j. For the three-way joint probability in front of the logarithm, we can again use the Kirkwood superposition approximation and obtain e.g. for the element $k = l = m$

$$\begin{aligned}
&\Pr[X_j(t+h)=1, X_j(t)=1, X_i(t)=1] \\
&\approx \frac{\Pr[X_j(t+h)=1, X_j(t)=1]\Pr[X_j(t+h)=1, X_i(t)=1]\Pr[X_j(t)=1, X_i(t)=1]}{\Pr[X_j(t)=1]\Pr[X_i(t)=1]\Pr[X_j(t)=1]} \\
&= \frac{(auto_j + \Pr[X_j(t)=1]^2)(corr_{del}(i,j,h) + \Pr[X_j(t)=1]\Pr[X_i(t)=1])(corr(i,j) + \Pr[X_j(t)=1]\Pr[X_i(t)=1])}{\Pr[X_j(t)=1]\Pr[X_i(t)=1]\Pr[X_j(t)=1]}
\end{aligned}$$

where $corr(i,j)$ is the correlation (or covariance) of the two nodes' binary time series. For the other elements of the sum, the derivation can be conducted similarly. To sum up, we have demonstrated that the transfer entropy from node i to node j can be expressed as a combination of the (delayed) correlation between i and j corrected for the auto-correlation of j. In the following section, we will further examine analytically the (delayed) correlation and auto-correlation as 'building blocks' of the transfer entropy.

6.6.5. THE COVARIANCE $\widetilde{\rho}\left(X_i(t), X_j(t+h)\right)$ FOR A SMALL TIME LAG h

The functional connectivity between two nodes i and j is defined as the correlation of their activation series

$$\rho(X_i(t), X_j(t)) = \frac{E[X_i(t)X_j(t)] - E[X_i(t)]E[X_j(t)]}{\sqrt{Var[X_i(t)]}\sqrt{Var[X_j(t)]}} \tag{6.5}$$

over the whole simulation time [90].

The numerator is also referred to as the covariance between node i and j. We compute the expectation $E\left[X_i(t)X_j(t+h)\right]$ for a very small time $h > 0$. Although the derivative of a Bernoulli random variable does not exist, we follow the framework in [112] and we agree to *formally* define the derivative by the random variable equation

$$\frac{dX_j(t)}{dt} = -\delta X_j(t) + \left(1 - X_j(t)\right)\beta \sum_{k=1}^{N} a_{kj} X_k(t) \tag{6.6}$$

For small h, the first order expansion of the Taylor series yields

$$X_j(t+h) = X_j(t) + h\frac{dX_j(t)}{dt} + o(h) \tag{6.7}$$

DEDUCTIONS

With the definition (6.5) of the covariance, we find for $i \neq j$ that the j-delayed covariance satisfies

$$\begin{aligned}
\widetilde{\rho}\left(X_i(t), X_j(t+h)\right) = (1 - \delta h)\,\widetilde{\rho}\left(X_i(t), X_j(t)\right) + \beta h \sum_{k=1}^{N} a_{kj} \widetilde{\rho}\left(X_i(t), X_k(t)\right) \\
- \beta h \sum_{k=1}^{N} a_{kj}\left\{E\left[X_i(t)X_j(t)X_k(t)\right] - E\left[X_i(t)\right]E\left[X_j(t)X_k(t)\right]\right\} + o(h)
\end{aligned} \tag{6.8}$$

In general, the j-delayed covariance $\widetilde{\rho}\left(X_i(t), X_j(t+h)\right)$ is different from the i-delayed covariance $\widetilde{\rho}\left(X_j(t), X_i(t+h)\right)$. Indeed, (6.8) demonstrates that

$$\begin{aligned}
\widetilde{\rho}\left(X_i(t), X_j(t+h)\right) - \widetilde{\rho}\left(X_j(t), X_i(t+h)\right) = \beta h \sum_{k=1}^{N}\left(a_{kj}\widetilde{\rho}(X_i(t), X_k(t)) - a_{ki}\widetilde{\rho}(X_j(t), X_k(t))\right) \\
-\beta h \sum_{k=1}^{N}(a_{kj} - a_{ki})E[X_i(t)X_j(t)X_k(t)] - \beta h \sum_{k=1}^{N}\left(a_{kj}E[X_i(t)]E[X_j(t)X_k(t)] - a_{ki}E[X_j(t)]E[X_i(t)X_k(t)]\right)
\end{aligned}$$

Starting from the original definition of $\widetilde{\rho}\left(X_i(t), X_j(t+h)\right)$, we can deduce the parts as

$$\begin{aligned}
E\left[X_i(t)X_j(t+h)\right] &= E\left[X_i(t)X_j(t)\right] + hE\left[-\delta X_j(t)X_i(t) + \left(1 - X_j(t)\right)X_i(t)\beta\sum_{k=1}^{N} a_{kj}X_k(t)\right] + o(h) \\
E\left[X_j(t)X_i(t+h)\right] &= E\left[X_j(t)X_i(t)\right] + hE\left[-\delta X_i(t)X_j(t) + (1 - X_i(t))X_j(t)\beta\sum_{k=1}^{N} a_{ki}X_k(t)\right] + o(h)
\end{aligned}$$

Subtraction yields

$$\begin{aligned}
T &= E\left[X_i(t)X_j(t+h)\right] - E\left[X_j(t)X_i(t+h)\right] \\
&= \beta h E\left[X_i(t)\left(1-X_j(t)\right)\sum_{k=1}^{N} a_{kj}X_k(t) - X_j(t)\left(1-X_i(t)\right)\sum_{k=1}^{N} a_{ki}X_k(t)\right] \\
&= \beta h E\left[X_i(t)\sum_{k=1}^{N} a_{kj}X_k(t) - X_j(t)\sum_{k=1}^{N} a_{ki}X_k(t) + X_i(t)X_j(t)\sum_{k=1}^{N}\left(a_{ki}-a_{kj}\right)X_k(t)\right]
\end{aligned}$$

where $\sum_{k=1}^{N} a_{kj}X_k(t)$ are the infected neighbors of node j. The first equation tells that T is the balance of two cases: either an infection at node i and all infected neighbors of node j try to infect node j or an infection at node j and all infected neighbors of node i try to infect node i.

The other parts of the difference of covariances can be written as

$$\begin{aligned}
E[X_j(t)]E[X_i(t+h)] - E[X_i(t)]E[X_j(t+h)] &= \beta h E[X_j(t)]\sum_{k=1}^{N} a_{ki}E[X_k(t)] - \beta h E[X_i(t)]\sum_{k=1}^{N} a_{kj}E[X_k(t)] \\
&\quad -\beta h\sum_{k=1}^{N} a_{ki}E[X_i(t)X_k(t)]E[X_j(t)] + \beta h\sum_{k=1}^{N} a_{kj}E[X_j(t)X_k(t)]E[X_i(t)]
\end{aligned}$$

Together we get for the probability flux

$$\begin{aligned}
\tilde{\rho}\left(X_i(t),X_j(t+h)\right) - \tilde{\rho}\left(X_j(t),X_i(t+h)\right) &= \beta h\sum_{k=1}^{N} a_{kj}\left(E[X_i(t)]E[X_j(t)X_k(t)] - E[X_i(t)X_j(t)X_k(t)]\right) \\
&\quad -\beta h\sum_{k=1}^{N} a_{ki}\left(E[X_j(t)]E[X_i(t)X_k(t)] - E[X_i(t)X_j(t)X_k(t)]\right)
\end{aligned}$$

This information flow has also been researched by Hillebrand et al. [50], where instead of the delayed correlation, the authors used the *Phase Transfer Entropy* as a measure of causality. This difference in coavariance is positive if and only if the fraction from [50] is larger than 0.5.

JUST ABOVE THE EPIDEMIC THRESHOLD

Just above the epidemic threshold [115], the probability of infection is $E\left[X_i(t)\right] = \epsilon\left(x_1\right)_i$, where $\epsilon > 0$ is small and where x_1 is the principal eigenvector of the adjacency matrix A belonging to the largest eigenvalue λ_1.

Assuming that the effective infection rate $\tau = \frac{\beta}{\delta} = \tau_c + \epsilon$, then we may discard the last sum with triple expectations (of order $O\left(\epsilon^2\right)$) in (6.8) so that

$$\tilde{\rho}\left(X_i(t),X_j(t+h)\right) \approx (1-\delta h)\,\tilde{\rho}\left(X_i(t),X_j(t)\right) + \beta h\sum_{k=1}^{N} a_{kj}\tilde{\rho}\left(X_i(t),X_k(t)\right) + o(h)$$

Since $\tilde{\rho}\left(X_i(t),X_j(t)\right) \geq 0$ and assuming that $\tilde{\rho}\left(X_i(t),X_k(t)\right)$ is of about the same magnitude as $\tilde{\rho}\left(X_i(t),X_j(t)\right)$ for any node k that is a neighbor of j (this is possible because node k as a neighbor of j can only be one hop further away from or nearer to i than j. If i and j are directly connected and k is a common neighbor, then this approximation is even more accurate), then

$$\tilde{\rho}\left(X_i(t),X_j(t+h)\right) \approx \left(1+\left(\tau d_j - 1\right)\delta h\right)\tilde{\rho}\left(X_i(t),X_j(t)\right) + o(h)$$

and

$$\frac{\rho\left(X_i(t),X_j(t+h)\right)}{\rho\left(X_i(t),X_j(t)\right)} \approx \left(1+\left(\tau d_j - 1\right)\delta h\right)\frac{\sqrt{\operatorname{Var}\left[X_j(t)\right]}}{\sqrt{\operatorname{Var}\left[X_j(t+h)\right]}} + o(h)$$

Assuming $\operatorname{Var}\left[X_j(t+h)\right] \approx \operatorname{Var}\left[X_j(t)\right]$ (which is reasonable for small h) the fraction on the right hand side can be approximated by 1 and we obtain

$$\frac{\rho\left(X_i(t),X_j(t+h)\right)}{\rho\left(X_i(t),X_j(t)\right)} \approx 1 + \delta h\left(\tau d_j - 1\right) + o(h)$$

Finally, since $\tau > \tau_c \geq \frac{1}{\lambda_1}$, we have that $\tau d_j - 1 > \frac{d_j}{\lambda_1} - 1$. Since the spectral radius is bounded [111] by $\max\left(d_{av}, \sqrt{d_{\max}}\right) \leq \lambda_1 \leq d_{\max}$, where the average degree $d_{av} = \frac{2L}{N}$, the factor $\tau^* d_j - 1$ is positive for a node j with more than average degree, but possibly negative for a node j with low degree.

7

CONCLUSION

In this dissertation, we developed new and enlarged existing methods from network science in order to apply them to complex brain networks. The aim hereby was to shed some light on the emergence of information flow in the human brain. We summarize the results of this dissertation categorized under the two main research questions.

RESEARCH QUESTION 1: WHAT ARE THE MOST IMPORTANT LINKS AND MOTIFS IN FUNCTIONAL BRAIN NETWORKS WITH RESPECT TO GLOBAL INFORMATION FLOW?

In Chapter 2, we proposed the USPT as a new sampling method for functional brain networks. We showed that, by extracting all the shortest paths, we are able to detect significant differences between MS patients and healthy controls. Moreover, the discovered differences were in line with previous findings on the functional brain networks of patients suffering from MS. Consequently, the shortest paths of the functional brain networks seem to represent important features for the global information flow in the human brain.

In Chapter 3, we proposed a general sampling method for networks based on the USPT. We analyzed this new general α-tree sampling method for different underlying link weight distributions and explored its theoretical properties. With respect to functional brain networks, the general USPT method enables the comparison between individual functional brain networks at different levels of link density. Assuming that the shortest paths are important for the global information flow, the presented α-tree sampling method can further be exploited to rank all the links in a network with respect to their importance for the shortest path structure.

In Chapter 4, we explored the meso-scale of the information flow in brain networks in the form of motifs. Based on different construction methods of the effective connectivity network, we observed a dominant high frequency of the bi-directional two-hop path motif when compared with randomly rewired networks. Thus, the bi-directional two-hop path appears to represent a general building block for the information flow in functional brain networks. This bi-directional 3-motif probably resembles the general organizational principle of segregation and integration. Previous studies also discovered the bi-directional two-hop path in e.g. the macaque structural brain network and brought its occurrence in connection with the presence of hubs. The hubs involved in (many instances of) this motif are interpreted to act as 'bridges' for the information flow. To analyze the intertwined global organization of the bi-directional two-hop path, we applied a recently developed motif-based clustering algorithm. On a global level, a posterior-anterior pattern of information flow has been observed in earlier empirical studies. After performing the motif-based clustering, the posterior hubs seem to play a crucial role to facilitate the communication between posterior and anterior brain regions. Specifically, these posterior hubs are hypothesized to carry out the role of 'bridges' for the information flow not only on the local but also on the global level. Concerning different frequency bands, opposite patterns were stated in previous work with respect to lower and higher frequency band data. We showed that these different empirically observed global patterns seem to arise based on different frequency-dependent interaction patterns between the occipital regions and the frontal lobe.

RESEARCH QUESTION 2: WHICH STRUCTURAL NETWORK PROPERTIES DRIVE THE FUNCTIONAL INTERACTIONS?

In Chapter 5, we approached the relationship between the adjacency matrices of structural and functional brain networks mathematically. As a result, we presented a function that can map the structural onto the functional adjacency matrix and vice versa reaching a relatively high goodness-of-fit level. This mapping was not only shown to provide good approximations for group-averaged data sets but also for individual measurements from different techniques, including fMRI, MEG and DTI. Furthermore, this structure-function mapping incorporates and confirms previous findings in this research field. As an interpretation of this mapping, walks in the structural brain network up to the length of the diameter have the highest influence on a functional connection for fMRI and MEG data. This result points towards the importance of not only the shortest paths for information flow in brain networks but also the inclusion of alternative paths for reasons of robustness and redundancy of the communication (though only up to a certain hopcount). Furthermore, the mapping was found to be modality-dependent in terms of its fitted coefficients, which consequently suggests a general modality-dependency for the structure-function relation in the human brain.

In Chapter 6, we analyzed the outcome of modeling an epidemic spreading model on the human connectome. Based on the undirected underlying human connectome, we were able to replicate the empirically observed global patterns of information flow. Similar to the motif analysis, the posterior hubs have been identified as important influencers of the global information flow. The interconnectivity pattern of the posterior hubs biases the spatial distribution of the structural degree. This unequal spatial distribution of the structural degree seems to be a necessary condition for the emergence of a global directionality of the information flow. Moreover, the hubs seem to act simultaneously as both, strong senders and receivers, though apparently on different time scales. Consequently, the mirrored global directions of information flow, towards these posterior hubs and away from them, could be ascribed to different time scales of the spreading process.

To sum up, as a commonality throughout this dissertation we observed that the densely structurally connected hubs among the posterior brain regions strongly influence the emergence of the global information flow. As a second point, on a local level, the shortest path and also all walks between two brain regions up to the length of the diameter drive their functional interaction.

FUTURE WORK

All of the above approaches have mostly been conducted for healthy controls and could also be applied to patient data to uncover the origins of disruptions for different neurological disorders. When patient data sets become available, modifying the above analyses towards specific brain disorders could be a major part of future work. For example, a heterogeneous SIS model seems likely to explain the outbreak of seizures for epilepsy patients. Furthermore, the general movement towards individualized medicine should motivate tailoring the developed models and frameworks for individual patients. Combining the data of different modalities for one individual should become the focus of future approaches to accelerate the possible benefits for individual patients.

The above models could also be applied to various other networks. For example, the proposed sampling methods in Chapters 2 and 3 are not limited to functional brain networks and could be applied to identify important links with regard to other flows in networks. In the same way, the design of the mapping approach in Chapter 5 is flexible. Applications also in e.g. man-made networks could investigate how disruptions in the structural layer can influence the functional outcome of a system.

The field of brain networks should also continuously benefit from the newest developments in network science. Following current trends in network science, the application possibilities of temporal networks [64] and multilayer frameworks [9] should be exploited in more depth. Analyzing the brain as a multilayer network is still a relatively new approach [97]. Even though the advantages of including more data within one framework are obvious, the avoidance of redundant information needs to be investigated for the multilayer framework in the same way as for the single layers. Additionally, the comparison of multilayer networks is still a general open research question that needs to be answered before this multilayer framework can prove its usefulness for patient data.

ACKNOWLEDGEMENTS

OFFICIAL ACKNOWLEDGEMENTS

DATA

The data used in Chapters 2 till 5 of this dissertation was supported by a private sponsorship to the VUmc MS Center Amsterdam. The VUmc MS Center Amsterdam is sponsored through a program grant by the Dutch MS Research Foundation (grant number 09-358d). We thank Menno Schoonheim for acquisition and post-processing of fMRI data and Prejaas Tewarie for making this data set available to us. For the PTE data in Chapter 4, we additionally thank Matteo Fraschini, Matteo Demuru and Meichen Yu for developing scripts for the processing of the MEG data. Also, we thank Linda Douw for providing us with the individual multimodal data set for Chapter 5. We thank Gaolang Gong for providing structural network data that we used in Chapters 5 and 6.

SOFTWARE

We are grateful to Jure Leskovec, who made his code for the motif-based clustering publicly available as part of the SNAP framework that we applied in Chapter 4. Further, we thank Ruud van de Bovenkamp for his useful comments and for making his SIS simulator available to us to gain the results in Chapter 6.

UNOFFICIAL ACKNOWLEDGEMENTS

First of all, I would like to thank my promotor Piet especially for his (sometimes way too) fast reactions to new drafts and always making time for long discussions. Though we might have not agreed on many topics, when it came to research I always felt that we shared the same high standards and mathematics as a common language. Thanks also for accepting me for being different than most of your previous PhD students and allowing me to get involved with many other things next to my research like e.g. teaching.

Applying network science to a complex field like neuroscience needs an expert who is patiently explaining and at the same time broadly interested and open to new approaches. Luckily I found exactly this person in my promotor Kees! Already after my first interview day at the VUmc, the importance of the field of complex brain networks became not only very obvious to me but also filled my motivation for the whole four years. Thanks Kees for the continuous guidance through the neuroscience world and all your help with the interpretation of our often very mathematical results!

Next to my promotors, there was one person without whom I would have surely been frustrated with interdisciplinary research very soon and who always (even though he was half of the time physically not in the Netherlands anymore) was there for all of my questions. Because of this special person the bridge between my mathematical background and the application to neuroscience was only possible to exist: Prejaas, thank you so much for keeping my hopes up when coauthors with many different backgrounds had many different critical suggestions to improve our papers and thanks for the fast reactions to thousands of my e-mails!

Thanks also to Huijuan Wang for helping me to settle in as my daily supervisor during the first 9 months and also thank you for keeping the connection open and continuing to give me good advice over the whole course of my PhD!

There were many more people from the VU who were involved in many (Monday morning) discussions and who helped me to improve many of my articles, special thanks here goes to Arjan, Bob, Linda and Meichen!

Special thanks to the best master student ever who kept busy even long after obtaining her degree and moving to Seattle: Candy, I wish you all the best!

Thanks to Marcus for improving my writing and being the most efficient coauthor I ever had the pleasure working with!

Special thanks for very good advice and relaxed 'Feierabend' beers to Norbert, Niels and Ruud!

Thanks also to the rest of my current and former NAS colleagues for being always helpful with respect to many different questions: Evangelos, Martijn, Aleksandar, Negar, Karel, Songwei, Stojan, Xavi, Annalisa, Song, Farabi, Rogier, Ebisa, Cong, Edgar, Nico, Fernando, Rani, Marloes, Wendy, Christian, Hale, Dongchao, Wynand, Xiangrong, Zhidong, Qiang, Luxing, Chuan, Yakup, Shruti, Bo, Rob and Remco.

There are a few people who were not involved with my research at all but who guided me through other equally important learning processes: Thanks for being my mentor, Mathijs de Weerdt! Thanks to Catholijn for pointing me in the right direction! And a special thanks here goes to Saskia de Vries for the communication coaching!

Ann-Sophie: thanks for way too long coffee- and lunch-breaks filled with way too many words about everything but our actual research! Introducing us was probably the greatest thing that the Graduate School did for me!

Yannick: You are the one person who keeps pushing and challenging me always encouraging that I can do more. Your working style especially during your master thesis but also when it comes to language learning has always been an inspiration to me! I hope our paths will cross again and again in different cities around the globe!

Bedankt ook aan mijn nieuwe Nederlandse familie! Door jullie voel ik me hier in Nederland nog een stukje meer thuis! Bedankt, Kees, voor je hulp bij alle Nederlandse vertalingen! Bedankt, Jasper, voor het mooie cover design!

Tom, even though you were most of the time thousands of kilometers away, for the last three years you have been on my mind as my favorite distraction. Thanks for your constant "alles komt goed" encouragement, your people-management advice and for being the chaos in my order!

Lastly, a few words to my family: Danke liebe Familie, dass ihr akzeptiert habt, dass ich nicht bei der Landessparkasse zu Oldenburg arbeite, und mich immer unterstützt habt bei meinem sehr anderen Weg! Eure Besuche aber noch viel mehr eure Stimmen am Telefon haben mir seit meinem Umzug nach München vor 10 Jahren ein Gefühl von zuhause gegeben, wo immer ich gerade war!

REFERENCES

[1] Abdelnour, F., Voss, H. U., and Raj, A. (2014). Network diffusion accurately models the relationship between structural and functional brain connectivity networks. *NeuroImage*, 90:335–347.

[2] Aertsen, A., Gerstein, G., Habib, M., and Palm, G. (1989). Dynamics of neuronal firing correlation: modulation of "effective connectivity". *Journal of Neurophysiology*, 61(5):900–917.

[3] Alexander-Bloch, A. F., Vértes, P. E., Stidd, R., Lalonde, F., Clasen, L., Rapoport, J., Giedd, J., Bullmore, E. T., and Gogtay, N. (2013). The anatomical distance of functional connections predicts brain network topology in health and schizophrenia. *Cerebral Cortex*, 23(1):127–138.

[4] Bastos, A. M., Vezoli, J., Bosman, C. A., Schoffelen, J.-M., Oostenveld, R., Dowdall, J. R., De Weerd, P., Kennedy, H., and Fries, P. (2015). Visual areas exert feedforward and feedback influences through distinct frequency channels. *Neuron*, 85(2):390–401.

[5] Battaglia, D., Witt, A., Wolf, F., and Geisel, T. (2012). Dynamic effective connectivity of inter-areal brain circuits. *PLoS Computational Biololgy*, 8(3):e1002438.

[6] Battiston, F., Nicosia, V., Chavez, M., and Latora, V. (2017). Multilayer motif analysis of brain networks. *Chaos: An Interdisciplinary Journal of Nonlinear Science*, 27(4):047404.

[7] Benson, A. R., Gleich, D. F., and Leskovec, J. (2016). Higher-order organization of complex networks. *Science*, 353(6295):163–166.

[8] Betzel, R. F., Griffa, A., Avena-Koenigsberger, A., Goñi, J., Thiran, J.-P., Hagmann, P., and Sporns, O. (2013). Multi-scale community organization of the human structural connectome and its relationship with resting-state functional connectivity. *Network Science*, 1(03):353–373.

[9] Boccaletti, S., Bianconi, G., Criado, R., Del Genio, C. I., Gómez-Gardenes, J., Romance, M., Sendina-Nadal, I., Wang, Z., and Zanin, M. (2014). The structure and dynamics of multilayer networks. *Physics Reports*, 544(1):1–122.

[10] Braun, U., Muldoon, S. F., and Bassett, D. S. (2015). On human brain networks in health and disease. *eLS*.

[11] Braunstein, L. A., Wu, Z., Chen, Y., Buldyrev, S. V., Kalisky, T., Sreenivasan, S., Cohen, R., Lopez, E., Havlin, S., and Stanley, H. E. (2007). Optimal path and minimal spanning trees in random weighted networks. *International Journal of Bifurcation and Chaos*, 17(07):2215–2255.

[12] Brookes, M. J., Woolrich, M., Luckhoo, H., Price, D., Hale, J. R., Stephenson, M. C., Barnes, G. R., Smith, S. M., and Morris, P. G. (2011). Investigating the electrophysiological basis of resting state networks using magnetoencephalography. *Proceedings of the National Academy of Sciences*, 108(40):16783–16788.

[13] Buckner, R. L., Andrews-Hanna, J. R., and Schacter, D. L. (2008). The brain's default network. *Annals of the New York Academy of Sciences*, 1124(1):1–38.

[14] Bullmore, E. and Sporns, O. (2009). Complex brain networks: graph theoretical analysis of structural and functional systems. *Nature Reviews Neuroscience*, 10(3):186–198.

[15] Bullmore, E. and Sporns, O. (2012). The economy of brain network organization. *Nature Reviews Neuroscience*, 13(5):336–349.

[16] Cator, E. and Van Mieghem, P. (2013). Susceptible-infected-susceptible epidemics on the complete graph and the star graph: Exact analysis. *Physical Review E*, 87(1):012811.

[17] Crossley, N. A., Mechelli, A., Scott, J., Carletti, F., Fox, P. T., McGuire, P., and Bullmore, E. T. (2014). The hubs of the human connectome are generally implicated in the anatomy of brain disorders. *Brain*, 137(8):2382–2395.

[18] Daducci, A., Gerhard, S., Griffa, A., Lemkaddem, A., Cammoun, L., Gigandet, X., Meuli, R., Hagmann, P., and Thiran, J.-P. (2012). The connectome mapper: an open-source processing pipeline to map connectomes with MRI. *PloS One*, 7(12):e48121.

[19] Damoiseaux, J. S. and Greicius, M. D. (2009). Greater than the sum of its parts: a review of studies combining structural connectivity and resting-state functional connectivity. *Brain Structure and Function*, 213(6):525–533.

[20] Dauwan, M., van Dellen, E., van Boxtel, L., van Straaten, E. C., de Waal, H., Lemstra, A. W., Gouw, A. A., van der Flier, W. M., Scheltens, P., Sommer, I. E., et al. (2016). EEG-directed connectivity from posterior brain regions is decreased in dementia with Lewy bodies: a comparison with Alzheimer's disease and controls. *Neurobiology of Aging*, 41:122–129.

[21] de Haan, W., Mott, K., van Straaten, E. C., Scheltens, P., and Stam, C. J. (2012). Activity dependent degeneration explains hub vulnerability in Alzheimer's disease. *PLoS Computational Biology*, 8(8):e1002582.

[22] Deco, G., Jirsa, V. K., Robinson, P. A., Breakspear, M., and Friston, K. (2008). The dynamic brain: from spiking neurons to neural masses and cortical fields. *PLoS Computational Biology*, 4(8):e1000092.

[23] Deco, G., McIntosh, A. R., Shen, K., Hutchison, R. M., Menon, R. S., Everling, S., Hagmann, P., and Jirsa, V. K. (2014). Identification of optimal structural connectivity using functional connectivity and neural modeling. *The Journal of Neuroscience*, 34(23):7910–7916.

[24] Deco, G., Senden, M., and Jirsa, V. (2012). How anatomy shapes dynamics: a semi-analytical study of the brain at rest by a simple spin model. *Frontiers in Computational Neuroscience*, 6:68.

[25] Delvenne, J.-C., Yaliraki, S. N., and Barahona, M. (2010). Stability of graph communities across time scales. *Proceedings of the National Academy of Sciences*, 107(29):12755–12760.

[26] Deng, B., Deng, Y., Yu, H., Guo, X., and Wang, J. (2016). Dependence of inter-neuronal effective connectivity on synchrony dynamics in neuronal network motifs. *Chaos, Solitons & Fractals*, 82:48–59.

[27] Douw, L., DeSalvo, M. N., Tanaka, N., Cole, A. J., Liu, H., Reinsberger, C., and Stufflebeam, S. M. (2015). Dissociated multimodal hubs and seizures in temporal lobe epilepsy. *Annals of Clinical and Translational Neurology*, 2(4):338–352.

[28] Dubbelink, K. T. O., Hillebrand, A., Stoffers, D., Deijen, J. B., Twisk, J. W., Stam, C. J., and Berendse, H. W. (2014). Disrupted brain network topology in parkinson's disease: a longitudinal magnetoencephalography study. *Brain*, 137(1):197–207.

[29] Edelman, G. M. and Gally, J. A. (2013). Reentry: a key mechanism for integration of brain function. *Frontiers in Integrative Neuroscience*, 7:63.

[30] Emmons, S., Kobourov, S., Gallant, M., and Börner, K. (2016). Analysis of network clustering algorithms and cluster quality metrics at scale. *PloS One*, 11(7):e0159161.

[31] Fiedler, M. (1973). Algebraic connectivity of graphs. *Czechoslovak Mathematical Journal*, 23(2):298–305.

[32] Fischl, B., Sereno, M. I., and Dale, A. M. (1999). Cortical surface-based analysis: II: Inflation, flattening, and a surface-based coordinate system. *NeuroImage*, 9(2):195–207.

[33] Frey, J. N., Ruhnau, P., and Weisz, N. (2015). Not so different after all: The same oscillatory processes support different types of attention. *Brain Research*, 1626:183–197.

[34] Friedman, E. J., Young, K., Tremper, G., Liang, J., Landsberg, A. S., Schuff, N., Initiative, A. D. N., et al. (2015). Directed network motifs in Alzheimer's disease and mild cognitive impairment. *PloS One*, 10(4):e0124453.

[35] Friston, K. J. (1994). Functional and effective connectivity in neuroimaging: a synthesis. *Human Brain Mapping*, 2(1-2):56–78.

[36] Garey, M. R. and Johnson, D. S. (2002). *Computers and Intractability*, volume 29. W.H. Freeman and Company, New York.

[37] Gerhard, S., Daducci, A., Lemkaddem, A., Meuli, R., Thiran, J.-P., and Hagmann, P. (2011). The connectome viewer toolkit: an open source framework to manage, analyze, and visualize connectomes. *Frontiers in Neuroinformatics*, 5(3).

[38] Gollo, L. L., Zalesky, A., Hutchison, R. M., van den Heuvel, M., and Breakspear, M. (2015). Dwelling quietly in the rich club: brain network determinants of slow cortical fluctuations. *Phil. Trans. R. Soc. B*, 370(1668):20140165.

[39] Golub, G. H. and Loan, C. F. V. (1996). *Matrix Computations*. The John Hopkins University Press, Baltimore, third edition.

[40] Gong, G., He, Y., Concha, L., Lebel, C., Gross, D. W., Evans, A. C., and Beaulieu, C. (2009). Mapping anatomical connectivity patterns of human cerebral cortex using in vivo diffusion tensor imaging tractography. *Cerebral Cortex*, 19(3):524–536.

[41] Goñi, J., van den Heuvel, M. P., Avena-Koenigsberger, A., de Mendizabal, N. V., Betzel, R. F., Griffa, A., Hagmann, P., Corominas-Murtra, B., Thiran, J.-P., and Sporns, O. (2014). Resting-brain functional connectivity predicted by analytic measures of network communication. *Proceedings of the National Academy of Sciences*, 111(2):833–838.

[42] Hagmann, P., Cammoun, L., Gigandet, X., Meuli, R., Honey, C. J., Wedeen, V. J., and Sporns, O. (2008). Mapping the structural core of human cerebral cortex. *PLoS Biology*, 6(7):e159.

[43] Hahs, D. W. and Pethel, S. D. (2011). Distinguishing anticipation from causality: anticipatory bias in the estimation of information flow. *Physical Review Letters*, 107(12):128701.

[44] Haimovici, A., Tagliazucchi, E., Balenzuela, P., and Chialvo, D. R. (2013). Brain organization into resting state networks emerges at criticality on a model of the human connectome. *Physical Review Letters*, 110(17):178101.

[45] Hämäläinen, M. S. and Ilmoniemi, R. (1994). Interpreting magnetic fields of the brain: minimum norm estimates. *Medical & Biological Engineering & Computing*, 32(1):35–42.

[46] Hämäläinen, M. S. and Sarvas, J. (1987). Feasibility of the homogeneous head model in the interpretation of neuromagnetic fields. *Physics in Medicine and Biology*, 32(1):91.

[47] Hermundstad, A. M., Bassett, D. S., Brown, K. S., Aminoff, E. M., Clewett, D., Freeman, S., Frithsen, A., Johnson, A., Tipper, C. M., Miller, M. B., Grafton, S., and Carlson, J. (2013). Structural foundations of resting-state and task-based functional connectivity in the human brain. *Proceedings of the National Academy of Sciences*, 110(15):6169–6174.

[48] Higham, N. J. (2008). *Functions of matrices: theory and computation*. Siam.

[49] Hillebrand, A., Barnes, G. R., Bosboom, J. L., Berendse, H. W., and Stam, C. J. (2012). Frequency-dependent functional connectivity within resting-state networks: an atlas-based MEG beamformer solution. *NeuroImage*, 59(4):3909–3921.

[50] Hillebrand, A., Tewarie, P., van Dellen, E., Yu, M., Carbo, E. W., Douw, L., Gouw, A. A., van Straaten, E. C., and Stam, C. J. (2016). Direction of information flow in large-scale resting-state networks is frequency-dependent. *Proceedings of the National Academy of Sciences*, 113(14):3867–3872.

[51] Honey, C., Sporns, O., Cammoun, L., Gigandet, X., Thiran, J.-P., Meuli, R., and Hagmann, P. (2009). Predicting human resting-state functional connectivity from structural connectivity. *Proceedings of the National Academy of Sciences*, 106(6):2035–2040.

[52] Honey, C. J., Kötter, R., Breakspear, M., and Sporns, O. (2007). Network structure of cerebral cortex shapes functional connectivity on multiple time scales. *Proceedings of the National Academy of Sciences*, 104(24):10240–10245.

[53] Jensen, P., Morini, M., Marton, K., Venturini, T., Vespignani, A., Jacomy, M., Cointet, J.-P., Merckle, P., and Fleury, E. (2016). Detecting global bridges in networks. *Journal of Complex Networks*, 4:319–329.

[54] Kashtan, N., Itzkovitz, S., Milo, R., and Alon, U. (2002). Mfinder tool guide. *Department of Molecular Cell Biology and Computer Science and Applied Mathematics, Weizmann Institute of Science, Rehovot Israel, Tech Rep.*

[55] Leaver, A. M., Van Lare, J., Zielinski, B., Halpern, A. R., and Rauschecker, J. P. (2009). Brain activation during anticipation of sound sequences. *The Journal of Neuroscience*, 29(8):2477–2485.

[56] Leskovec, J. and Sosič, R. (2016). Snap: A general-purpose network analysis and graph-mining library. *ACM Transactions on Intelligent Systems and Technology (TIST)*, 8(1):1.

[57] Li, C., Wang, H., and Van Mieghem, P. (2013). Epidemic threshold in directed networks. *Physical Review E*, 88(6):062802.

[58] Li, W. (1990). Mutual information functions versus correlation functions. *Journal of Statistical Physics*, 60(5-6):823–837.

[59] Liu, Q. and Van Mieghem, P. (2016). Die-out probability in SIS epidemic processes on networks. In *International Workshop on Complex Networks and their Applications*, pages 511–521. Springer.

[60] Liu, Q. and Van Mieghem, P. (2017). Evaluation of an analytic, approximate formula for the time-varying SIS prevalence in different networks. *Physica A: Statistical Mechanics and its Applications*, 471:325–336.

[61] Lobier, M., Siebenhühner, F., Palva, S., and Palva, J. M. (2014). Phase transfer entropy: a novel phase-based measure for directed connectivity in networks coupled by oscillatory interactions. *NeuroImage*, 85:853–872.

[62] Markushevich, A. I. (1985). *Theory of functions of a complex variable, volume I – III.* Chelsea Publishing Company, New York.

[63] Maslov, S. and Sneppen, K. (2002). Specificity and stability in topology of protein networks. *Science*, 296(5569):910–913.

[64] Masuda, N. and Lambiotte, R. (2016). *A guide to temporal networks*, volume 4. World Scientific.

[65] Matias, F. S., Gollo, L. L., Carelli, P. V., Bressler, S. L., Copelli, M., and Mirasso, C. R. (2014). Modeling positive Granger causality and negative phase lag between cortical areas. *NeuroImage*, 99:411–418.

[66] Messé, A., Rudrauf, D., Benali, H., and Marrelec, G. (2014). Relating structure and function in the human brain: Relative contributions of anatomy, stationary dynamics, and non-stationarities. *PLoS Computational Biology*, 10(3):e1003530.

[67] Milo, R., Kashtan, N., Itzkovitz, S., Newman, M. E., and Alon, U. (2003). Uniform generation of random graphs with arbitrary degree sequences. *arXiv preprint cond-mat/0312028*, 106:1–4.

[68] Milo, R., Shen-Orr, S., Itzkovitz, S., Kashtan, N., Chklovskii, D., and Alon, U. (2002). Network motifs: simple building blocks of complex networks. *Science*, 298(5594):824–827.

[69] Mišić, B., Betzel, R. F., Nematzadeh, A., Goñi, J., Griffa, A., Hagmann, P., Flammini, A., Ahn, Y.-Y., and Sporns, O. (2015). Cooperative and competitive spreading dynamics on the human connectome. *Neuron*, 86(6):1518–1529.

[70] Moon, J.-Y., Lee, U., Blain-Moraes, S., and Mashour, G. A. (2015). General relationship of global topology, local dynamics, and directionality in large-scale brain networks. *PLoS Computational Biology*, 11(4):e1004225.

[71] Newman, M. (2010). *Networks: an Introduction.* Oxford University Press Inc., New York, United States.

[72] Newman, M., Barabasi, A.-L., and Watts, D. J. (2011). *The structure and dynamics of networks.* Princeton University Press.

[73] Newman, M. E. (2003). The structure and function of complex networks. *SIAM Review*, 45(2):167–256.

[74] Paluš, M. and Stefanovska, A. (2003). Direction of coupling from phases of interacting oscillators: an information-theoretic approach. *Physical Review E*, 67(5):055201.

[75] Pastor-Satorras, R., Castellano, C., Van Mieghem, P., and Vespignani, A. (2015). Epidemic processes in complex networks. *Reviews of Modern Physics*, 87(3):925.

[76] Price, C. J. and Friston, K. J. (2002). Degeneracy and cognitive anatomy. *Trends in Cognitive Sciences*, 6(10):416–421.

[77] Robinson, P. (2012). Interrelating anatomical, effective, and functional brain connectivity using propagators and neural field theory. *Physical Review E*, 85(1):011912.

[78] Robinson, P., Sarkar, S., Pandejee, G., and Henderson, J. (2014). Determination of effective brain connectivity from functional connectivity with application to resting state connectivities. *Physical Review E*, 90(1):012707.

[79] Rosenblum, M., Pikovsky, A., Kurths, J., Schäfer, C., and Tass, P. A. (2001). Phase synchronization: from theory to data analysis. *Handbook of Biological Physics*, 4:279–321.

[80] Rubinov, M., Sporns, O., Thivierge, J.-P., and Breakspear, M. (2011). Neurobiologically realistic determinants of self-organized criticality in networks of spiking neurons. *PLoS Computational Biology*, 7(6):e1002038.

[81] Sarkar, S., Chawla, S., and Xu, D. (2015). On inferring structural connectivity from brain functional-MRI data. *arXiv preprint arXiv:1502.06659*.

[82] Schreiber, T. (2000). Measuring information transfer. *Physical Review Letters*, 85(2):461.

[83] Senden, M., Deco, G., de Reus, M. A., Goebel, R., and van den Heuvel, M. P. (2014). Rich club organization supports a diverse set of functional network configurations. *NeuroImage*, 96:174–182.

[84] Sirota, A., Montgomery, S., Fujisawa, S., Isomura, Y., Zugaro, M., and Buzsáki, G. (2008). Entrainment of neocortical neurons and gamma oscillations by the hippocampal theta rhythm. *Neuron*, 60(4):683–697.

[85] Skudlarski, P., Jagannathan, K., Calhoun, V. D., Hampson, M., Skudlarska, B. A., and Pearlson, G. (2008). Measuring brain connectivity: diffusion tensor imaging validates resting state temporal correlations. *NeuroImage*, 43(3):554–561.

[86] Sporns, O., Chialvo, D. R., Kaiser, M., and Hilgetag, C. C. (2004). Organization, development and function of complex brain networks. *Trends in Cognitive Sciences*, 8(9):418–425.

[87] Sporns, O., Honey, C. J., and Kötter, R. (2007). Identification and classification of hubs in brain networks. *PloS One*, 2(10):e1049.

[88] Sporns, O. and Kötter, R. (2004). Motifs in brain networks. *PLoS Biol*, 2(11):e369.

[89] Stam, C. J. (2014). Modern network science of neurological disorders. *Nature Reviews Neuroscience*, 15(10):683–695.

[90] Stam, C. J., Hillebrand, A., van Dellen, E., Meier, J., Tewarie, P., van Straaten, E., and Van Mieghem, P. (2016). The relation between structural and functional connectivity patterns in complex brain networks. *International Journal of Psychophysiology*, 103(5):149–160.

[91] Stam, C. J., Nolte, G., and Daffertshofer, A. (2007). Phase lag index: assessment of functional connectivity from multi-channel EEG and MEG with diminished bias from common sources. *Human Brain Mapping*, 28(11):1178–1193.

[92] Stam, C. J., Tewarie, P., Van Dellen, E., van Straaten, E., Hillebrand, A., and Van Mieghem, P. (2014). The trees and the forest: Characterization of complex brain networks with minimum spanning trees. *International Journal of Psychophysiology*, 92(3):129–138.

[93] Stam, C. J. and Van Straaten, E. (2012). The organization of physiological brain networks. *Clinical Neurophysiology*, 123(6):1067–1087.

[94] Stam, C. J. and van Straaten, E. C. (2012). Go with the flow: use of a directed phase lag index (dPLI) to characterize patterns of phase relations in a large-scale model of brain dynamics. *NeuroImage*, 62(3):1415–1428.

[95] Tagliazucchi, E., Chialvo, D. R., Siniatchkin, M., Amico, E., Brichant, J.-F., Bonhomme, V., Noirhomme, Q., Laufs, H., and Laureys, S. (2016). Large-scale signatures of unconsciousness are consistent with a departure from critical dynamics. *Journal of The Royal Society Interface*, 13(114):20151027.

[96] Tewarie, P., Hillebrand, A., van Dellen, E., Schoonheim, M., Barkhof, F., Polman, C., Beaulieu, C., Gong, G., van Dijk, B., and Stam, C. (2014a). Structural degree predicts functional network connectivity: A multimodal resting-state fMRI and MEG study. *NeuroImage*, 97:296–307.

[97] Tewarie, P., Hillebrand, A., van Dijk, B. W., Stam, C. J., O'Neill, G. C., Van Mieghem, P., Meier, J. M., Woolrich, M. W., Morris, P. G., and Brookes, M. J. (2016). Integrating cross-frequency and within band functional networks in resting-state MEG: A multi-layer network approach. *NeuroImage*, 142:324–336.

[98] Tewarie, P., Schoonheim, M. M., Schouten, D. I., Polman, C. H., Balk, L. J., Uitdehaag, B. M., Geurts, J. J., Hillebrand, A., Barkhof, F., and Stam, C. J. (2015). Functional brain networks: linking thalamic atrophy to clinical disability in multiple sclerosis, a multimodal fMRI and MEG study. *Human Brain Mapping*, 36(2):603–618.

[99] Tewarie, P., Steenwijk, M., Tijms, B., Daams, M., Balk, L., Stam, C., Uitdehaag, B., Polman, C., Barkhof, F., Pouwels, P., Vrenken, H., and Hillebrand, A. (2014b). Disruption of structural and functional networks in long-standing multiple sclerosis. *Human Brain Mapping*, 35(12):5946–5961.

[100] Thomas, C., Frank, Q. Y., Irfanoglu, M. O., Modi, P., Saleem, K. S., Leopold, D. A., and Pierpaoli, C. (2014). Anatomical accuracy of brain connections derived from diffusion MRI tractography is inherently limited. *Proceedings of the National Academy of Sciences*, 111(46):16574–16579.

[101] Titchmarsh, E. C. (1964). *The Theory of Functions*. Oxford University Press, Amen House, London.

[102] Ton, R., Deco, G., and Daffertshofer, A. (2014). Structure-function discrepancy: inhomogeneity and delays in synchronized neural networks. *PLoS Computational Biology*, 10(7):e1003736.

[103] Tononi, G., Edelman, G. M., and Sporns, O. (1998). Complexity and coherency: integrating information in the brain. *Trends in Cognitive Sciences*, 2(12):474–484.

[104] Tzourio-Mazoyer, N., Landeau, B., Papathanassiou, D., Crivello, F., Etard, O., Delcroix, N., Mazoyer, B., and Joliot, M. (2002). Automated anatomical labeling of activations in spm using a macroscopic anatomical parcellation of the mni mri single-subject brain. *NeuroImage*, 15(1):273–289.

[105] van de Bovenkamp, R. (2015). *Epidemic Processes on Complex Networks: Modelling, Simulation and Algorithms*. PhD thesis, TU Delft.

[106] van Dellen, E., Douw, L., Hillebrand, A., de Witt Hamer, P. C., Baayen, J. C., Heimans, J. J., Reijneveld, J. C., and Stam, C. J. (2014). Epilepsy surgery outcome and functional network alterations in longitudinal MEG: A minimum spanning tree analysis. *NeuroImage*, 86:354–363.

[107] van den Heuvel, M. P., Kahn, R. S., Goñi, J., and Sporns, O. (2012). High-cost, high-capacity backbone for global brain communication. *Proceedings of the National Academy of Sciences*, 109(28):11372–11377.

[108] van den Heuvel, M. P., Mandl, R. C., Kahn, R. S., Pol, H., and Hilleke, E. (2009). Functionally linked resting-state networks reflect the underlying structural connectivity architecture of the human brain. *Human Brain Mapping*, 30(10):3127–3141.

[109] Van Kerkoerle, T., Self, M. W., Dagnino, B., Gariel-Mathis, M.-A., Poort, J., Van Der Togt, C., and Roelfsema, P. R. (2014). Alpha and gamma oscillations characterize feedback and feedforward processing in monkey visual cortex. *Proceedings of the National Academy of Sciences*, 111(40):14332–14341.

[110] Van Mieghem, P. (2011a). *Data Communications Networking*. Delft University of Technology.

[111] Van Mieghem, P. (2011b). *Graph Spectra for Complex Networks*. Cambridge University Press.

[112] Van Mieghem, P. (2014a). Exact Markovian SIR and SIS epidemics on networks and an upper bound for the epidemic threshold. *arXiv preprint arXiv:1402.1731*.

[113] Van Mieghem, P. (2014b). *Performance Analysis of Complex Networks and Systems*. Cambridge University Press.

[114] Van Mieghem, P. and Magdalena, S. M. (2005). Phase transition in the link weight structure of networks. *Physical Review E*, 72(5):056138.

[115] Van Mieghem, P., Omic, J., and Kooij, R. (2009). Virus spread in networks. *IEEE/ACM Transactions on Networking*, 17(1):1–14.

[116] Van Mieghem, P. and van Langen, S. (2005). Influence of the link weight structure on the shortest path. *Physical Review E*, 71(5):056113.

[117] Van Mieghem, P. and Wang, H. (2009). The observable part of a network. *IEEE/ACM Transactions on Networking*, 17(1):93–105.

[118] van Wijk, B. C., Stam, C. J., and Daffertshofer, A. (2010). Comparing brain networks of different size and connectivity density using graph theory. *PLoS One*, 5(10):e13701.

[119] Vértes, P. E., Alexander-Bloch, A. F., Gogtay, N., Giedd, J. N., Rapoport, J. L., and Bullmore, E. T. (2012). Simple models of human brain functional networks. *Proceedings of the National Academy of Sciences*, 109(15):5868–5873.

[120] Von Luxburg, U. (2007). A tutorial on spectral clustering. *Statistics and Computing*, 17(4):395–416.

[121] Wang, H., Douw, L., Hernandez, J. M., Reijneveld, J., Stam, C., and Van Mieghem, P. (2010). Effect of tumor resection on the characteristics of functional brain networks. *Physical Review E*, 82(2):021924.

[122] Wang, H., Hernandez, J. M., and Van Mieghem, P. (2008). Betweenness centrality in a weighted network. *Physical Review E*, 77(4):046105.

[123] Wang, H. and Van Mieghem, P. (2010). Sampling networks by the union of m shortest path trees. *Computer Networks*, 54:1042–1053.

[124] Whittaker, E. T. and Watson, G. N. (1996). *A Course of Modern Analysis*. Cambridge University Press, Cambridge, UK, cambridge mathematical library edition.

[125] Wiener, N. (1956). The theory of prediction. *Modern Mathematics for Engineers*, 1:125–139.

[126] Wu, Z., Braunstein, L. A., Havlin, S., and Stanley, H. E. (2006). Transport in weighted networks: partition into superhighways and roads. *Physical Review Letters*, 96(14):148702.

[127] Yu, S., Yang, H., Shriki, O., and Plenz, D. (2013). Universal organization of resting brain activity at the thermodynamic critical point. *Frontiers in Systems Neuroscience*, 7.

[128] Zamora-López, G., Chen, Y., Deco, G., Kringelbach, M. L., and Zhou, C. (2016). Functional complexity emerging from anatomical constraints in the brain: the significance of network modularity and rich-clubs. *arXiv preprint arXiv:1602.07625*.

[129] Zhigulin, V. P. (2004). Dynamical motifs: building blocks of complex dynamics in sparsely connected random networks. *Physical Review Letters*, 92(23):238701.

CURRICULUM VITÆ

Jil Mona MEIER

15-12-1989	Born in Bremen, Germany.

EDUCATION

2001–2007	Max-Planck-Gymnasium Delmenhorst, Germany.
2007–2010	Bachelor of Science in Mathematics with minor in economics TU München, Munich, Germany. *Thesis title:* Density Factorizations Using Graphical Models
Aug. – Dec. 2009	Exchange semester at Hong Kong University of Science and Technology Hong Kong, China.
2010 - 2011	Exchange year at Ecole Centrale Paris Châtenay-Malabry, France.
2010 – 2012	Master of Science in Mathematical Finance and Actuarial Science TU München, Munich, Germany. *Thesis title:* Default Risks in Random Networks *Advisor:* Prof. Dr. Nina Gantert
Apr. 2013 – Apr. 2017	PhD candidate at TU Delft Network Architectures and Services Group Delft, The Netherlands. *Thesis title:* The Relation between Structure and Function in Brain Networks *Promotors:* Prof. dr. Piet Van Mieghem, TU Delft and Prof. dr. Cornelis Jan Stam, VU University Medical Center Amsterdam

SCHOLARSHIPS

2007 - 2012	Scholarship of the Konrad-Adenauer-Foundation

LIST OF PUBLICATIONS

10. **J. Meier**, H. Wang and P. Van Mieghem, *Generalized α-Tree Sampling Method Shows Link Importance Beyond Betweenness, in preparation.**

9. M. Märtens, **J. Meier**, A. Hillebrand, P. Tewarie and P. Van Mieghem, *Brain Network Clustering with Information Flow Motifs*, *Journal of Applied Network Science* (SpringerOpen), invited article, *submitted.**

8. **J. Meier**, X. Zhou, A. Hillebrand, P. Tewarie, C.J. Stam and P. Van Mieghem, *The Epidemic Spreading Model and the Direction of Information Flow in Brain Networks*, *NeuroImage*, **152**, pp. 639-646 (2017).*

7. **J. Meier**, M. Märtens, A. Hillebrand, P. Tewarie and P. Van Mieghem, *Motif-Based Analysis of Effective Connectivity in Brain Networks*, in *Fifth International Workshop on Complex Networks and their Applications* (Springer), November 30 - December 2, Milan, Italy, pp. 685 - 696 (2016).*

6. P. Tewarie, A. Hillebrand, B.W. van Dijk, C.J. Stam, G.C. O'Neill, P. Van Mieghem, **J. Meier**, M.W. Woolrich, P.G. Morris and M.J. Brookes, *Integrating cross-frequency and within band functional networks in resting-state MEG: a multi-layer network approach*, *NeuroImage*, **142**, pp. 324–336 (2016).

5. P. Tewarie, M.G. Bright, A. Hillebrand, S.E. Robson, L.E. Gascoyne, P.G. Morris, **J. Meier**, P. Van Mieghem and M.J. Brookes, *Predicting haemodynamic networks using electrophysiology: the role of non-linear and cross-frequency interactions*, *NeuroImage*, **130**, pp. 273-292 (2016).

4. **J. Meier**, P. Tewarie, A. Hillebrand, L. Douw, B.W. van Dijk, S.M. Stufflebeam and P. Van Mieghem, *A mapping between structural and functional brain networks*, *Brain Connectivity*, **6**(4), pp. 298-311 (2016).*

3. C.J. Stam, W.C.W. van Straaten, E. Van Dellen, P. Tewarie, G. Gong, A. Hillebrand, **J. Meier**, and P. Van Mieghem, *The relation between structural and functional connectivity patterns in complex brain networks*, *International Journal of Psychophysiology*, **103**(5), pp. 149–160. (2016).

2. **J. Meier**, P. Tewarie and P. Van Mieghem, *The Union of Shortest Path Trees of Functional Brain Networks*, *Brain Connectivity*, **5**(9), pp. 575-581 (2015).*

1. M. Yu, A. Hillebrand, P. Tewarie, **J. Meier**, B.W. van Dijk, P. Van Mieghem and C.J. Stam, *Hierarchical clustering in minimum spanning trees*, *Chaos: An Interdisciplinary Journal of Nonlinear Science*, **25**(2), 023107 (2015).

* part of this dissertation

ISBN 9789402806380